St3TART-FO — FRM for Sentinel-3 Land Altimetry

St3TART-FOLLOW-ON: FIDUCIAL REFERENCE MEASUREMENTS (FRM) - S3 LAND ALTIMETRY

Sea Ice FRM protocols and procedures (TD-08_2), v1.0

For the attention of: Mrs. Filomena CATAPANO - ESA

Mr. Pierre FÉMÉNIAS - ESA

	Function	Name	Signature	Date
Prepared by	St3TART-FO Project Team	Claire MILLER	*signature*	26/11/24
Approved by	Project manager (NOVELTIS)	Claire MILLER	*signature*	26/11/24
Authorized by	Deputy CEO (NOVELTIS)	Mahmoud EL HAJJ		26/11/24
Accepted by	ESA Technical Officer	Filomena CATAPANO		

NOVELTIS

153 rue du Lac – 31670 Labège – France
Ph: +33 (0)562 88 11 11 – Fax: +33 (0)562 88 11 12 – E-mail : noveltis@noveltis.fr

afaq ISO 9001 Qualité AFNOR CERTIFICATION

Distribution list

INTERNAL	EXTERNAL	
Name	**Name**	**Company / Organisation**
NOVELTIS Documentation Mr. Richard BRU Mr. Mahmoud EL HAJJ St3TART-FO Project team	Ms Filomena CATAPANO Mr. Pierre FÉMÉNIAS	ESA ESA

Document status

St3TART-FOLLOW-ON: FIDUCIAL REFERENCE MEASUREMENTS (FRM) - S3 LAND ALTIMETRY Sea Ice FRM protocols and procedures (TD-08_2), v1.0			
Issue	**Revision**	**Date**	**Reason for the revision**
1	0	26/11/2024	Initial version

Modification status				
Issue	Rev	Status *	Modified pages	Reason for the modification

*		I = Inserted		D = Deleted		M = Modified*

Acronyms

AEM	Airborne ElectroMagnetic
ALS	Airborne Laser Scanner
AO	Announcement of Opportunity
API	Application Programming Interface
AWI	Alfred Wegener Institute
AWS	Automatic Weather Stations
Cal/Val	Calibration/Validation
CCI	Climate Change Initiative
CCR	Contract Close-out Review
CLS	Collecte Localisation Satellites
CIMR	Copernicus Imaging Microwave Radiometer
CO	Contract Officer
CRISTAL	Copernicus polaR Ice and Snow Topography ALtimeter
CS-2	CryoSat-2 mission
CSV	Comma-Separated Values
DOI	Digital Object Identifier
DSM	Digital Surface Models
DTU	Denmark's Technical University
EASE	Equal Area Scalable Earth
EEA	European Environmental Agency
eLTER	European Long-Term Ecosystem Research
EO	Earth Observation
ESA	European Space Agency
EUMETSAT	European Organization for the Exploitation of Meteorological Satellites
FAQ	Frequently Asked Questions

FF	Fully Focused
FFP	Firm Fixed Price
FO	Follow On
FR	Final Review
FRM	Fiducial Reference Measurement
FRM-CC	FRM Collaborative Campaign
GCOS	Global Climate Observing System
GCP	Ground Control Point
GeoJSON	Geographic JavaScript Object Notation
GIS	Geographic Information System
GNSS	Global Navigation Satellite Systems
GPS	Global Positioning System
GRDC	Global Runoff Data Center
IMBIE	Ice sheet Mass Balance Intercomparison Exercise
IPS	Ice Profiling Sonar
ITT	Invitation To Tender
KO	Kick Off
LEGOS	Laboratoire d'Etudes en Géophysique et Océanographie Spatiales (literally : Laboratory of Space Geophysical and Oceanographic Studies)
LiDAR	Light Detection And Ranging
LOCEAN	Laboratoire d'Océanographie et du Climat: Expérimentations et Approches Numériques (literally : Laboratory of Oceanography and Climate: Experimentations and Numerical Approaches)
MoM	Minutes of Meeting
MPC	Mission Performance Cluster
NetCDF	Network Common Data Form
NORCE	Norwegian Research Center
NSIDC	National Snow and Ice Data Center
NPI	Norwegian Polar Institute

OLCI	Ocean and Land Colour Instrument
ORR	Operation Readiness Review
OZCAR	Observatoires de la Zone Critique, Applications et Recherches (literally: Critical Zone Observatories, Applications and Research)
PM	Progress Meeting
POCA	Point of Closest Approach
PPP	Precise Point Positioning
PR	Progress Review
PVR	Product Validation Report
QA4EO	Quality Assurance framework for Earth Observation
QGIS	Quantum Geographic Information System
QWG	Quality Working Group
RB	Requirements Baseline
REMA	Reference Elevation Model of Antarctica
S3	Sentinel-3
S3VT	Sentinel-3 Validation Team
SAR	Synthetic Aperture Radar
SBLA	Single Point Laser Altimeter
ScalSIT	Super Cal/Val Site Identifier Tool
SfM	Structure-from-Motion
SI	Système International d'unités (literally: International System of Units)
SIMS	Sea Ice Measurement System
SIN'XS	Sea Ice thickness product intercomparison exercise
SLSTR	Sea and Land Surface Temperature Radiometer
SMB	Surface Mass Balance
SNO-GLACIOCLIM	Service National d'Observation GLACIOlogique et CLIMatologique des régions de montagne (literally: National Glaciological and Climatological Observation Service for Mountain Regions)
SoW	Statement of Work

SPR	Set-up Phase Review
SWOT	Surface Water and Ocean Topography
St3TART	Sentinel-3 Topography mission Assessment through Reference Techniques (contract between 2021 and 2023)
St3TART-FO	St3TART Follow-On
STM	Surface Topography Mission
TBD	To Be Defined
TDP	Thematic Data Products
TO	Technical Officer
UAV	Unmanned Aerial Vehicles
UN	UNfocused
WP	Work Package

References

N°	Reference	Title
[RD1]	ESA-EOPG-EOPGMQ-SOW-80, Issue 1 Rev. 0 – 24/11/2023	Statement of Work - H2.2/2023/001 - FIDUCIAL REFERENCE MEASUREMENTS (FRM) - S3 LAND ALTIMETRY ST3TART (FOLLOW-ON)
[RD2]	NOV-FE-1464-PR-004	Detailed Proposal
[RD3]	ESA Contract No. 4000144565/24/I-KE	ESA Contract – H2.2/2023/001 - FIDUCIAL REFERENCE MEASUREMENTS (FRM) - S3 LAND ALTIMETRY ST3TART (FOLLOW-ON)
[RD4]	Ader M. and Axelsson, D. (2017). Drones in Arctic Environments, Master of Science Thesis, KTH Industrial Engineering and Management, Stockholm, Sweden.	
[RD5]	Akitaya, E., "Studies of depth hoar," Contrib. Inst. Low Temp. Sci., vol. 26A, pp. 1–67, 1974. URI: http://hdl.handle.net/2115/20238	
[RD6]	Alexandrov, V., Sandven, S., Wahlin, J., and Johannessen, O. M. (2010): The relation between sea ice thickness and freeboard in the Arctic, The Cryosphere, 4, 373–380, https://doi.org/10.5194/tc-4-373-2010.	
[RD7]	AMAP, 2015. Arctic Science RPAS Operator's Handbook. By: R. Storvold, C. Sweatte, P. Ruel, M. Wuennenberg, K. Tarr, M. Raustein, T. Hillesøy, T. Lundgren, M. Sumich. Arctic Monitoring and Assessment Programme, Oslo. 25 pp. ISBN: 978-82-7971-090-5	
[RD8]	AMAP, 2012. Enabling Science use of Unmanned Aircraft Systems for Arctic Environmental Monitoring. By: W. Crowe, K.D. Davis, A. la Cour-Harbo, T. Vihma, S. Lesenkov, R. Eppi, E.C. Weatherhead, P.Liu, M. Raustein, M. Abrahamsson, K-S.Johansen, D. Marshall, R. Storvold, B. Mulac. AMAP Technical Report No. 6 (2012). Arctic Monitoring and Assessment Programme (AMAP), Oslo. 30 pp. ISBN: 978-82-7971-076-9	
[RD9]	Armitage, T. W. K., & Ridout, A. L. (2015). Arctic sea ice freeboard from AltiKa and comparison with CryoSat-2 and Operation IceBridge. Geophysical Research Letters, 42(16), 6724–6731. https://doi.org/10.1002/2015GL064823	
[RD10]	Arndt, S., Haas, C., Meyer, H., Peeken, I., and Krumpen, T. (2021): Recent observations of superimposed ice and snow ice on sea ice in the northwestern Weddell Sea, The Cryosphere, 15, 4165–4178, https://doi.org/10.5194/tc-15-4165-2021.	
[RD11]	Ayhan, S., et al. (2016), Millimeter-wave radar sensor for snow height measurements, IEEE Trans. on Geoscience and Remote Sensing, PP, issue 99, pp: 1-8, (99), 1–8, doi:10.1109/TGRS.2016.2616441.	
[RD12]	Beaven, S. G., G. L. Lockhart, S. P. Gogineni, A. R. Hossetnmostafa, K. Jezek, A. J. Gow, D. K. Perovich, A. K. Fung, and S. Tjuatja (1995), Laboratory measurements of radar backscatter from bare and snow-covered saline ice sheets, Int. J. Remote Sens., 16(5), 851– 876. https://doi.org/10.1080/01431169508954448	
[RD13]	Beckers, J. F., A. H.H. Renner, G. Spreen, S. Gerland and C. Haas, (2015). Sea-ice surface roughness estimates from airborne laser scanner and laser altimeter observations in Fram Strait and north of Svalbard, Annals of Glaciology, 56 (69), pp 235-244, doi:10.3189/2015AoG69A717	

[RD14]	BIPM. International Vocabulary of Metrology-Basic and General Concepts and Associated Terms (VIM), 3rd ed.; JCGM/WG 2 Doc. N313; Bureau Int. des Poids et Measures: Sevres, France, 2012.
[RD15]	Blair, J. B., Rabine, D. L., & Hofton, M. A. (1999). The Laser Vegetation Imaging Sensor: A medium-altitude, digitization-only, airborne laser altimeter for mapping vegetation and topography. ISPRS Journal of Photogrammetry and Remote Sensing, 54, 115–122. https://doi.org/10.1016/S0924-2716(99)00002-7
[RD16]	Brunt, K. M., Neumann, T. A., & Smith, B. E. (2019). Assessment of ICESat-2 ice sheet surface heights, based on comparisons over the interior of the Antarctic ice sheet. Geophysical Research Letters, 46(22), 13072–13078. https://doi.org/10.1029/2019GL084886
[RD17]	Brunt, K. M., Hawley, R. L., Lutz, E. R., Studinger, M., Sonntag, J. G., Hofton, M. A., et al. (2017). Assessment of NASA airborne laser altimetry data using ground-based GPS data near Summit Station, Greenland. The Cryosphere, 11(2), 681–692. https://doi.org/10.5194/tc-11-681-2017
[RD18]	Connor, L. N., Farrell, S. L., McAdoo, D. C., Krabill, W. B., & Manizade, S. (2013). Validating ICESat over thick sea ice in the northern Canada Basin. IEEE Transactions on Geoscience and Remote Sensing, 51(4), 2188–2200. https://doi.org/10.1109/TGRS.2012.2211603
[RD19]	Doble, M. J., H. Skourup, P. Wadhams, and C. A. Geiger (2011), The relation between Arctic sea ice surface elevation and draft: A case study using coincident AUV sonar and airborne scanning laser, J. Geophys. Res., 116, C00E03, doi:10.1029/2011JC007076
[RD20]	Donlon, C.J.; Minnett, P.J.; Wimmer,W. Chapter 5.2-Strategies for the Laboratory and Field Deployment of Ship-Borne Fiducial Reference Thermal Infrared Radiometers in Support of Satellite-Derived Sea Surface Temperature Climate Data Records. In Experimental Methods in Sciences; Elsevier: Waltham, MA, USA, 2015; Volume 47, pp. 557–603, ISBN 9780124170117
[RD21]	Farrell, S. L., Duncan, K., Buckley,E. M., Richter-Menge, J., & Li, R.(2020). Mapping sea ice surface topography in high fidelity with ICESat-2. Geophysical Research Letters,47, e2020GL090708. https://doi.org/10.1029/2020GL090708
[RD22]	Farrell, S. L., Brunt, K. M., Ruth, J. M., Kuhn, J. M., Connor, L. N., & Walsh, K. M. (2015). Sea-ice freeboard retrieval using digital photon- counting laser altimetry. Annals of Glaciology, 56(69), 167–174. https://doi.org/10.3189/2015AoG69A686
[RD23]	Farrell, S. L., Kurtz, N., Connor, L. N., Elder, B. C., Leuschen, C., Markus, T., et al. (2012). A first assessment of IceBridge snow and ice thickness data over Arctic sea ice. IEEE Transactions on Geoscience and Remote Sensing, 50(6), 2098–2111. https://doi.org/10.1109/TGRS.2011.2170843
[RD24]	Farrell, S. L., Markus, T., Kwok, R., & Connor, L. (2011). Laser altimetry sampling strategies over sea ice. Annals of Glaciology, 52(57), 69–76. https://doi.org/10.3189/172756411795931660
[RD25]	Forsström, S., Gerland, S., & Pedersen, C. A. (2011). Thickness and density of snow-covered sea ice and hydrostatic equilibrium assumption from in situ measurements in Fram Strait, the Barents Sea and the Svalbard coast. Annals of Glaciology, 52(57), 261–269. https://doi.org/10.3189/172756411795931598
[RD26]	Gaffey, C., & Bhardwaj, A. (2020). Applications of Unmanned Aerial Vehicles in Cryosphere: Latest Advances and Prospects. Remote. Sens., 12, 948. doi: 10.3390/rs12060948
[RD27]	Garnier, F., Fleury, S., Garric, G., Bouffard, J., Tsamados, M., Laforge, A., Bocquet, M., Fredensborg Hansen, R. M., and Remy, F. (2021): Advances in altimetric snow depth estimates using bi-frequency

	SARAL and CryoSat-2 Ka–Ku measurements, The Cryosphere, 15, 5483–5512, https://doi.org/10.5194/tc-15-5483-2021.
[RD28]	Gao, H.; Yang, D.; Zhang, B.; Wang, Q.; Wang, F. Remote Sensing of Sea Ice Thickness with GNSS Reflected Signal. J. Electron. Inf. Technol. 2017, 39, 1096–1100. doi: 10.11999/JEIT160765
[RD29]	Guerreiro, K., Fleury, S., Zakharova, E., Rémy, F., Kouraev, A., 2016. Potential for estimation of snow depth on Arctic sea ice from CryoSat-2 and SARAL/AltiKa missions. Remote Sensing of Environment 186, 339–349. https://doi.org/10.1016/j.rse.2016.07.013
[RD30]	Haas, C., & Jochmann, P. (2003). Continuous EM and ULS thickness profiling in support of ice force measurements. In S Loeset, B Bonnemaire, & M Bjerkas (Eds.), Proceedings of the 17th International Conference on Port and Ocean Engineering under Arctic Conditions, POAC ´03, Trondheim, Norway, (Vol. 2, pp. 849– 856). Trondheim, Norway: Department of Civil and Transport Engineering, Norwegian University of Science and Technology NTNU.
[RD31]	Haas, C., Gerland, S., Eicken, H., Miller, H., 1997. Comparison of sea-ice thickness measurements under summer and winter conditions in the Arctic using a small electromagnetic induction device. Geophysics 62, 749–757. https://doi.org/10.1190/1.1444184
[RD32]	Haas, C., Hendricks, S.,Doble, M., 2006. Comparison of the sea ice thickness distribution in the Lincoln Sea and adjacent Arctic Ocean in 2004 and 2005. Annals of Glaciology, 44, 247–252. https://doi.org/10.3189/172756406781811781
[RD33]	Haas, C., Lobach, J., Hendricks, S., Rabenstein, L., Pfaffling, A., 2009. Helicopter-borne measurements of sea ice thickness, using a small and lightweight, digital EM system. Journal of Applied Geophysics, Volume 67, Issue 3, 234-241, doi: 10.1016/j.jappgeo.2008.05.005.
[RD34]	Haas, C., Hendricks, S., Ricker, R., King, J., Beckers, J., Skourup, H., et al. (2016). CryoVal-SI: CryoSat Sea Ice Product Validation using CryoVex and IceBridge campaign data (Tech. Note 3 v 1.1: Assessment of different sources of uncertainty). Norway: Norwegian Polar Institute.
[RD35]	Haas, C., Beckers, J., King, J., Silis, A., Stroeve, J., Wilkinson, J., Notenboom, B., Schweiger, A., & Hendricks, S. (2017). Ice and snow thickness variability and change in the high Arctic Ocean observed by in situ measurements. Geophysical Research Letters, 44, 10,462– 10,469. https://doi.org/10.1002/2017GL075434
[RD36]	Hallikainen, M. T., F. T. Ulaby, and M. Abdelrazik, "Dielectric properties of snow in the 3 to 37 GHz range," IEEE Trans. Antennas Propag., vol. AP-34, no. 11, pp. 1329–1340, Nov. 1986. doi:10.1109/TAP.1986.1143757
[RD37]	Harpold, R., Yungel, J., Linkswiler, M., & Studinger, M. (2016). Intra-scan intersection method for the determination of pointing biases of an airborne altimeter. International Journal of Remote Sensing, 37(3), 648–668. https://doi.org/10.1080/01431161.2015.1137989
[RD38]	Helm, V. , Hendricks, S. , Göbell, S. , Rack, W. , Haas, C. , Nixdorf, U. and Boebel, T.: CryoVEx 2004 and 2005 (BoB) data acquisition and final report , Alfred Wegener Institute, Bremerhaven, Germany, ESA contract C18677/04/NL/GS, 2006
[RD39]	Holt, B., Johnson, M. P., Perkovic-Martin, D., & Panzer, B. (2015). Snow depth on Arctic sea ice derived from radar: In situ comparisons and time series analysis. Journal of Geophysical Research: Oceans, 120(6), 4260–4287. https://doi.org/10.1002/2015JC010815

[RD40]	Huntington H.P., Gearheard S., Holm L.K. (2010) The Power of Multiple Perspectives: Behind the Scenes of the Siku–Inuit–Hila Project. In: Krupnik I., Aporta C., Gearheard S., Laidler G., Kielsen Holm L. (eds) SIKU: Knowing Our Ice. Springer, Dordrecht. https://doi.org/10.1007/978-90-481-8587-0_11
[RD41]	Hutchings, J., Delamere, J., and Heil, P.; The Ice Watch Manual (2020). University of Alaska Fairbanks. Technical Note.
[RD42]	Hvidegaard, S. M., & Forsberg, R. (2002). Sea-ice thickness from airborne laser altimetry over the Arctic Ocean north of Greenland. Geophysical Research Letters, 29(20), 1952. https://doi.org/10.1029/2001GL014474
[RD43]	IASC (International Arctic Science Committee), 2016: Multidisciplinary drifting Observatory for the Study of Arctic Climate (MOSAIC) - Science Plan. September 2016.
[RD44]	IASC (International Arctic Science Committee), 2018: Multidisciplinary drifting Observatory for the Study of Arctic Climate (MOSAIC) - Implementation plan. September 2018.
[RD45]	Jackson, Keith, Jeremy Wilkinson, Ted Maksym, David Meldrum, Justin Beckers, Christian Haas, and David Mackenzie. " A Novel and Low-Cost Sea Ice Mass Balance Buoy", Journal of Atmospheric and Oceanic Technology 30, 11 (2013): 2676-2688, accessed Oct 7, 2021, https://doi.org/10.1175/JTECH-D-13-00058.1
[RD46]	Jutila, A. and Hendricks, S. and Ricker, R. and von Albedyll, L. and Krumpen, T. and Haas, C. (2022), Retrieval and parameterisation of sea-ice bulk density from airborne multi-sensor measurements, The Cryosphere, 16 (1), pages 259-275, https://tc.copernicus.org/articles/16/259/2022/, doi:10.5194/tc-16-259-2022.
[RD47]	Kern, S., Khvorostovsky, K., Skourup, H., Rinne, E., Parsakhoo, Z. S., Djepa, V., Wadhams, P., and Sandven, S. (2015): The impact of snow depth, snow density and ice density on sea ice thickness retrieval from satellite radar altimetry: results from the ESA-CCI Sea Ice ECV Project Round Robin Exercise, The Cryosphere, 9, 37–52, https://doi.org/10.5194/tc-9-37-2015.
[RD48]	King, J. and Howell, S. and Brady, M. and Toose, P. and Derksen, C. and Haas, C. and Beckers, J. (2020), Local-scale variability of snow density on Arctic sea ice, The Cryosphere, 14 (12), pp 4323-4339, https://tc.copernicus.org/articles/14/4323/2020/, doi: 10.5194/tc-14-4323-2020
[RD49]	Koenig, L. S., Ivanoff, A., Alexander, P. M., MacGregor, J. A., Fettweis, X., Panzer, B., et al. (2016). Annual Greenland accumulation rates (2009–2012) from airborne snow radar. The Cryosphere, 10, 1739–1752. https://doi.org/10.5194/tc-10-1739-2016
[RD50]	Krabill, W. B., Abdalati, W., Frederick, E. B., Manizade, S. S., Martin, C. F., Sonntag, J. G., et al. (2002). Aircraft laser altimetry measurement of elevation changes of the Greenland Ice Sheet: Technique and accuracy assessment. Journal of Geodynamics, 34(3–4), 357–376. https://doi.org/10.1016/S0264-3707(02)00040-6
[RD51]	Krabill, W. B., Thomas, R. H., Martin, C. F., Swift, R. N., & Frederick, E. B. (1995). Accuracy of airborne laser altimetry over the Greenland ice sheet. International Journal of Remote Sensing, 16(7), 1211–1222. https://doi.org/10.1080/01431169508954472
[RD52]	Kramar, V. (2019). UAS (drone) Arctic Challenges-Next Steps.Proceedings of the 25th Conference of Fruct Association. ISSN 2305-7254

[RD53]	Kurtz, N., Studinger, M., Harbeck, J. P., Onana, V. D., & Yi, D. (2015). IceBridge L4 sea ice freeboard, snow depth, and thickness, version 1. Boulder, CO: NASA National Snow and Ice Data Center Distributed. Active Archive Center. https://doi.org/10.5067/G519SHCKWQV6
[RD54]	Kurtz, N. T., Galin, N., & Studinger, M. (2014). An improved CryoSat-2 sea ice freeboard retrieval algorithm through the use of waveform fitting. The Cryosphere, 8, 1217–1237. https://doi.org/10.5194/tc-8-1217-2014
[RD55]	Kurtz, N. T., Farrell, S. L., Studinger, M., Galin, N., Harbeck, J. P., Lindsay, R., et al. (2013). Sea ice thickness, freeboard, and snow depth products from Operation IceBridge airborne data. The Cryosphere, 7, 1035–1056. https://doi.org/10.5194/tc-7-1035-2013
[RD56]	Kurtz, N. T., and Farrell, S. L. (2011), Large-scale surveys of snow depth on Arctic sea ice from Operation IceBridge, Geophys. Res. Lett., 38, L20505, doi:10.1029/2011GL049216.
[RD57]	Kurtz, N. T., Markus, T., Cavalieri, D. J., Sparling, L. C., Krabill, W. B., Gasiewski, A. J., & Sonntag, J. G. (2009). Estimation of sea ice thickness distributions through the combination of snow depth and satellite laser altimetry data. Journal of Geophysical Research, 114, C10007. https://doi.org/10.1029/2009JC005292
[RD58]	Kwok, R., Kacimi, S., Webster, M. A., Kurtz, N. T., & Petty, A. A. (2020). Arctic snow depth and sea ice thickness from ICESat-2 and CryoSat-2 freeboards: A first examination. Journal of Geophysical Research: Oceans, 125, e2019JC016008. https://doi.org/ 10.1029/2019JC016008
[RD59]	Kwok, R., Kacimi, S., Markus, T., Kurtz, N. T., Studinger, M., Sonntag, J. G., et al. (2019). ICESat-2 surface height and sea ice freeboard assessed with ATM Lidar acquisitions from Operation IceBridge. Geophysical Research Letters, 46, 11228–11236. https://doi.org/10.1029/2019GL084976
[RD60]	Kwok, R., Kurtz, N. T., Brucker, L., Ivanoff, A., Newman, T., Farrell, S. L., et al. (2017). Intercomparison of snow depth retrievals over Arctic sea ice from radar data acquired by Operation IceBridge. The Cryosphere, 11(6), 2571–2593. https://doi.org/10.5194/tc-11-2571-2017
[RD61]	Kwok, R., & Maksym, T. (2014). Snow depth of the Weddell and Bellingshausen sea ice covers from IceBridge surveys in 2010 and 2011: An examination. Journal of Geophysical Research: Oceans, 119(7), 4141–4167. https://doi.org/10.1002/2014JC009943
[RD62]	Kwok, R., Cunningham, G. F., Manizade, S. S., & Krabill, W. B. (2012). Arctic sea ice freeboard from IceBridge acquisitions in 2009: Estimates and comparisons with ICESat. Journal of Geophysical Research, 117(C2). https://doi.org/10.1029/2011JC007654
[RD63]	Kwok, R., Cunningham, G. F., Wensnahan, M., Rigor, I., Zwally, H. J., & Yi, D. (2009). Thinning and volume loss of the Arctic Ocean sea ice cover: 2003–2008. Journal of Geophysical Research, 114, C07005. https://doi.org/10.1029/2009JC005312
[RD64]	Kwok, R., & Cunningham, G. F. (2008). ICESat over Arctic sea ice: Estimation of snow depth and ice thickness. Journal of Geophysical Research, 113, C08010. https://doi.org/10.1029/2008JC004753
[RD65]	Kwok, R., & Haas, C. (2015). Effects of radar side-lobes on snow depth retrievals from Operation IceBridge. Journal of Glaciology, 61(227), 576-584. doi:10.3189/2015JoG14J229
[RD66]	Landy, J. et al 2022. A year-round satellite sea-ice thickness record from CryoSat-2. Nature 2022, 609(7927), 517-522. doi: 10.1038/s41586-022-05058-5

[RD67]	Lalumiere, L., and S. Prinsenberg (2009), Integration of a helicopter-based ground penetrating radar (GPR) with a laser, video and GPS system, paper presented at 19th International Offshore and Polar Engineering Conference, Osaka, Japan. ISBN 978-1-880653-53-1 (Set); ISSN 1098-618
[RD68]	Liao, Z., Bin Cheng, JieChen Zhao, Timo Vihma, Keith Jackson, Qinghua Yang, Yu Yang, Lin Zhang, Zhijun Li, Yubao Qiu & Xiao Cheng (2019) Snow depth and ice thickness derived from SIMBA ice mass balance buoy data using an automated algorithm, International Journal of Digital Earth, 12:8, 962-979, doi: 10.1080/17538947.2018.1545877
[RD69]	Lucieer V, Nau AW, Forrest AL, Hawes I. Fine-Scale Sea Ice Structure Characterized Using Underwater Acoustic Methods. Remote Sensing. 2016; 8(10):821. https://doi.org/10.3390/rs8100821
[RD70]	MacGregor, J. A., Boisvert, L. N., Medley, B., Petty, A. A., Harbeck, J. P., Bell, R. E., et al. (2021). The scientific legacy of NASA's Operation IceBridge. Reviews of Geophysics, 59, e2020RG000712. https://doi.org/10.1029/2020RG000712
[RD71]	Mahoney, A. and Gearheard, S., 2008, Handbook for community-based sea ice monitoring, NSIDC Special Report 14, Boulder, CO, USA: National Snow and Ice Data Center. http://nsidc.org/pubs/special/nsidc_special_report_14.pdf
[RD72]	Martin, C. F., Krabill, W. B., Manizade, S. S., Russell, R. L., Sonntag, J. G., Swift, R. N., & Yungel, J. K. (2012). Airborne topographic mapper calibration procedures and accuracy assessment (NASA Technical Report TM-2012-215891) (pp. 32). NASA Center for AeroSpace Information
[RD73]	Massom, R. A., H. Eicken, C. Haas, M. O. Jeffries, M. R. Drinkwater, M. Sturm, A. P. Worby, X. R. Wu, V. I. Lytle, S. Ushio, K. Morris, P. A. Reid, S. G. Warren, and I. Allison, "Snow on Antarctic Sea ice," Rev. Geophys., vol. 39, no. 3, pp. 413–445, Aug. 2001. https://doi.org/10.1029/2000RG000085
[RD74]	Mertikas, S.; Tripolitsiotis, A.; Donlon, C.; Mavrocordatos, C.; Féménias, P.; Borde, F.; Frantzis, X.; Kokolakis, C.; Guinle, T.; Vergos, G.; Tziavos, I.N.; Cullen, R. The ESA Permanent Facility for Altimetry Calibration: Monitoring Performance of Radar Altimeters for Sentinel-3A, Sentinel-3B and Jason-3 Using Transponder and Sea-Surface Calibrations with FRM Standards. Remote Sens. 2020, 12, 2642. https://doi.org/10.3390/rs12162642
[RD75]	Mertikas, S.P.; Donlon, C.; Vuilleumier, P.; Cullen, R.; Féménias, P.; Tripolitsiotis, A. An Action Plan Towards Fiducial Reference Measurements for Satellite Altimetry. Remote Sens. 2019, 11, 1993. https://doi.org/10.3390/rs11171993
[RD76]	MS-DTU-KAR-03- PFF-032, Coccia et al., KAREN Altimeter - Processing chain and file format, Reference Code: MS-DTU-KAR-03- PFF-032, Issue: 3.2, MetaSensing BV Huygensstraat 44 2201DK Noordwijk, The Netherlands Tel.: +31 71 751 5960 Email: info@metasensing.com, Date: 4th July 2019
[RD77]	Munoz-Martin JF, Perez A, Camps A, Ribó S, Cardellach E, Stroeve J, Nandan V, Itkin P, Tonboe R, Hendricks S, Huntemann M, Spreen G, Pastena M. Snow and Ice Thickness Retrievals Using GNSS-R: Preliminary Results of the MOSAiC Experiment. Remote Sensing. 2020; 12(24):4038. https://doi.org/10.3390/rs12244038
[RD78]	Nandan, V., Geldsetzer, T., Yackel, J.,Mahmud, M., Scharien, R., Howell, S.,...Else, B. (2017). Effect of snow salinity on CryoSat-2 Arctic first-year sea ice freeboard measurements. Geophysical Research Letters, 44, 10,419–10,426. https://doi.org/10.1002/2017GL074506R
[RD79]	Newman, T., Farrell, S. L., Richter-Menge, J., Connor, L. N., Kurtz, N. T., Elder, B. C., & McAdoo, D. (2014). Assessment of radar-derived snow depth over Arctic sea ice. Journal of Geophysical Research: Oceans, 119, 8578–8602. https://doi.org/10.1002/2014JC010284

[RD80]	Passaro, M.et al. 2017 Lead detection using Cryosat-2 delay-doppler processing and Sentinel-1 SAR images. Adv. Space Res. 2017. https://doi.org/10.1016/j.asr.2017.07.011
[RD81]	Paul, S., et al. (2018): Empirical parametrization of Envisat freeboard retrieval of Arctic and Antarctic sea ice based on CryoSat-2: progress in the ESA Climate Change Initiative, The Cryosphere, 12, 2437–2460, https://doi.org/10.5194/tc-12-2437-2018.
[RD82]	Cullen, R.: CryoVEx Airborne Data Products Description, Issue 2.6.1, ESA, Ref. CS-LI-ESA-GS-0371, 2010
[RD82-b]	Cullen, R. et al. (2007): Arctic Experiments Supporting CryoSat-2, IUGG, Perugia, July 9th, 2007
[RD83]	Pfaffhuber, A. A., Lieser, J. L., and Haas, C. (2017), Snow thickness profiling on Antarctic sea ice with GPR—Rapid and accurate measurements with the potential to upscale needles to a haystack, Geophys. Res. Lett., 44, 7836– 7844, doi:10.1002/2017GL074202.
[RD84]	Pfaffling, A., Haas, C., Reid, J.E., 2007. A direct helicopter EM sea ice thickness inversion, assessed with synthetic and field data. Geophysics 72, F127–F137. https://doi.org/10.1190/1.2732551
[RD85]	Pfaffling, A. (2007), Ground penetrating radar snow thickness profiling during WWOS 06—Field data report, Hamburg, Germany, doi:10.13140/RG.2.2.29249.76647.
[RD86]	Poisson, J., et al., 2018. Development of an ENVISAT Altimetry Processor Providing Sea Level Continuity Between Open Ocean and Arctic Leads. IEEE Transactions on Geoscience and Remote Sensing 56, 5299–5319. https://doi.org/10.1109/TGRS.2018.2813061
[RD87]	Polashenski, Chris M., Donald K. Perovich, Jacqueline Richter-Menge and Bruce C. Elder. "Seasonal ice mass-balance buoys: adapting tools to the changing Arctic." Annals of Glaciology 52 (2011): 18 - 26. doi: 10.3189/172756411795931516
[RD88]	Proksch, M., Rutter, N., Fierz, C., and Schneebeli, M. (2016): Intercomparison of snow density measurements: bias, precision, and vertical resolution, The Cryosphere, 10, 371–384, https://doi.org/10.5194/tc-10-371-2016.
[RD89]	Qing Ji, Bingjie Li, Xiaoping Pang, Xi Zhao, Ruibo Lei, Arctic sea ice density observation and its impact on sea ice thickness retrieval from CryoSat–2, Cold Regions Science and Technology, Volume 181, 2021, 103177, ISSN 0165-232X, https://doi.org/10.1016/j.coldregions.2020.103177
[RD90]	Quartly, G.D.; Rinne, E.; Passaro, M.; Andersen, O.B.; Dinardo, S.; Fleury, S.; Guillot, A.; Hendricks, S.; Kurekin, A.A.; Müller, F.L.; Ricker, R.; Skourup, H.; Tsamados, M. Retrieving Sea Level and Freeboard in the Arctic: A Review of Current Radar Altimetry Methodologies and Future Perspectives. Remote Sens. 2019, 11, 881. https://doi.org/10.3390/rs11070881
[RD91]	Richter-Menge, J. A., & Farrell, S. L. (2013). Arctic sea ice conditions in Spring 2009–2013 prior to melt. Geophysical Research Letters, 40(22), 5888–5893. https://doi.org/10.1002/2013GL058011
[RD92]	Richter-Menge, J., Perovich, D., Elder, B., Claffey, K., Rigor, I., & Ortmeyer, M. (2006). Ice mass-balance buoys: A tool for measuring and attributing changes in the thickness of the Arctic sea-ice cover. Annals of Glaciology, 44, 205-210. doi:10.3189/172756406781811727

[RD93]	Ricker, R., Hendricks, S., Helm, V., Skourup, H., and Davidson, M.: Sensitivity of CryoSat-2 Arctic sea-ice freeboard and thickness on radar-waveform interpretation, The Cryosphere, 8, 1607–1622, https://doi.org/10.5194/tc-8-1607-2014
[RD94]	Rodriguez-Morales, F., et al., "An Improved UWB Microwave Radar for Very Long-Range Measurements of Snow Cover," in IEEE Transactions on Instrumentation and Measurement, vol. 69, no. 10, pp. 7761-7772, Oct. 2020, doi: 10.1109/TIM.2020.2982813.
[RD95]	Rodríguez-Morales, F., et al., (2021): "A Compact, Reconfigurable, Multi-UWB Radar for Snow Thickness Evaluation and Altimetry: Development and Field Trials," in IEEE Journal of Selected Topics in Applied Earth Observations and Remote Sensing, vol. 14, pp. 6755-6765, doi: 10.1109/JSTARS.2021.3092313.
[RD96]	Rösel, A., Farrell, S. L., Nandan, V., Richter-Menge, J., Spreen, G., Divine, D. V., et al. (2020). Implications of surface flooding on airborne thickness measurements of snow on sea ice, The Cryosphere. https://doi.org/10.5194/tc-2020-168
[RD97]	Sallila, H., Farrell, S. L., McCurry, J., & Rinne, E. (2019). Assessment of contemporary satellite sea ice thickness products for Arctic sea ice. The Cryosphere, 13(4), 1187–1213. https://doi.org/10.5194/tc-13-1187-2019
[RD98]	Skourup, H., S. B. Simonsen, A. Coccia, and R. Forsberg (2020): ESA CryoVEx/KAREN 2016 fall campaign – First airborne field campaign with combined Ku/Ka-band radars over the EGIG-line with coincident in situ measurements. Technical Report, National Space Institute (DTU Space), Technical University of Denmark, ISBN-978-87-91694-44-8
[RD99]	Skourup, H., A. V. Olesen, L. Sandberg Sørensen, S. Simonsen, S. M. Hvidegaard, N. Hansen, A. F. Olesen, A. Coccia, K. Macedo, V. Helm, R. S. Ladkin, R. Forsberg, A. E. Hogg, I. Otosaka, A. Shepherd, C. Haas, and J. Wilkinson: ESA CryoVEx/KAREN and EU ICE-ARC 2017 - Arctic field campaign with combined airborne Ku/Ka-band radar and laser altimeters, together with extensive in situ measurements over sea- and land ice. Technical Report, National Space Institute (DTU Space), Technical University of Denmark, ISBN-978-87-91694-45-5
[RD100]	Stenseng, L., S. M. Hvidegaard, H. Skourup, R. Forsberg, C. J. Andersen, S. Hanson, R. Cullen, and V. Helm: Airborne Lidar and Radar Measurements in and around Greenland, CryoVEx 2006. Danish National Space Center, Technical Report 9, 2007
[RD101]	Stroeve, J., Nandan, V., Willatt, R., Tonboe, R., Hendricks, S., Ricker, R., Mead, J., Mallett, R., Huntemann, M., Itkin, P., Schneebeli, M., Krampe, D., Spreen, G., Wilkinson, J., Matero, I., Hoppmann, M., and Tsamados, M. (2020): Surface-based Ku- and Ka-band polarimetric radar for sea ice studies, The Cryosphere, 14, 4405–4426, https://doi.org/10.5194/tc-14-4405-2020.
[RD102]	Stroeve, J., Nandan, V., Willatt, R., Dadic, R., Rostosky, P., Gallagher, M., Mallett, R., Barrett, A., Hendricks, S., Tonboe, R., McCrystall, M., Serreze, M., Thielke, L., Spreen, G., Newman, T., Yackel, J., Ricker, R., Tsamados, M., Macfarlane, A., Hannula, H.-R., and Schneebeli, M. (2022): Rain on snow (ROS) understudied in sea ice remote sensing: a multi-sensor analysis of ROS during MOSAiC (Multidisciplinary drifting Observatory for the Study of Arctic Climate), The Cryosphere, 16, 4223–4250, https://doi.org/10.5194/tc-16-4223-2022.
[RD103]	Stroeve, J., Barrett, A., Serreze, M., & Schweiger, A. (2014). Using records from submarine, aircraft and satellites to evaluate climate model simulations of Arctic sea ice thickness. The Cryosphere, 8(5), 1839–1854. https://doi.org/10.5194/tc-8-1839-2014

[RD104]	Sturm, M., & Holmgren, J. (2018). An automatic snow depth probe for field validation campaigns. Water Resources Research, 54, 9695– 9701. https://doi.org/10.1029/2018WR023559
[RD105]	Sturm, M. (2009), Field techniques for snow observations on sea ice, in Field Techniques for Sea Ice Research, edited by H. Eicken et al., pp. 25–49, Alaska University Press, Fairbanks, Alaska. ISBN-10: 1602230595
[RD106]	Thielke, Linda & Huntemann, Marcus & Hendricks, Stefan & Jutila, Arttu & Ricker, Robert & Spreen, Gunnar. (2022). Sea ice surface temperatures from helicopter-borne thermal infrared imaging during the MOSAiC expedition. Scientific Data. 9. 364. doi: 10.1038/s41597-022-01461
[RD107]	Ulaby, F. T., Moore, R. K., and Fung, A. K.: Microwave remote sensing: Active and passive, volume 3 – From Theory to Applications, 1986. ISBN 10: 0890061920 ISBN 13: 9780890061923
[RD108]	Vesterhauge, A. (2021) Drones for the Arctic, Master of Science Thesis, Technical University of Denmark, Lyngby, Denmark.
[RD109]	Vivier, F., J. K. Hutchings, Y. Kawaguchi, T. Kikuchi, J. H. Morison, A. Lourenc¸o, and T. Noguchi (2016), Sea ice melt onset associated with lead opening during the spring/summer transition near the North Pole, J. Geophys. Res. Oceans, 121, doi:10.1002/2015JC011588.
[RD110]	P. Wadhams, B. Krogh, Operational history and development plans for the use of AUVs and UAVs to map sea ice topography, Polar Science, Volume 21, 2019, Pages 195-203, ISSN 1873-9652, https://doi.org/10.1016/j.polar.2019.07.004.
[RD111]	Wagner, D. N., Shupe, M. D., Cox, C., Persson, O. G., Uttal, T., Frey, M. M., Kirchgaessner, A., Schneebeli, M., Jaggi, M., Macfarlane, A. R., Itkin, P., Arndt, S., Hendricks, S., Krampe, D., Nicolaus, M., Ricker, R., Regnery, J., Kolabutin, N., Shimanshuck, E., Oggier, M., Raphael, I., Stroeve, J., and Lehning, M. (2022): Snowfall and snow accumulation during the MOSAiC winter and spring seasons, The Cryosphere, 16, 2373-2402, https://doi.org/10.5194/tc-16-2373-2022.
[RD112]	Wang, X., Guan, F., Liu, J., Xie, H., & Ackley, S. (2016). An improved approach of total freeboard retrieval with IceBridge Airborne topographic mapper (ATM) elevation and digital mapping system (DMS) images. Remote Sensing of Environment, 184, 582–594. https://doi.org/10.1016/j.rse.2016.08.002
[RD113]	Wang, X., Xie, H., Ke, Y., Ackley, S. F., & Liu, L. (2013). A method to automatically determine sea level for referencing snow freeboards and computing sea ice thicknesses from NASA IceBridge airborne LIDAR. Remote Sensing of Environment, 131, 160–172. https://doi.org/10.1016/j.rse.2012.12.022
[RD114]	Warren, S. G., Rigor, I. G., Untersteiner, N., Radionov, V. F., Bryazgin, N. N., Aleksandrov, Y. I., & Colony, R. (1999). Snow depth on Arctic sea ice. Journal of Climate, 12(6), 1814–1829. https://doi.org/10.1175/1520-0442(1999)01210.1175/1520-0442(1999)012
[RD115]	Webster, M. A., Rigor, I. G., Nghiem, S. V., Kurtz, N. T., Farrell, S. L., Perovich, D. K., & Sturm, M. (2014). Interdecadal changes in snow depth on Arctic sea ice. Journal of Geophysical Research: Oceans, 119(8), 5395–5406. https://doi.org/10.1002/2014JC009985
[RD116]	Willatt, R., Stroeve, J., Nandan, V., Tonboe, R., Hendricks, S., Ricker, R., Mead, J., Newman, T., Itkin, P., Liston, G., Mallett, R., Zhou, L., Schneebeli, M., Krampe, D., Tsamados, M., Demir, O., Oggier, M., Buehner Gattis, E., and Wilkinson, J. (2021): KuKa altimeter mode data gathered during MOSAiC: scattering from snow covered sea ice and snow depth determination using dual-frequency and

	polarimetric approaches, EGU General Assembly 2021, online, 19–30 Apr 2021, EGU21-16150, https://doi.org/10.5194/egusphere-egu21-16150.
[RD117]	Willatt, R., Laxon, S., Giles, K., Cullen, R., Haas, C., & Helm, V. (2011). Ku-band radar penetration into snow cover on Arctic sea ice using airborne data. Annals of Glaciology, 52(57), 197-205. doi:10.3189/172756411795931589
[RD118]	Willatt, R., K. Giles, S. Laxon, L. Stone-Drake, and A. Worby (2010), Field Investigations of Ku-Band Radar Penetration Into Snow Cover on Antarctic Sea Ice, IEEE Trans. Geosci. Remote Sens., vol. 48, no. 1, Jan. 2010, pp. 365-372.
[RD119]	Witte, H., and E. Fahrbach. 2005. AWI Moored ULS Data, Greenland Sea and Fram Strait, 1991-2002. Boulder, CO: National Snow and Ice Data Center/World Data Center for Glaciology. Digital media.
[RD120]	Worby, A. P., Geiger, C. A., Paget, M. J., Van Woert, M. L., Ackley, S. F., and DeLiberty, T. L. (2008), Thickness distribution of Antarctic sea ice, J. Geophys. Res., 113, C05S92, doi:10.1029/2007JC004254.
[RD121]	Worby, A. P., and I. Allison (1999), A technique for making ship-based observations of Antarctic sea ice thickness and characteristics: Part I. Observational technique and results, Res. Rep. 14, pp. 1–23, Antarct. Coop. Res. Cent., Univ. of Tasmania, Hobart, Tasmania, Australia. ISBN: 1875796096
[RD122]	Yan, Q. and W. Huang, "Sea Ice Thickness Measurement Using Spaceborne GNSS-R: First Results With TechDemoSat-1 Data," in IEEE Journal of Selected Topics in Applied Earth Observations and Remote Sensing, vol. 13, pp. 577-587, 2020, doi: 10.1109/JSTARS.2020.2966880.
[RD123]	Yan, Q., & Huang, W. (2019). Sea Ice Remote Sensing Using GNSS-R: A Review. Remote. Sens., 11, 2565. doi:10.3390/rs11212565
[RD124]	Yi, D., Harbeck, J. P., Manizade, S. S., Kurtz, N. T., Studinger, M., & Hofton, M. (2014). Arctic sea ice freeboard retrieval with waveform characteristics for NASA's Airborne Topographic Mapper (ATM) and Land, Vegetation, and Ice Sensor (LVIS). IEEE Transactions on Geoscience and Remote Sensing, 53(3), 1403–1410. https://doi.org/10.1109/TGRS.2014.2339737
[RD125]	Zhou, L., Stroeve, J., Xu, S., Petty, A., Tilling, R., Winstrup, M., Rostosky, P., Lawrence, I. R., Liston, G. E., Ridout, A., Tsamados, M., and Nandan, V. (2021): Inter-comparison of snow depth over Arctic sea ice from reanalysis reconstructions and satellite retrieval, The Cryosphere, 15, 345–367, https://doi.org/10.5194/tc-15-345-2021.
[RD126]	Zhongxiang, T., Cheng Bin, Zhao Jiechen, Vihma Timo, Zhang Wenliang, Li Zhijun, Zhang Zhanhai (2017) Observed and modelled snow and ice thickness in the Arctic Ocean with CHINARE buoy data. Acta Oceanologica Sinica, 36(8): 66–75, doi: 10.1007/s13131-017-1020-4
[RD127]	http://imb-crrel-dartmouth.org/imb/, last access: 2021/10/07
[RD128]	http://www.spatialtech.com.tw/document/ces/dm/zeno-dm.pdf, last access: 2021/09/11
[RD129]	http://www.snowhydro.com/products/column2.html, last access: 2021/10/11
[RD130]	http://geonics.com/html/em31-mk2.html , last access: 2021/10/11
[RD131]	https://www.awi.de/en/science/climate-sciences/sea-ice-physics/projects/ice-bird.html, last access: 2021/10/12
[RD132]	https://mosaic-expedition.org/, last access: 2021/10/18

[RD133]	IASC, 2016; https://mosaic-expedition.org/expedition/, last access: 2021/10/18
[RD134]	https://nsidc.org/data/NSIDC-0698/versions/1, last access: 2021/09/28
[RD135]	https://www.frm4alt.eu/, last access: 2021/09/28
[RD136]	https://www.serac-crete.eu/, last access: 2021/09/28
[RD137]	https://www.serac-crete.eu/cal-val-techniques.html, last access: 2021/09/28
[RD138]	https://www.serac-crete.eu/cal-val-techniques/sea-surface/10-cal-val-techniques/12-transponder.html, last access: 2021/09/2028
[RD139]	https://www.serac-crete.eu/cal-val-techniques/sea-surface.html, last access: 2021/09/28
[RD140]	https://www.serac-crete.eu/cal-val-techniques/multi-mission-cross-over.html, last access: 2021/09/28
[RD141]	https://www2.whoi.edu/site/beaufortgyre/methods/instruments/
[RD142]	The GUM. Guide to the Expression of Uncertainty in Measurement. Joint Committee for Guides in Metrology (JCGM)
[RD143]	Qing Ji, Bingjie Li, Xiaoping Pang, Xi Zhao, Ruibo Lei (2021): Arctic sea ice density observation and its impact on sea ice thickness retrieval from CryoSat–2, Cold Regions Science and Technology, Volume 181, 2021, 103177, ISSN 0165-232X, https://doi.org/10.1016/j.coldregions.2020.103177.
[RD144]	GCOS Surface Reference Network (GSRN): Justification, requirements, siting and instrumentation options, February 2019. WORLD METEOROLOGICAL ORGANIZATION, INTERGOVERNMENTAL OCEANOGRAPHIC COMMISSION, UNITED NATIONS, ENVIRONMENT PROGRAMME INTERNATIONAL SCIENCE COUNCIL. GCOS-226
[RD145]	Ricker, R.; Hendricks, S.; Beckers, J.F. The Impact of Geophysical Corrections on Sea-Ice Freeboard Retrieved from Satellite Altimetry. Remote Sens. 2016, 8, 317. https://doi.org/10.3390/rs8040317
[RD146]	D.J. Wingham, C.R. Francis, S. Baker, C. Bouzinac, D. Brockley, R. Cullen, P. de Chateau-Thierry, S.W. Laxon, U. Mallow, C. Mavrocordatos, L. Phalippou, G. Ratier, L. Rey, F. Rostan, P. Viau, D.W. Wallis (2006): CryoSat: A mission to determine the fluctuations in Earth's land and marine ice fields, Advances in Space Research, Volume 37, Issue 4, Pages 841-871, ISSN 0273-1177, https://doi.org/10.1016/j.asr.2005.07.027
[RD147]	Skourup, H., Farrell, S. L., Hendricks, S., Ricker, R., Armitage, T. W. K., Ridout, A., Andersen, O. B., Haas, C., and Baker, S. (2017). An assessment of state-of-the-art mean sea surface and geoid models of the Arctic Ocean: Implications for sea ice freeboard retrieval. Journal of Geophysical Research: Oceans, 122, 8593–8613. https://doi.org/10.1002/2017JC013176
[RD148]	S3MPC-STM_RP_0038, Issue 1.1, – 05/12/2022 Contract: 4000136824/21/I-BG - *Sentinel-3 SRAL/MWR Land User Handbook*

[RD149]	Olsen, I. B. L., Skourup, H., Sallila, H., Hendricks, S., Hansen, R. M. F., Kern, S., Paul, S., Bocquet, M., Fleury, S., Divine, D., and Rinne, E.: Dual-hemisphere sea ice thickness reference measurements from multiple data sources for evaluation and product inter-comparison of satellite altimetry, Earth Syst. Sci. Data Discuss. [preprint], https://doi.org/10.5194/essd-2024-234, in review, 2024.

Table of contents

1 Introduction

1.1 Purpose and scope

This document is the Sea Ice FRM protocols and procedures, initially developed for the St3TART project (2021 – 2023) and updated in this St3TART-FO project, [RD1].

This deliverable (TD-08_2) presents a review of the state-of-the-art existing in-situ solutions, procedures, methods, fiducial reference measurement (FRM) data and associated uncertainties that have been already used to assess the performance of satellite altimetry over Sea Ice. This is done to ensure that these observations meet the criteria of FRM standards and can be used in an operational way for the validation of the Sentinel-3 Land topography mission.

1.2 Overview of this document

In addition to this Introduction chapter, this "FRM Protocols and Procedures" document includes the following chapters:

▲ Chapter 2: The altimetry measurement for sea ice
  o Altimeter parameters
  o Auxiliary parameters
  o Sources of uncertainty in the satellite altimeter measurement

▲ Chapter 3: Calibration/Validation framework for sea ice
  o The specific challenges of sea ice
  o Calibration and validation as a comparison process
  o Calibration for sea ice

▲ Chapter 4: Requirements for Cal/Val altimetry measurements of sea ice
  o Types of measurements to include in an FRM suite
  o Campaigns vs. semi-permanent observations
  o FRM quality and other observations

▲ Chapter 5: Existing means for Cal/Val activities
  o Literature review of sea ice altimetry validation data from airborne, shipborne, and in situ sensors
  o Other technologies
  o Uncertainty estimates of existing validation data
  o Calibration measurements for the FRM

▲ Chapter 6: Learnings from alternative satellite missions
  o Learnings from other satellite missions' Cal/Val processes
  o Comparison with other satellites
  o Using the same validation data for multiple satellites

▲ Chapter 7: FRM protocols and procedures
  o Calibration site selection
  o Metrological approach to uncertainties
  o A metrological uncertainty analysis for sea ice TDP
  o Implementing metrological uncertainty analysis for sea ice FRMs

1.3 Definition of FRM and a metrological approach

The Quality Assurance framework for Earth Observation (QA4EO), established and endorsed by Committee on Earth Observation Satellites (CEOS), defines the following principle regarding Earth Observation data quality:

> *'It is critical that data and derived products are easily accessible in an open manner and have an associated indicator of quality traceable to reference standards (preferably SI) so users can assess suitability for their applications i.e., 'fitness for purpose'.'*

QA4EO defines high level processes to achieve this, such as well-documented procedures, participation in comparisons and uncertainty assessments that apply to all EO data records. Traceability requires that this quality indicator be based on "a documented and quantifiable assessment of evidence demonstrating the level of traceability to internationally agreed (where possible SI) reference standards." The QA4EO principle stops short of requiring SI-traceability in all circumstances, recognizing that the full rigor of linkage to SI may not be viable for all applications and measurements, however, the accompanying guidelines are based on metrological concepts adapted from guidelines of the international metrology community and a metrological approach is strongly implied.

Metrology, the science of measurement, is the discipline responsible for maintaining the International System of Units (SI) and the associated system of measurement. It is core to the SI that measurements are stable over centuries and that measurement standards are equivalent worldwide. These properties are achieved through the key principles of metrological traceability: uncertainty analysis and comparison. These same principles are important to Earth observation.

The term "fiducial reference measurement" (FRM) is used for non-satellite observations that follow QA4EO guidelines.

> *Fiducial reference measurements (FRMs) are a suite of independent, fully characterized, and traceable sub-orbital measurements that follow the guidelines outlined by the GEO/CEOS Quality Assurance framework for Earth Observation (QA4EO) and have value for space-based observations.*

Thus, FRMs are the quality-assured non-satellite observations that can be used to calibrate and validate satellite-based sensor measurements. As ESA states 'these FRM provide the maximum return on investment for a satellite mission by delivering, to users, the required confidence in data products, in the form of independent validation results and satellite measurement uncertainty estimation, over the entire end-to-end duration of a satellite mission.'

Other satellite observations cannot be considered FRMs under this definition, but satellite-based comparisons are important in the calibration and validation of satellite missions and to ensure the continuity of the time series between the different missions, in particular for the analysis of climatic evolutions and to feed the reanalysis models. These multi-mission comparisons also make it possible to estimate the coherence and stability of space observations despite the change of space support or sensor types. Thus, a satellite-based comparison should also be considered metrologically, following many similar approaches. Similarly, comparisons with model outputs (e.g. reanalyses) are also used in Cal/Val processes, but are not FRMs.

2 Altimetry measurement for sea ice

S3 SRAL measures the sea ice topography using Ku-band and C-band. The C-band is primarily used as observation to support atmospheric corrections and will not be included here. In Ku-band an often-used assumption is that the signal penetrates the snow layer and reflects at the snow/ice surface based on laboratory findings of cold dry fresh snow (Beaven et al., 1995 [RD12]). This assumption provides satisfying estimates of the derived sea ice thickness, when compared to validation data with exceptions where snow conditions are not dry, cold and fresh, i.e., snow depths in the Southern Hemisphere where the snow can exceed 1m and suppress the sea ice freeboard below the water or due to snow metamorphism.

Quartly et al. (2018) [RD90] provide an extensive review of over 25 years of Arctic altimetry, assessing benefits but also current challenges for the accurate estimation of potential climate-related changes. The basic assumption for altimetry, which measures the ice freeboard, is that of a two-layer medium in hydrostatic balance, composed of an ice layer overlain by a snow layer. The accuracy of the ice thickness retrieval depends chiefly on the uncertainty in the snow load, but also in ice density. These parameters are quite poorly known owed to the lack of in-situ observations.

To fully validate the S3 LAND STM L2 sea ice product and determine the related uncertainty budget, the primary geophysical variables to be assessed over sea Ice are:

▲ Sea ice freeboard (FB);
▲ Surface Type Classification Derived from Altimeter (leads, floes);
▲ Auxiliary snow depth product.

These indirectly include:

▲ Sea ice thickness (from FB and snow);
▲ Sea surface anomalies (needed to compute FB);
▲ Sea ice roughness (intermediate useful parameter).

Currently sea ice thickness is not a geophysical parameter available in the S3 products. However, new products for sea ice thickness will in the future be available, hopefully with the same processing between the missions (see CRYOTEMPO (http://cryosat.mssl.ucl.ac.uk/tempo) and FDR4ALT (https://www.fdr4alt.org) thematic products activities). Processors for Sentinel-3 thematic products are currently developed in the framework of the S3 MPC project under CLS lead, for sea ice, land ice and hydrology products. Until recently these processors did not include a dedicated sea ice product, thus processed without zero-padding and Hammer filtering, which are crucial for SAR processing over sea ice covered regions. More recently, these have been implemented in a pilot version of the new thematic processing strategies, but it does not yet include data prior to June 2022. We have requested (as of December 21, 2022) re-processing of dedicated Sentinel-3 orbits under-flown at the St3TART spring campaign using this new baseline, and hope these will be available within the time-frame of this project, and in time for making a comparison to the campaign data. More information about the dedicated orbits can be found in "TD-13-2 FRM Campaign Final Report for Sea Ice".

To prepare for sea ice thickness as a geophysical parameter in the S3 LAND STM L2 product we also need to investigate:
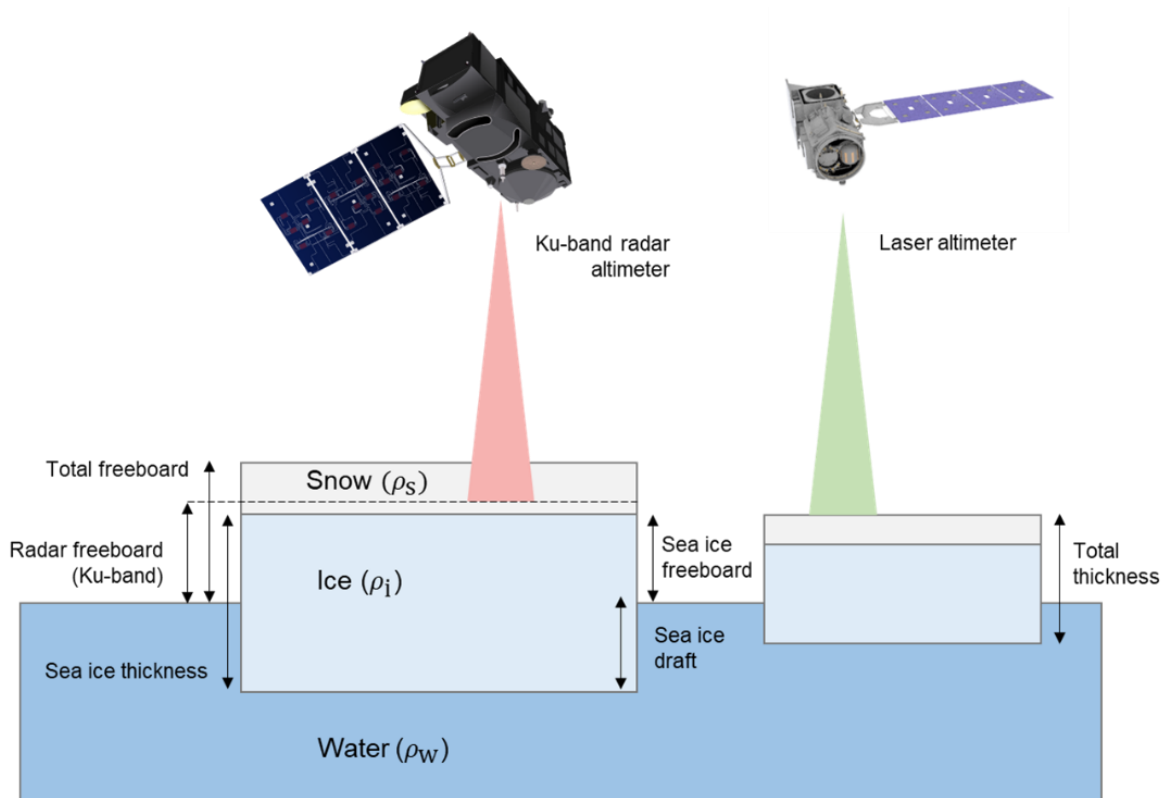
▲ Snow and ice densities.

Figure 2.1: Sea ice variables and parameters of relevance to the altimetry measurements. Adapted from CPOM.

Sea ice thickness is not directly measured. Figure 2.1 shows the relationship between what is measured (the radar freeboard) and other parameters that can be inferred by combining the radar freeboard with additional auxiliary information. The auxiliary information includes the snow depth (traditionally derived from climatologies, although more recently, observations have been used), and the snow, ice and water densities. These are used to derive the sea ice thickness and total ice thickness. All these different parameters are described in section 2.1 below.

In Section 3, we discuss how these quantities can be compared with the FRM observations.

2.1 Altimeter parameters

2.1.1 Radar freeboard

Radar freeboard is defined as the difference between the interpolated Sea Level Anomaly (SLA, which is derived from elevation points originating from leads) and the re-tracked elevation heights of floe observations with respect to the same reference frame as the SLA (a reference Mean Sea Surface such as the DTU18 MSS) obtained from a radar altimeter. The interpolation is performed to determine a sea surface through the ice, interpolating between measurements classified as leads. The SLA, over leads, and ice level anomaly (ILA) over ice, interpolated to a geolocation for the observation are combined to give the radar freeboard.

The physical parameters measured by the radar freeboard depend on the frequency used by the altimeter. Based on laboratory and in-situ tests, the Ka-band waves do not penetrate the snow, or only the very first centimetres, and thus the Ka radar-freeboard correspond to a total freeboard including the ice freeboard and the snow depth [Guerreiro et al. 2016 [RD29]]. On the other hand, the Ku-band can fully penetrate dry, cold, and fresh snow, penetrating down to the snow-ice-interface. Nevertheless, it does not provide the ice freeboard directly and a correction must be applied to take into account the reduction of the speed propagation of the radar wave into the snow.

2.1.2   Sea ice freeboard

While we assume that the radar penetrates to the snow-ice interface (assuming dry snow conditions), one must also consider the slowing of the propagation speed of the radar while it penetrates through the snowpack. If this is not considered, the range from the satellite altimeter to the reflected surface (which is measured by the altimeter) will not be corrected for the snow, and thus, the range will appear longer than it is. When converting from range to elevations, this will decrease the elevation and thus, reduce the freeboard observation (an observation that is equivalent with the radar freeboard, but not to the sea ice freeboard). To compute from Ku radar freeboard (FB_{Ku}) to sea ice freeboard (FB_{ice}), one must add the following correction:

$$FB_{ice} = FB_{Ku} + \delta SD_{Ku},$$

(2.1)

With $\delta SD_{Ku} = (c/c_s - 1)SD$, where SD is the snow depth, c is the speed of light in vacuum and c_s is the speed of light propagation through snow. The speed of light when propagating through snow is related to sea ice through the sea ice density (ρ_s) by the following (Ulaby et al., 1986 [RD107]).

$$c/c_s = (1 + S \cdot \rho_s)^{1.5}; \quad S = 0.00051 \text{ m}^3 \text{ kg}^{-1}$$

(2.2)

Based on the formulas above, it is shown how this correction requires knowledge of the overlying snow depth and the snow density.

2.1.3   Total freeboard (ice + snow)

Total freeboard, or also known as snow freeboard, or laser freeboard, is defined as the difference between the interpolated sea surface height anomaly (derived from elevation points originating from leads) and the re-tracked elevation heights of floe observations obtained from a laser altimeter (both green and near-infra-red lasers). Due to the wavelength of the laser altimeters (nano-meters), no penetration is expected or assumed for laser altimeters, and therefore the total freeboard is expected to be reflected at the snow-air-interface.

$$FB_{total} = FB_{ice} + SD.$$

(2.3)

Total freeboard as a measurand is obtained by NASA ICESat and ICESat-2 satellite altimetry missions, and to some extent from Ka-band radar altimetry missions AltiKa, however, with a potentially larger penetration depending on snow conditions (see also Section 2.1.1). The total freeboard can be derived from Ku-band altimetry if the snow depth is known.

Crucial reference data has been collected by use of airborne laser altimetry including ESA CryoVEx and Cryo2IceEx campaigns and NASA Operation IceBridge (OIB). These measurements provide a reference for the penetration depth of radar altimeters and are typically used in combination of a snow radar (see Section 5.2.1.2 and 2.1.7) as is the case for OIB or airborne (Ku-band and Ka-band) radar altimeters, as is the case for ESA CryoVEx and Cryo2IceEx.

Snow depth refers to the thickness of the layer of snow lying on top of the ice floe. Snow depth varies spatially and temporally due to changes in precipitation patterns, and loss of snow to open water within sea (in ice leads) as well as due to changes in the sea ice cover caused by divergence (lead formation) or divergence (ridging and rafting of sea ice). Furthermore, increases in temperature can cause melt, which can wet the snowpack which impacts the radar penetration – and decreases in temperatures after melting within the snowpack can cause refreezing within the snowpack. This can create ice lenses and impact the reflective horizon of the spaceborne altimeters. However, snow depth is also an important quantity to know when converting from sea ice/total freeboard to sea ice thickness. It is therefore important to have as accurate a representation of snow depth as possible.

Spaceborne altimetry measurements have mainly used the Warren 99 climatology [RD114], which has been elaborated from in-situ data gathered over multi-year ice between 1954 and 1991 in the central Arctic, or its modified version from Kurtz et al. 2011 [RD56] to take into account the replacement of multiyear ice (MYI) by first-year ice (FYI). More recent work has been done on utilising spaceborne observations to compute snow depth or using reanalysis/model-based

estimates of snow depth. Results show that models and spaceborne estimates of snow varies in spatially and temporally – both amongst the models and when compared with observations (Zhou et al., 2021 [RD125], Garnier et al 2022 [RD27]), highlighting the challenge it currently is in producing accurate pan-Arctic snow depth maps. For airborne surveys, there are often instruments carried along that helps the retrieval of more accurate snow depths (e.g., snow radars, which will be described in more detail later), however snow depths from one part of the Arctic are rarely representative of snow depth in other parts of the Arctic. As such, snow depth remains one of the largest uncertainties in the sea ice thickness computation when utilising altimeter observations.

2.1.4   Sea ice thickness

Sea ice thickness (SIT) is the essential climate variable of primary interest when considering altimetry observations. Current estimates of sea ice thickness are computed from sea ice freeboard (FB_{ice}) and snow depth (SD) observations, and assume of hydrostatic equilibrium by the following equation:

$$SIT = \frac{\rho_w}{\rho_w - \rho_i} FB_{ice} + \frac{\rho_s}{\rho_w - \rho_i} SD \qquad (2.4)$$

where ρ_w, ρ_i and ρ_s denote the densities of sea water, ice and snow. Thus, from Equations (2.2) and(2.4), the SIT can be computed from the observed Ku-radar freeboard as following:

$$SIT = \frac{\rho_w}{\rho_w - \rho_i} FB_{Ku} + \frac{\rho_s - \rho_w(1 - c/c_s)}{\rho_w - \rho_i} SD \qquad (2.5)$$

In this equation, c/c_s depends on the snow density ρ_s. For instance, Ulaby et al. (1986) [RD107] suggest the following relationship: $c/c_s = (1 + 0.00057 \rho_s)^{1.5}$. Thus, SIT depends on 5 variables that can be considered as independent. In such a case, the square SIT uncertainty can be estimated as the sum of the square uncertainties of the 5 partial derivatives of Equation (2.5). This uncertainty equation is developed in Section 7.4.1.2 and instantiated with typical values from the Effects Table in Appendix B.

This equation (2.5) is valid under the assumption that Ku-radar fully penetrates the snow. This hypothesis can be wrong in some cases, for instance for salty or wet snow [Nandan et al. (2017) [RD78]]. If the altimeter wave does not penetrate the snow, as it is the case for laser altimeters, we would have $FB_{total} = FB_{ice} + SD$ which becomes, when combined with (2.4),:

$$SIT = \frac{\rho_w}{\rho_w - \rho_i} FB_{total} + \frac{\rho_s - \rho_w}{\rho_w - \rho_i} SD \qquad (2.6)$$

The densities are obtained from older measurements, as discussed in Section 2.2.

2.1.5   Sea ice draft

Sea ice draft refers to the part of the sea ice submerged below water. Sea ice draft cannot be observed directly from altimeters, since the altimeter observations will be reflected at either the ice floe or open water surface. However, the sea ice draft parameter is often measured by in situ observations using under water moorings, or buoys equipped with underwater electronic 'fish' (see Ice-T buoys data, Section 5.2.2.6). These draft measurements are very pertinent to estimate the freeboard because they directly measure about 90% of the sea ice thickness. Therefore, a conversion from altimetric observations to sea ice draft is commonly required. This conversion can be easily deduced from the previous equations (2.4), (2.5) or (2.6) from the draft D definition: $D = SIT - FB_{ice}$

For instance, equation (2.4) becomes:

$$SIT = \frac{\rho_w D - \rho_s SD}{\rho_i} \qquad (2.7)$$

2.1.6   Total thickness (snow + ice)

Total thickness is defined as the sum of the thickness of the sea ice floe and the overlying snow depth layer. Total thickness cannot be retrieved directly from altimetry measurements, since the altimeter measures either radar freeboard or total freeboard (depending on frequency of the altimeter). However, total thickness is a parameter often measured by validation campaign when using electromagnetic (EM) sounding, which requires no mean of assumptions regarding penetration into snowpack since it gives a combined (total) ice thickness measure.

Thus, it is necessary for altimetric measurements of sea ice floes (either radar freeboard or total freeboard) to be combined with another parameter, typically snow depth or sea ice draft to properly compare them with the reference observations of total thickness. This conversion can be easily deduced from the previous equations(2.4), (2.5) or (2.6) from the total thickness definition:

$$SIT_{\text{total}} = SIT + SD.$$

(2.8)

2.1.7   Snow depth

It is clear, that for every single altimetry-relevant parameter mentioned here, one particular parameter is key: the snow loading on top of the ice. It is necessary to convert between total freeboard (from laser) and radar freeboards (Ka-band, which is commonly assumed to reflect the total freeboard, or Ku-band) to sea ice freeboard, is pivotal in the conversion from sea ice freeboard to thickness, as well as is included in the total thickness derived from EM sounding. Snow depth refers to the thickness of the layer of snow lying on top of the ice floe. Snow depth varies spatially and temporally due to changes in precipitation patterns, and loss of snow to open water within sea (in ice leads) as well as due to changes in the sea ice cover caused by divergence (lead formation) or divergence (ridging and rafting of sea ice). Furthermore, increases in temperature can cause melt, which can wet the snowpack which impacts the radar penetration – and decreases in temperatures after melting within the snowpack can cause refreezing within the snowpack. This can create ice lenses and impact the reflective horizon of the spaceborne altimeters. However, snow depth is also an important quantity to know when converting from sea ice/total freeboard to sea ice thickness. It is therefore important to have as accurate a representation of snow depth as possible.

Spaceborne altimetry measurements have mainly used the Warren 99 climatology [RD114], which has been elaborated from in-situ data gathered over multi-year ice between 1954 and 1991 in the central Arctic, or its modified version from Kurtz et al. 2011 [RD56] to take into account the replacement of multiyear ice (MYI) by first-year ice (FYI). More recent work has been done on utilising spaceborne observations to compute snow depth or using reanalysis/model-based estimates of snow depth. Results show that models and spaceborne estimates of snow varies in spatially and temporally – both amongst the models and when compared with observations (Zhou et al., 2021 [RD125], Garnier et al 2022 [RD27]), highlighting the challenge it currently is in producing accurate pan-Arctic snow depth maps. For airborne surveys, there are often instruments carried along that helps the retrieval of more accurate snow depths (e.g., snow radars, which will be described in more detail later), however snow depths from one part of the Arctic are rarely representative of snow depth in other parts of the Arctic. As such, snow depth remains one of the largest uncertainties in the sea ice thickness computation when utilising altimeter observations.

Of particular interest for altimetry sensors is the dual-frequency approaches to estimate snow depth, using either laser or Ka-band as a reference of the air-snow interface, as well as Ku-band as a reference of the snow-ice interface. Then, snow depth can be derived by differencing the radar freeboards and correcting for slower wave propagation speed. Alternatively, frequency-modulated continuous-wave (FMCW) "snow-radar" systems have also been deployed on aerial platforms, from which the air-snow and snow-ice interfaces are re-tracked directly from the altimeter observations given the frequency-range allows for penetration to the snow-ice interface while also having significant scattering from both interfaces to be retracked. Here, a correction for slower wave propagation speed is also applied following:

$$SD = \frac{(h_{air-snow} - h_{snow-ice})}{\eta_s}.$$

Here, η_s is refractive index of a radar wave travelling through snow and is given by $\frac{c}{c_s}\rho_s = (1 + 0.51\rho_s)^{1.5}$ following Ulaby et al. 1986 [RD108], and $h_{air-snow}$ and $h_{snow-ice}$ refers to the elevation of the air-snow and snow-ice interface (which can be given either by ellipsoidal heights, freeboards, or even as range-estimates).

2.2 Auxiliary parameters

2.2.1 Surface classification

Surface classification is a crucial step of the freeboard estimation using altimetry as it allows to make the distinction between leads and ice floes whose height difference provides the freeboard. Leads in winter are always covered with a thin layer of ice and present a considerable specularity which results in a backscatter several dB higher than normal and very peaky waveforms. On the other hand, because of its roughness and the attenuation due to the snow, the backscatter of the ice is more diffuse and results in waveforms closer to what can be observed over open ocean. Thus, the most common method is to compute the peakiness (i.e., the maximum value divided by the mean value) of this waveform and define thresholds for the attribution to one or the other class. However, there are still ambiguities, especially on the edges of the ice pack and for the warmer seasons. Thus, different variants have been proposed. They consist in combining several characteristic parameters of the waveform, beyond the peakiness: the backscatter, the leading edge width, the range integrated power, etc. The complexity thus induced requires the use of clustering [Paul et al. 2018] or neural networks [Poisson et al 2018 [RD86]] techniques. A few approaches exploit spatial images collocated with altimetry to automate class learning [Passaro et al. 2017 [RD80], Landy et al 2022 [RD66]]. However, this technique is very cumbersome as it requires image segmentation. Thus, spatial images are still mainly used for a visual (non-automatic) validation of few classification samples.

2.2.2 Surface roughness

Due to the heterogeneous and dynamic nature of the sea, where sea ice is a medium composed of sea ice floes varying in thickness and size, while also being covered in rubble fields, pressure ridges, and snow features such as sastrugi and dunes, surface roughness observations is also of great interest. Variations in the surface roughness tends to impact the shape of the satellite altimeter waveform, which again impacts the waveform retracking point, depending on the retracker used. Elevations extracted from commonly used retrackers such as the TRMFA, are affected by the surface roughness, and studies dedicated to correcting the retracked elevations for the surface roughness are needed. Physical retrackers on the other hand takes the surface roughness into account but needs input data of the surface roughness. Elevations from airborne or drone swath lidars can be used to produce roughness estimates and to calibrate roughness on satellite scales (MacGregor et al., 2021 [RD70], Beckers et al. (2015) [RD13]). Furthermore, the fine-resolution footprint and accuracy of such data can detect pressure ridge sails, which are otherwise difficult to observe with satellite altimetry. Finally, analysis of the entire Arctic Sea ice height record from ATM data demonstrated how sea ice heights exhibit a more lognormal, as opposed to Gaussian, height distribution. This information was fed to a new physical re-tracker applied to radar altimeter observations from CryoSat-2 to provide improved elevation observations (MacGregor et al., 2021 [RD70]).

2.2.3 Sea ice densities

Sea ice densities are related to the stage of development i.e., the sea ice type, and the deformation. Typically, for satellite altimetry we only differentiate between first year (FYI) and multiyear ice (MYI). MYI has typically lower densities when compared to FYI, as MYI has drained out the brine, which has been replaced with less dense air bubbles. Typically, densities of sea ice have been estimated to be 882.0 ± 23.0 kg/m^3 and 916.7 ± 35.7 kg/m^3 (Alexandrov et al. 2010 [RD6]) for MYI and FYI, respectively. A more up to date study by Ji et al. (2021) [RD143] suggests that the measured sea ice densities during the time period 2000-2015 has a wider range (monthly means varies from 832 kg·m^{-3} to 916 kg·m^{-3}) than the values before the 21st century. They suggest updating the sea ice densities for retrieving Arctic Sea ice thicknesses from satellite altimetry missions accordingly. A sensitivity analysis of the freeboard-to-thickness conversion by Kern et al. (2015 [RD47]) suggests that to obtain sea ice thickness as accurate as 0.5 m from radar altimetry, besides a freeboard estimate with centimetre accuracy, an ice-type dependent sea ice density is as mandatory as a snow depth with centimetre accuracy. Thus, auxiliary information of classification of sea ice types are needed. Typically, OSI-SAF sea ice types from scatterometry missions are used. However, misclassification can have a significant impact on the sea ice thickness uncertainty budget. Besides in situ observations, airborne data from combined AEM and snow radar has been used to estimate sea ice densities on more regional scales (Jutila et al. 2022 [RD46]).

2.2.4 Snow densities

A common approach is to use the snow densities from the Warren Climatology (Warren et al., 1999 [RD114]). Several studies, have found these values to be well representative for current snow densities in the central Arctic. Outside the central Arctic where extrapolation of the Warren snow densities is invalid e.g., in the Fram Strait, Barents Sea and the Svalbard coastal areas, local climatologies has been produced using local in situ data (Forsström et al. 2011 [RD25]).

2.3 Sources of uncertainty in the satellite altimeter measurement

A full analysis of satellite observation uncertainties is beyond the scope of this project and is being considered in projects such as FDR4ALT (https://www.fdr4alt.org). However, a short overview is provided, as it supports thinking of priorities for Cal/Val activities.

Processing of the satellite observation starts with an identification of the sea level anomaly (SLA) of the leads and the ice level anomaly (ILA) of the floes. The first step towards this is to measure the radar range, *i.e.,* the heights over the leads and floes using a retracker. Over leads and ice, the returned waveform has a very different shape to the returned waveform from open ocean, and therefore specialist retrackers are used, or an 'adaptive retracker' is used which can process open ocean and sea ice areas in a way that smooths the transition between the two regimes. The lead and floe retrackers are usually threshold retrackers. They consist in identifying the main peak in the returned waveform and measuring the range on the leading edge of the waveform as the value that corresponds to a given percentage (typically 50%) of the main peak power. There are significant sources of uncertainty associated with this heuristic retracking process, especially in the identification of the 'main peak' over ice, and due to the impact of the radar sidelobes and off-nadir echoes.

The retracked heights are corrected for atmospheric and tide corrections, and then compared to an interpolated mean sea surface to give the SLA (called ILA over ice floes). The SLA is then interpolated below the ice floes and subtracted from the ILA to obtain the radar freeboard. There are uncertainties associated with the MSS and with the atmospheric and tide corrections. However, the (unknown) errors associated with these corrections will almost completely cancel out between the SLA and ILA (i.e. although there is an uncertainty associated with these corrections, that uncertainty leads to an unknown error that is almost identical between those two measurements). The residual uncertainty due to the minor variation over the relevant distances and timescales is very small.

Much more significant uncertainties are caused by the processing of these measured freeboards (later on called "radar freeboard") into sea ice freeboard and sea ice thickness. As described in Section 2.1, these analyses involve bringing in information about the snow depth, the penetration depth of the Ku band radar into the snow, and the densities of snow, ice and water. The data used for these analyses is, by necessity, simplified and based on a small number of measurements and a climatology.

Well-designed Cal/Val processes, that compare the satellite observations with measurements by other satellites (including those with different frequencies) and with FRMs, can help test scientists' understanding of these processes and sources of uncertainty. This is discussed in Section 3.

3 Calibration/Validation framework for sea ice

3.1 Special considerations for sea ice

Historically, the purpose of space altimetry was to measure sea level. This application was then extended to lake and river levels and to polar ice cap topography. For all these applications, the objective was to measure a height relative to a reference ellipsoid and to study its variations over time. For all these cases, Cal/Val procedures consist in ensuring that the measured height is consistent with the theoretical height, and that the usual methodology consists in making measurements on reference sites at the vertical of the satellite trajectory where reliable in-situ measurements are available – generally by means of high precision GNSS sensors. The site itself can be equipped with a radar reflector to make the radar echo even more precise and discriminating.

The use of altimetry to measure sea ice thickness in an operational way is a more recent application because it raises several problems. In particular, the objective here is no longer to measure a height, but a thickness that is not directly perceptible by altimetry, and that involves many other parameters such as snow depth, water, ice and snow densities, and so on.

Thus, we no longer have a means of direct comparison between dimensions of the same nature (height). We have on one side measurements of ice freeboard as perceived by the altimeter, and on the other side measurements of physical dimensions of the ice pack such as ice thickness, freeboard or draft, or snow depth.

Beyond this problem of different nature of the satellite altimetry measurements and the physical measurements in the field, the pack ice also poses the problem of its accessibility and its strong dynamics, which prevent the use of fixed equipment (except for moorings that measure the draft, provided there are no icebergs) and limit the reliability of "occasional" measurements (in-situ, aircraft, boat, buoys, drone) to a very small time interval around the measurement (few hours).

Because of these different constraints, Cal/Val techniques on pack ice are very specific. They must be based on a diversity of measured quantities, and therefore of sensor types, and on statistical approaches to counter the inevitable spatial and temporal differences between satellite measurements and local reference measurements.

3.2 Calibration and validation as a comparison process

Calibration and validation use other independent observations in comparison with measurements by the satellite altimeter in order to test the altimeter observations. Such comparisons can be made against observations by other satellites or observations from non-satellite methods (e.g., in situ, aircraft, drones, moored buoys). The results of such comparisons can be interpreted in three different ways:

a) A comparison can be used to validate that observation values are within an expected tolerance
b) A comparison can be used to evaluate the uncertainty associated with the satellite observation
c) A comparison can be used to validate independently-determined uncertainties.

Traditionally, comparisons have been used for approach (a), i.e. to monitor whether satellite and reference measurements agree within the satellite's specified requirements. More recently, approach (b) or (c) has been attempted.

In a comparison, it is necessary to consider uncertainties associated with

(1) The reference / compared observations
(2) The satellite altimeter observations
(3) The comparison process itself

Uncertainties associated with the comparison process itself include uncertainties related to the fact that the reference measurements and the satellite observations may be different, or uncertainties related to processing steps used to make the two measurements more equivalent (for example, by scaling or sampling observations to a common grid, or converting a radar freeboard into a lidar freeboard).

If the uncertainties associated with (1) the reference observations and (3) the comparison process themselves are much smaller than (2) uncertainties associated with the satellite altimeter observations, then the comparison can be used for approach (b), i.e., the comparison can be used to calculate/evaluate the uncertainty associated with the satellite measurements.

A metrological approach to comparisons would follow approach (c). That is, the three types of uncertainty associated with the two measurements (satellite and non-satellite) and the comparison process are independently evaluated and then the comparison is used to validate the uncertainties. It is for this reason, that the FRM needs an uncertainty evaluation independently determined and that we need to consider the uncertainty associated with the comparison process itself.

3.3 Calibrations for sea ice

3.3.1 What comparisons can be performed

One of the most important considerations in choosing an FRM is to decide what measurand the FRM should measure. As discussed in Section 2.1, the satellite altimeter does not measure 'sea ice thickness', but surface heights, from which sea ice thickness can be derived with auxiliary information. An ideal Cal/Val programme will therefore consider comparisons that can be performed at different stages of the derivation.

Figure 3.1 shows a 'comparison diagram' for sea ice measurements. On the left there is the value chain for sea ice measurements from a satellite altimeter, which starts with the level 1b waveform (bottom), which is retracked to obtain ranges (over leads and floes), which are corrected to give the surface height anomaly (SHA) and then the radar, and sea ice freeboards. This is the first point where a comparison can be made. Other Ku band instruments, whether on another satellite or on an aircraft, can be directly compared for Ku-band radar freeboard, and Ka-band radar (assuming no penetration) and lidar instruments (from satellites, aircraft or drones) can be compared with the total freeboard.

The data are then processed to give sea ice thickness, which is the quantity that can be compared with most in situ observations, and from sea ice thickness, the sea ice draft can be calculated. The sea ice draft can be compared with underwater measurements.
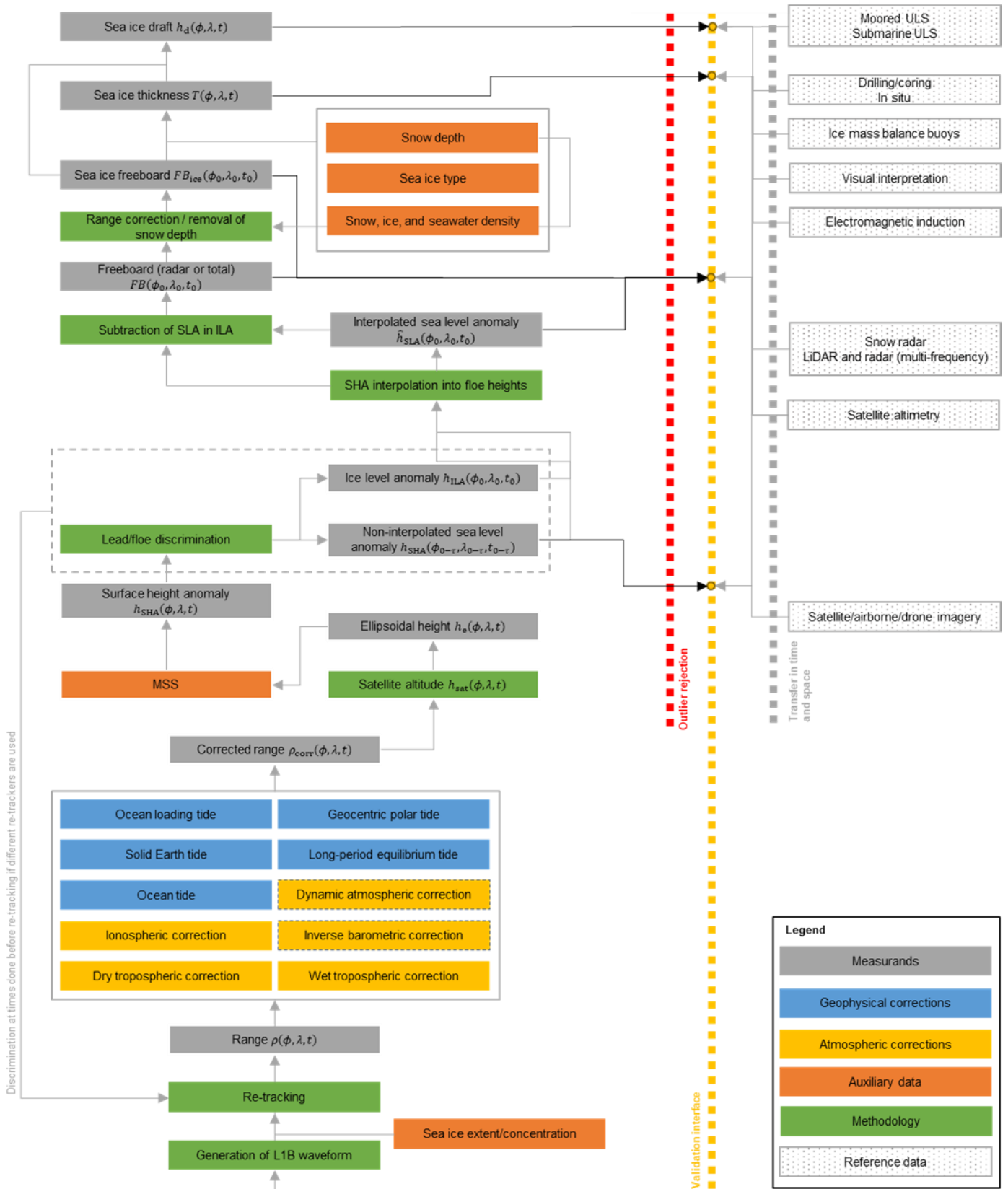
Figure 3.1: A comparison diagram for sea ice measurement parameters, showing the satellite altimeter measurements (left) and the different comparisons that can be performed (right).

3.3.2   Comparison representativeness and uncertainty

Section 3.3.1 has discussed how different Cal/Val approaches perform the comparison at different stages of the processing chain. It is also important to consider what area of surface the observations represent.

Figure 3.2 shows a generic validation scenario. The dashed red line denotes the actual satellite track, since the nominal (predicted) tracks, shown in black, and actual tracks rarely are identical. Over sea ice, both moored sensors (stationary, moored to the sea bottom) are available as well as stations moored/fixed to an ice floe (that moves with the ice pack). A stationary (moored) position measures the changing sea ice cover at that position, whereas a fixed station (to the ice floe) measures the changes that the specific ice floe observes. Furthermore, we have several types of moving sensors - either following dedicated satellite passes (campaign data using e.g., helicopters, aircraft, drones) or non-dedicated sensor passes (ships, drones covering a general area, potentially underwater vehicles etc.). Non-dedicated moving sensor passes rarely cover the actual or nominal satellite pass completely. The same applies for the fixed (whether stationary or to an ice floe) stations. Due to the complexity of such a validation scenario, we shall discuss in more detail what can be validated from satellite and compared with in situ observations, and how these observations are usually made comparable through different post-processing procedures.
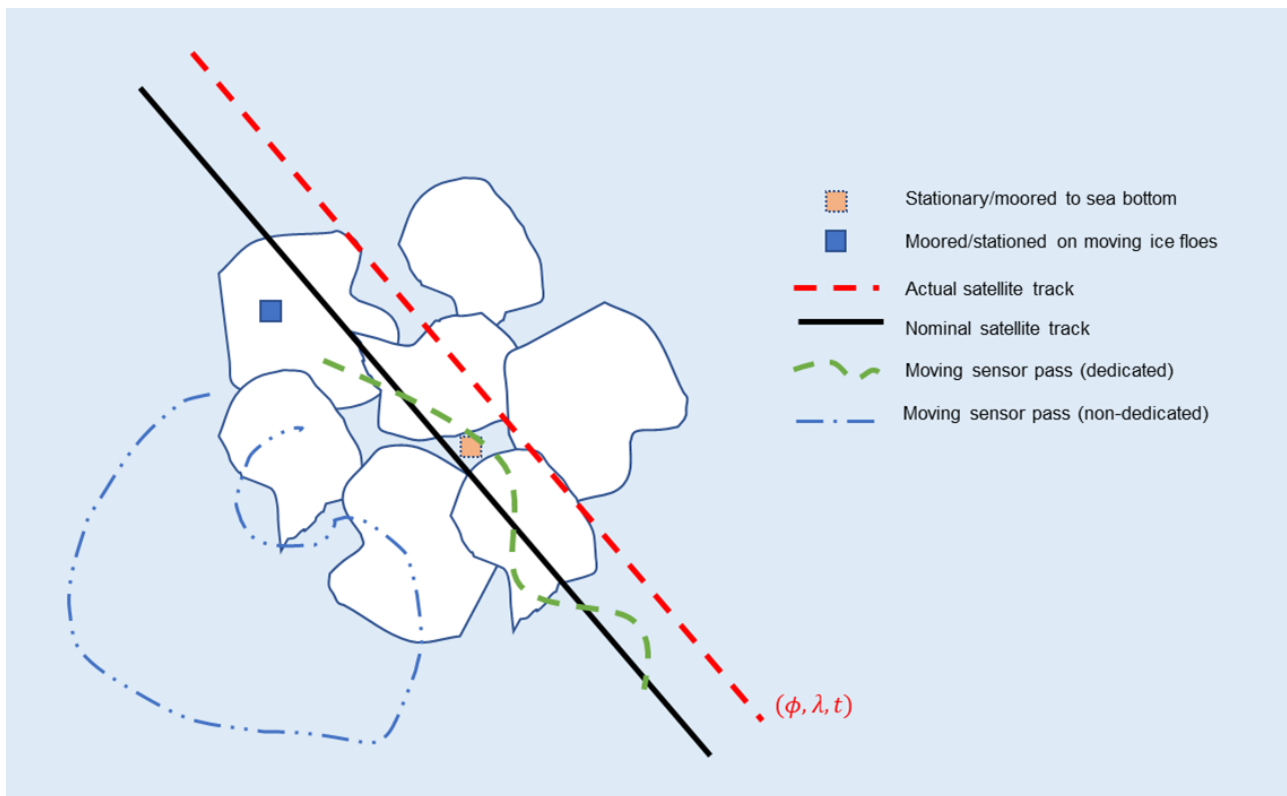

Figure 3.2: Schematic view of a generic scenario for collecting satellite altimetry and in situ data over moving/changing sea ice conditions

Over sea ice, we aim to validate the altimeter's ability to measure freeboard, i.e. the height of the sea ice above the local sea level, provided at a specific sampling rate thus having geodetic and time coordinates (ϕ, λ, t). The processing algorithm to retrieve freeboard is shown in Figure 3.1. However, selecting which measurand is of interest for validating the satellite observations over sea ice is not trivial. We can select multiple instances during data processing where data validation can be performed with different measurands, as described in Section 3.3.1.

Often the FRMs are not directly comparable with TDPs (thematic data products, i.e. one of the measurands in the processing chain). Generally, every set of in situ data must go through some post-processing procedure to ensure comparability with a specific measurand (or vice versa). This must be considered for a fully meteorological approach in the assessment of uncertainties.

It should be noted, that the procedures to ensure comparability do not have to be associated with the FRM procedures - frankly, they often occur for both TDPs and FRMs. A number of procedures are applied to the TDPs to reach an equivalent of the altimetric measurement using FRM. These post-processing procedures depend on the type of

reference measurement and whether they are spatially and temporally collocated. Figure 3.3 shows the most common post-processing procedures used in sea ice depending on whether we are using moving/fixed stations and whether products from altimeters are provided in the original format (along-track) or gridded (processed data).
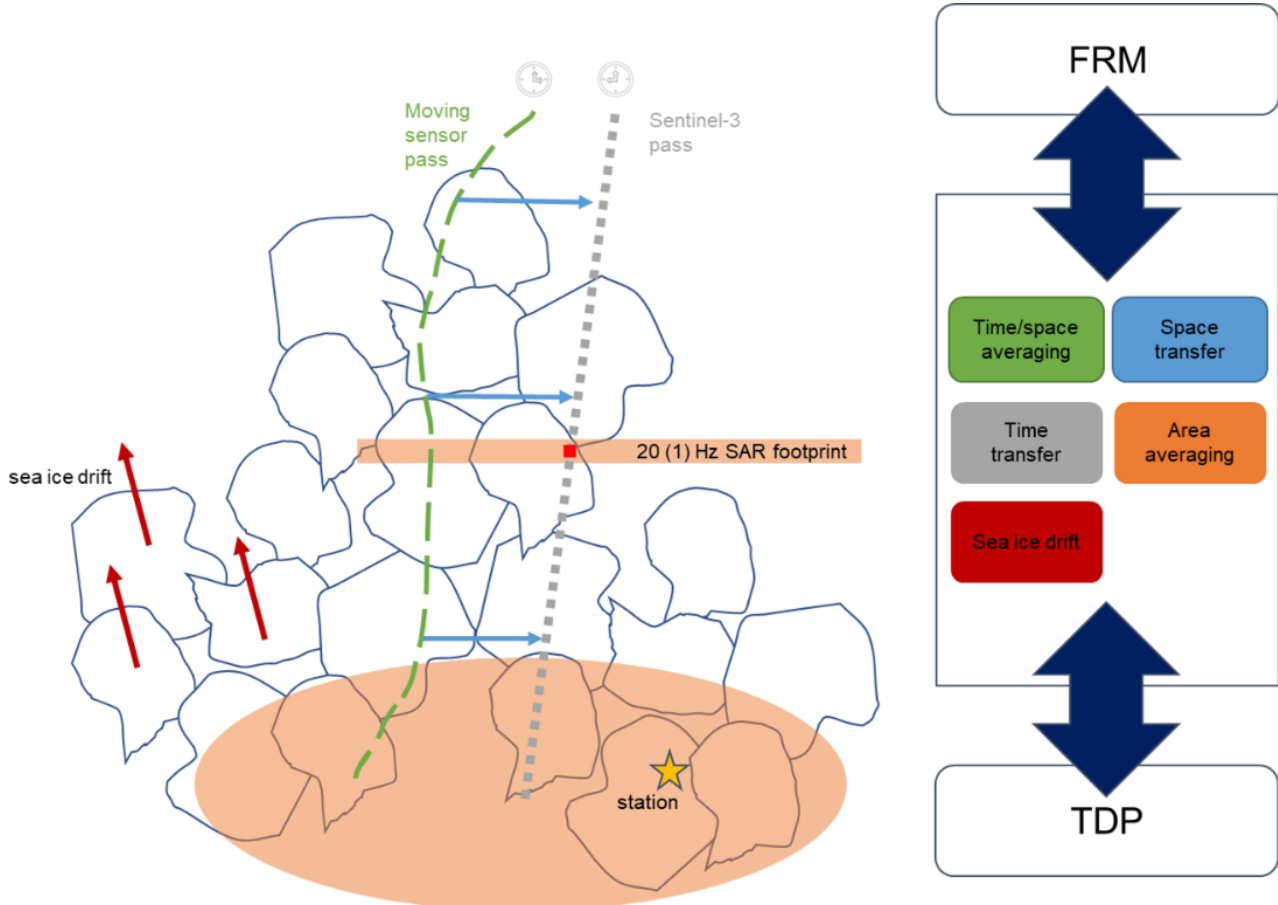

Figure 3.3: Deriving altimetry equivalent observations through various post-processing steps - either by applying to TDP or FRM

We shall describe it in more detail below:

- Time/space averaging: It may be necessary to sample either the reference data or TDP by averaging to ensure comparability. This is often the case for both fixed and moving sensors, as they will not be comparable otherwise. Especially for TDP, this can reduce noise related to speckle from the waveforms, but too much averaging can remove local topography (ridging of sea ice) which may be of interest. Therefore, care should be taken when smoothing data.

- Space transfer: Reference and satellite observations are rarely perfectly collocated. Space transfer is the procedure to shift the reference (or TDP) data to where the comparison data is located. However, it is important to consider what the TDP is actually observing and how this is comparable with the comparison data. The TDP location is truly only an approximation of the back-scattering points within some effective footprint. The footprint will include several types of sea ice (ridged and flat ice, open water, snow covered- and non-snow covered, wet snow, dry snow etc.), which all impacts the satellite observations and therefore also the retrieved variables. How one makes the TDP comparable with the reference observations (or the other way around) is therefore not straightforward when it comes to sea ice.

- Time transfer: Reference data and satellite data are also rarely collected concurrently, and even if they are, the temporal sampling is rarely the same. Thus, it would be necessary to transfer the reference/TDP samples to that of the comparison data. However, for sea ice, it is important to consider that sea ice changes all the time. Therefore, transferring observations of sea ice captured by a moving

sensor a few hours before even over exactly the same location will likely not yield similar data, since the sea ice will have moved due to constant motion. Here, it is again important to consider what is truly being compared, and what is comparable.

- Area averaging: One must remember that validations are conducted in relation to a specific measurand. This means that both TDPs and FRMs should present an identical measurand. However, even averaging over and transferring in space and time may not be enough if the different observations do not cover similar areas. And, since sea ice is changing quickly over short distances, it is important to consider what is comparable and similar.

- Sea ice drift: sea ice is dynamic and flows along with the wind and currents of the ocean, which impacts the location of the floes and the dynamics of the sea ice (opening of sea ice floes, ridging of floes when pushed together etc.), thus it may change the sea ice thickness distribution with time. It is important to consider the sea ice drift when comparing observations acquired at different times, and sometimes it is not enough to simply average over time, but rather a manual or automatic direct correction/elevation comparison must be conducted to ensure that the drift has been accounted for in the comparison.

All of these aspects should to the best of abilities be reflected in the uncertainty of the measurand either by conducting measurements of the uncertainty, collecting expert judgement or approximating by modelling.

4 Requirements for Cal/Val altimetry measurements of sea ice

4.1 Types of measurements to include in an FRM suite

As discussed in Section 3.3, it is important to consider different measurands of the satellite observation processing chain for comparison to validate the whole observation process. Radar freeboard measurements can most directly be compared with other Ku-band observations, from another satellite and/or from an aircraft. Observations from another satellite are not FRMs but can be useful in the Cal/Val process. Aircraft observations are valuable, especially where a Ku band radar can be operated alongside Ka band radar or lidar, which provide a measurement of the total freeboard, and where they underfly the satellite.

In-situ measurements provide measurements of the desired sea ice thickness quantity and are therefore important to validate the processing algorithms that convert the radar freeboard into sea ice thickness. Moored underwater observations measure the sea ice draft, which is related to sea ice thickness in a similar way to freeboard (analysis should use the same densities for ice, water and snow), and therefore is also an important part of an FRM suite.

As these different observations perform different functions, there will be no one FRM for sea ice thickness. Instead, we should consider a suite of observations from these different technologies that together perform the function of an FRM.

4.2 Campaigns vs semi-permanent observations

In other Earth science disciplines, it is possible to establish permanent reference sites that are used for calibration and validation, such as the RadCalNet desert sites used for radiometric sensor Cal/Val, the vegetated "super sites", and ocean colour moorings. The way sea ice drifts means that a permanent site for sea ice is impossible (with the exception of a few ocean floor upward looking stations). Semi-permanent sites, such as buoys embedded in the ice floes can provide seasonal information and travel with the ice. Campaigns, whether with aircraft or from ships, provide one-off detailed spatial information at a single time.

Because of the challenging nature of observations in polar regions, it is important to combine information from permanent and semi-permanent sites and from campaigns.

4.3 FRM quality and other observations

The definition of an FRM (Section 1.3) sets high expectations for FRM-quality measurements. They should be traceable to a community agreed reference (preferably SI) and come with robust uncertainty analysis. These requirements are both important and challenging. It is only with FRM-quality observations that we can perform comparisons to validate satellite observation (and processing) uncertainties (type c comparisons as described in Section 3.1) and therefore support the applications that use sea ice thickness data quantitatively (e.g. in climate modelling and reanalysis).

However, a full FRM-quality analysis of the uncertainties of Cal/Val techniques can be expensive and time-consuming, and for some historical data could be impossible if the full information is not available. Furthermore, the dominant uncertainty in such a Cal/Val process often comes not from the observational uncertainty, but from its representativeness, which means more, poorer quality data over a larger representative set of conditions can be preferable to a smaller set of higher quality data over just a few locations / times. Given the limited available information over the challenging polar regions, all data is of value.

It is therefore important to be pragmatic and to consider a Cal/Val process as using information from both FRM-quality and other Cal/Val data sources. It is, however, important for this distinction to be very clear to those performing these Cal/Val analyses.

5 Existing means for CAL/VAL activities

5.1 State of the art of existing sensors with ranking and discussion on their FRM compliancy

As an overview we provide a Sankey diagram (Figure 5.1) showing four categories; sensor type, platform, campaigns, derived geophysical variables, and their dependencies. In the following sections each of the categories are described.
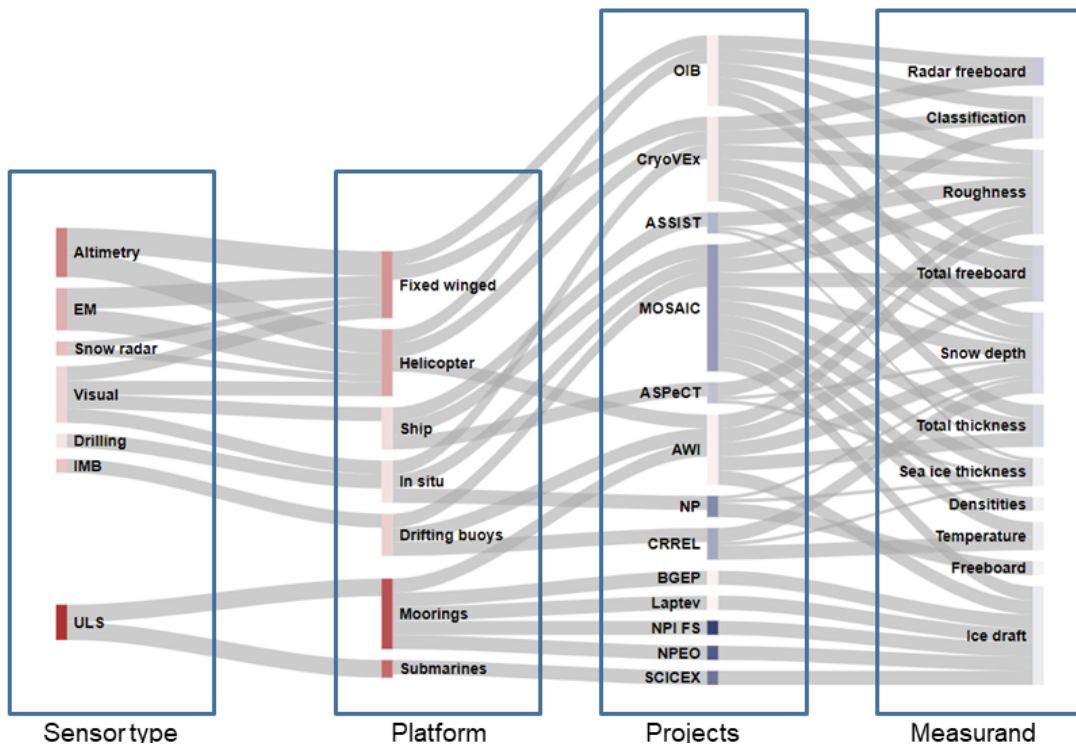

Figure 5.1: Sankey diagram showing four categories; sensor type, platform, projects, the associated measurand, and their dependencies.

5.2 Literature review of sea ice altimetry validation data from airborne, shipborne and in situ sensors

5.2.1 Airborne campaigns

Airborne sensors can offer complementary information with much finer spatial resolution than spaceborne measurements and wider coverage with respect to in-situ observations. Most commonly used sensors for sea ice thickness validation studies are radar and laser altimeters which provide information of freeboard heights and snow depths depending on the operating frequency and bandwidth. The EM-sensor also allows to acquire total thickness (ice + snow) information.

Beyond these key instruments we also have various optical/infrared/hyperspectral imagery systems used to either validate the other airborne observations - surface classification (such as for identification of leads or ice ridges) or for different sciences or other studies.

Below is provided a more detailed study of each state-of-the art sensor.

5.2.1.1 Airborne laser scanners

In the table below is provided a review of most commonly used laser scanners for airborne campaigns in polar regions. Some of these have been more extensively used and are described in more detail below.

Sensor	Airborne Laser Scanner	Airborne Topographic Mapper	Bathymetric & Topographic LiDAR	Land, Vegetation, and Ice Sensor	Airborne laser scanner
Instrument ID	ALS	ATM	BTL	LVIS	ALS
Manufacturer	REIGL	NASA	Leica	NASA	RIEGL
Type	LMS-Q240i-60LMS-Q240i-40	T2-T7	Chiroptera-4X	LVIS	VQ-580 VQ-580II
Functionality	Rotating scanner	2 Conically scanning laser altimeters	Oblique scanner	Wide-swath imaging laser	Rotating scanner
Frequency	NIR 904 nm	Green	Green NIR	1064 nm	1064 nm
Maximum Range	600 m	800 m	1600 m AGL	20 km	1200 m depending on PRR
Sampling rate (PRF)	10 kHz	3-10 kHz	140 kHz 500 kHz	4 kHz	50-380 kHz
Nominal Swath Width	3-400 m @ 300 m AGL	245, 40m @ 460 m AGL	70 % of AGL 700 m @ 1000 m AGL	2 km @ 10 km AGL	1150 m @ 1000 m AGL
Project	ESA CryoVEx	NASA Operation IceBridge	NASA ICESat-2 Cal/Val Summer 2022	NASA: Operation IceBridge +	AWI IceBird

Airborne Topographic Mapper (ATM): is a green-wavelength conically scanning laser altimeter. ATM has surveyed terrestrial topography for decades and has had a primary focus on the cryosphere since 1993 (Krabill et al., 1995 [RD51]), and has been operating during OIB since 2009 and throughout. The main components of ATM are two conically scanning laser altimeters that both measure the surface elevation independently along the path of the aircraft at 15° and 2.5° off-nadir angles, respectively (Krabill et al., 2002 [RD50]). At OIB-nominal AGL, the 15° and 2.5° scanners have swath widths of 245 and 40 m, respectively, with a near-constant angle of incidence, and intersecting tracks of laser footprints from the conical scan geometry allows for determination of pointing biases over any type of surface (Harpold et al., 2016 [RD37]; Martin et al., 2012 [RD72]). During OIB, six generations of ATM transceivers and three generations of data systems were used, along with four different lasers (with pulse-repetition-frequency (PRF) ranging from 3 to 10 kHz). The laser footprint varied in diameter between 1.2 and 0.6 m over the course of OIB at nominal AGL (MacGregor et al., 2021 [RD70]). The aircraft's position was determined by GNSS (that incorporated GPS, and later GLONASS), which was used to derive the precise surface elevations. In addition to this, two INS's were used to attitude determination over the course of OIB. Various assessments have been conducted to derive the accuracy of the measurements including analysing various sources of errors (Martin et al., 2012 [RD72]), comparing with GNSS ground observations over the interior of the Greenland and Antarctic ice sheets (Brunt et al., 2017, 2019 [RD16]), and comparing over sea ice (lead observations) (Farrell et al., 2012 [RD23]).

Several methods for determining sea ice freeboard from OIB has been developed (Connor et al., 2013 [RD18]; Farrell et al., 2015 [RD22], 2011 [RD24]; Kurtz et al., 2013 [RD55], 2009 [RD57]; Kwok et al., 2009 [RD63]; Wang et al., 2016 [RD112], 2013 [RD113]; Yi et al., 2014 [RD124]). All of these methods generally involve differencing the local sea surface elevation from the sea ice elevation determined from ATM measurements, where the ATM returns over sea ice are expected to track the air-snow interface (the total freeboard) with minimal penetration into the snowpack. Lead locations (where the local sea surface elevations were acquired from) were identified primarily with coincident visible imagery. Kurtz et al. (2013) [RD55] used the Sea-Ice Lead Detection Algorithm using Minimal Signal (SILDAMS) algorithm applied to DMS imagery, which allows for classifying and locating leads, while also co-locating these with the ATM elevation data. Other lead-classification methods used a combination of ATM elevation, reflectivity and waveform parameters (Yi et al., 2014 [RD124]), or by using ATM elevation and reflectivity histograms (Kwok et al., 2012 [RD62]), and also compared with visible imagery. These observations are extensively used to assess the quality of freeboard observations from satellite observations such as e.g., ICESat, ICESat-2, CryoSat-2 and AltiKa (e.g., Connor et al., 2013 [RD18]; Kwok et al., 2019 [RD59]; Kurtz et al., 2014 [RD54]; Armitage et al., 2015 [RD9]).

Arctic sea ice thickness has been derived from OIB in multiple studies (e.g., Farrell et al., 2012 [RD23]; Kurtz et al., 2013 [RD55]; Richter-Menge and Farrell, 2013 [RD91]), and although their results differ somewhat, their spatial patterns and interannual variability are similar and consistent with prior understanding of sea ice thickness distribution in the Arctic Ocean. OIB sea ice thickness products have also served as an important tool to assess the observations derived from satellites including ICESat, CryoSat-2, ICESat-2 and multi-sensor thickness assessment (e.g., Connor et al., 2013 [RD18]; Sallila et al., 2019 [RD97]; Stroeve et al., 2014 [RD103]).
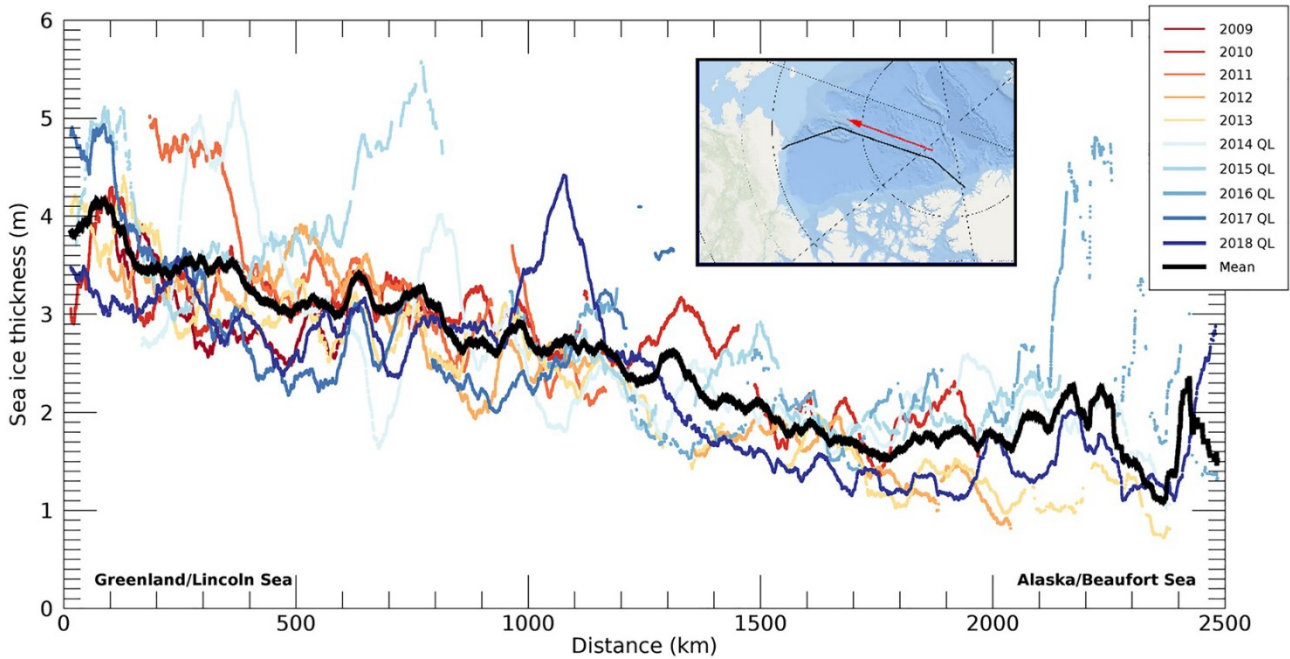
Figure 5.2: OIB PSO product sea ice thickness, smoothed with a 50 km boxcar average for Laxon Line surveyed during 2009-2018 Arctic spring campaigns. QL: Quick Look (adapted directly from MacGregor et al., 2021 [RD70]).

LVIS: The LVIS instrument suite includes a wide-swath, high-altitude airborne laser altimeter and a camera producing elevation and surface structure measurements of land, water and ice surfaces. With its full waveform, 1.064 nm wavelength laser it records both the outgoing and reflected laser pulse shapes, thus providing a three-dimensional record of the surface with a precision in the level of centimetres (Blair et al., 1999 [RD15]). LVIS maps with a 12° wide (about 2 km at 10 km AGL) swath centred on nadir using several technologies, and several versions of LVIS were flown for OIB, representing progressive improvements in observations strategy and system design (v1 - 2009-2010, footprint of 20 m, PRF of 1 kHz, v2 - 2010-2015, footprint of 20 m, PRF of 1.5 kHz, GH - 2013, footprint of 10 m, PRF of 2.5 hKz, Facility - 2017, footprint of 10 m, PRF of 4 kHz).
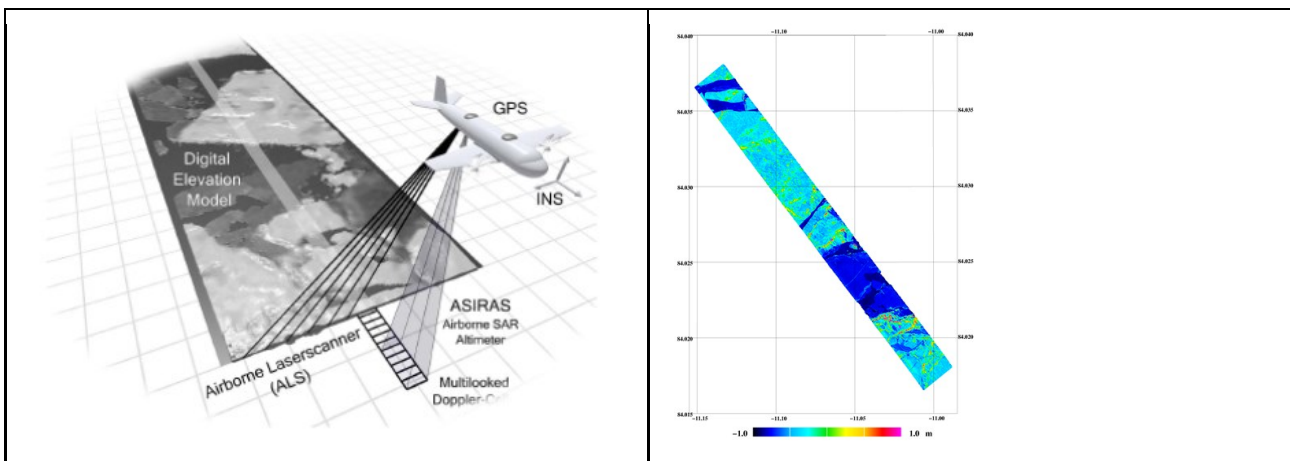
Figure 5.3: Principles of airborne swath scanner (ALS) using rotating mirrors, and ASIRAS airborne ku-band radar along a survey flight (left). Final surface topography with respect to DTU15 MSS demonstrating the high details and also the complexity of sea ice on small scales (300m x 2500m).

Airborne laser scanner (ALS) of type RIEGL LMS-Q240i-60/LMS-Q240i-80 uses 4/3 rotating mirrors, which results in a swath of parallel scan lines on the surface with a maximum scan-angle of 60° /80°. The ALS operates with wavelength 904 nm, which is expected to reflect on the air-snow surface. The pulse repetition frequency is 10,000 Hz and the ALS scans 40 lines per second, thus the data rate is 251 pulses per line. This corresponds to a horizontal resolution of 0.7 m

× 0.7 m at a flight height of 300 m and a ground speed of 250 kph. ALS range data have been combined with precise GPS positioning and inertial navigation attitude information to determine the three-dimensional point cloud of the surface topography. The across-track swath width is roughly equal to the flight height, and the vertical accuracy is in the order of 10 cm depending primarily on uncertainties in the kinematic GPS-solutions. The point to point shot accuracy of the ALS is 1–2 cm (noise level of laser measurements) and the incidence angle of 0-1-40 degrees limits the return over smooth open water or newly formed smooth ice to angles close to nadir, i.e., no return from most of the swath in these cases. The survey altitude is limited by the range of the ALS, which is 600 m for the RIEGL LMS-Q240i model. Other solutions are available with ranges up to 2 km but might not fit into smaller aircrafts.

The **Riegl VQ-580I/II** ALS is used by AWI IceBird and is going to be used for CRISTALair. The maximum range of the Riegl VQ-580II depends on the laser Pulse Repetition Rate (PPR) and the reflective properties of the surface. At the lowest PRR of 150 kHz the maximum range is 1850 m (natural targets $\rho \geq 20$ %) and 2850 m (natural targets $\rho \geq 60$ %). For higher PPR the maximum range will decrease. The VQ-580II is a waveform-based swath laser scanner, scanning the surface in parallel lines. The wavelength of 1064 nm (NIR) is particularly well suitable for glacier and snow field mapping. The Field of View (FOV) is 75%, thus at a 1000 m altitude AGL the swath width is 1535 m. By using the lowest PPR to allow for the highest maximum range the point density is 0.6 per m^2 at 180 knots (93 m/s) and 1000 m altitude AGL. By reducing the speed and/or increasing the PPR the point density will increase.

The following methods have been applied to extract total freeboard from ALS 3D surface topography from ESA CryoVEx campaigns to further obtain freeboard heights, the full resolution data have been thinned in the along-track direction and averaged across-track to a resolution of approximately 5 m × 5 m. Since the laser measures the surface topography, it is crucial to estimate the sea surface height, from which the freeboard heights can be estimated. An MSS or geoid model is used as a first approximation of the sea surface height (SSH) and is subtracted from the ALS elevations to derive surface height anomalies. Due to SSH variability caused by time varying ocean tides and currents, errors in the ocean mean dynamic topography, and measurement errors, it is necessary to estimate the instantaneous sea surface height anomaly by identifying leads in the ice pack. The leads are selected automatically by identifying the minimum values of the orthometric height within equidistant subsections. Typical subsection length is 5 km, which is chosen based on local ice properties and geoid model variations and resolution. As we expect the sea surface to be a smooth surface, minimum points are accepted only if they are within 0.5 m of a linear fit to the minimum points. The instantaneous sea surface height is estimated by fitting a least-square collocation function to the accepted minimum points. Finally, freeboard heights are found by subtracting the estimated sea surface heights from the thinned and averaged ALS data (see also Hvidegaard & Forsberg, 2002 [RD42]). This method relies on the existence of leads in the ice pack. If the leads are covered by thin ice with or without snow, this will underestimate the sea-ice freeboard heights accordingly (e.g., Kwok & Cunningham, 2008 [RD64]). This, however, is included in the total sea-ice freeboard error estimate (see Hvidegaard & Forsberg, 2002 [RD42]). Manual examination of the data set supports the presence of leads at the 5 km length scale. Other methods by using vertical optical images to support manual selection of leads have been used in ESA CryoVal Sea Ice - conclusion. A study of using ASIRAS as classification for detecting leads have been attempted but is inconclusive.

5.2.1.2 Airborne radars

Ku-band radar ASIRAS: Within the frame of the CryoSat mission, ESA has developed an airborne proxy for the 'SIRAL' radar altimeter on CryoSat 2 operating in the ku-band. The Airborne Synthetic Aperture and Interferometric Radar Altimeter System (ASIRAS) has been integrated into an airborne platform and operates with simultaneous laser altimetry and optical imagery to provide detailed information on the interaction of the radar echo with land- and sea-ice surfaces.

ASIRAS was built by Radar Systemtechnik (RST) of Switzerland with the support of the Alfred Wegener Institute (AWI) and Optimare for implementation and operation on an aircraft.

The instrument can be flown at altitudes of 300m to 7km with a typical recording time of 5 hours. It is fully supported with onboard differential GPS and an inertial navigation system (INS) providing high-precision navigation and aircraft attitude (pitch and roll) data.

The ASIRAS instrument operates with a centre frequency of 13.5 GHz with a bandwidth of 100MHz to 1GHz. The pulse transmit/receive antenna half power beam widths are 10° along track and 2.5° across track, resulting in a beam limited footprint of 50 × 5 m² for flight altitudes of 1100 m above any surface. The instrument is designed with two modes of operation see Figure 5.4. High altitude mode (HAM) operates at altitudes above ~1000 m as phase coherent pulse-width limited radar with interferometric capability with optional manual or on-board (automatic) surface tracking. At lower altitudes a new mode was built into the system in 2005. The low altitude mode (LAM) operates as a FMCW at

operationally programmable ranges of altitudes between 0 and 1200m (tested between 300-1000m). LAM does not include interferometric capability, nor does it allow surface tracking. An updated LAM mode (LAM-A) with reduced data volume was verified in 2007. A side-effect of LAM-A is that the ASIRAS to surface range may not vary more than 20m and is therefore suited only to surfaces with minimal topography (open water and sea ice). For 2011, new software has been implemented (Cullen et al. (2010) [RD82]). Currently the ASIRAS radar is only operational in LAM and LAM-A mode, and is about to retire, but has been an important and reliable instrument and made baseline Cal/Val learnings for CryoSat-2 through the CryoVEx campaigns.
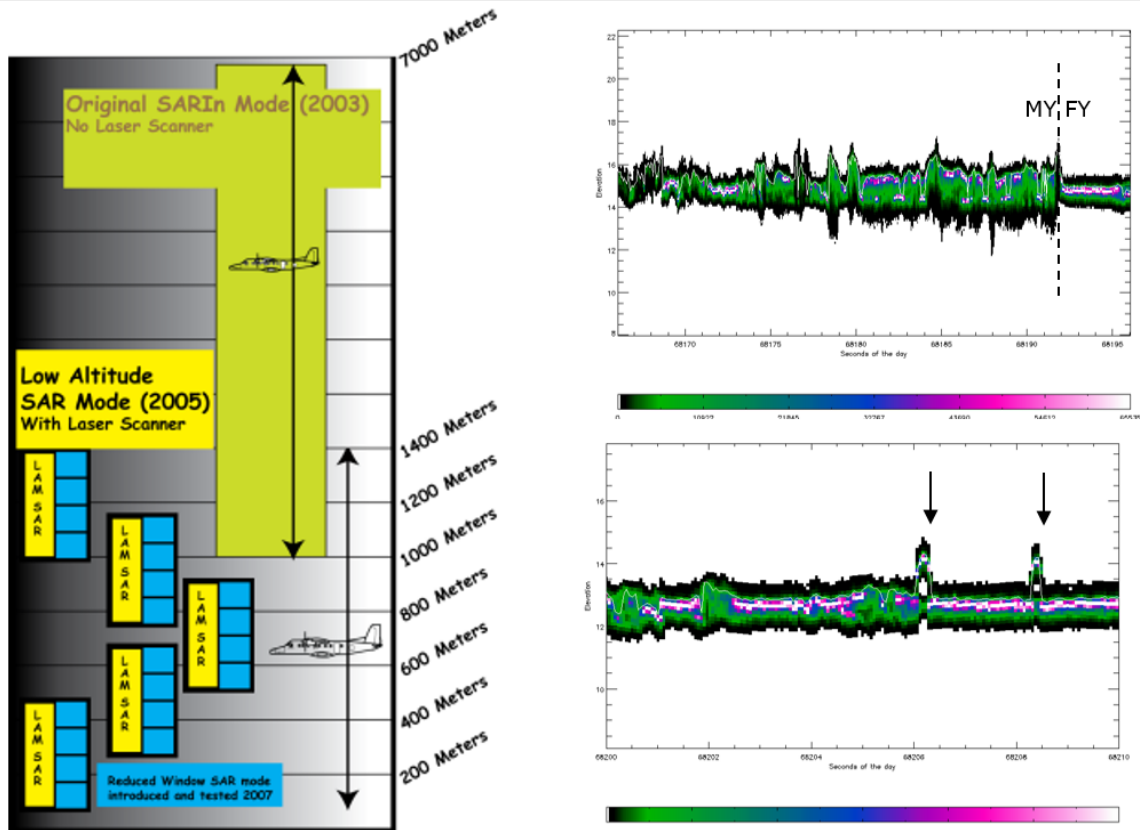

Figure 5.4: ASIRAS operation (left) ASIRAS operating modes; (top right) ASIRAS waveforms over multi-year (MY) and first year (FY) sea ice; (bottom right) ASIRAS waveforms over corner reflectors (arrows) on sea ice. From Cullen (2010) [RD82] and Cullen et al. (2007) [RD82]A.

Ka-band radar KAREN: The KAREN airborne instrument is an interferometric frequency modulated continuous wave (FMCW) SAR altimeter working at the Ka-band with central frequency of 34.525 GHz. The sensor operates with FMCW radar modulation in interferometric mode (SARIn), with one transmitting antenna and two receiving antennas. The instrument was developed by MetaSensing and was first tested over the Greenland Ice Sheet during ESA CryoVEx/KAREN 2016 fall campaign. Current version uses patch antennas, as opposed to the CryoVEx/KAREN 2016 fall campaign where horn antennas were used. Radiation characteristics of the new patch antennas include a gain of 22 dB and a 3dB aperture of 15° x 4.6° (along track and cross track). The processed multi-looked data corresponds to an along- and across-track footprint size of 5 m (100 looks) and 12 m, respectively. The vertical resolution is 0.1650 m.

The final version "levc" processing chain is similar to methods developed for CryoVEx/KAREN 2016 (Skourup et al., 2020) [RD98])and 2017 (Skourup et al., 2019 [RD99]), which introduces several steps going from the raw data format (level-0) to the final delivered data format (level 1B), including range compression (FFT and Hamming filtering), zero-Doppler filtering, ground-back projection (GBP), and multi-looking. For a more detailed description see the "KAREN altimeter - Processing chain and file format" documentation (MS-DTU-KAR-03-PFF-032). During the processing chain each KAREN data point is geo-located using input from best solutions of GNSS and INS data, and corrected for lever-arms between GPS antenna and KAREN reference points.

Multi-UWB S/C, Ku and Ka-band radar CReSIS: The use of multi-band radar systems for snow studies has been demonstrated extensively using ground-based equipment [13-17]. In contrast, the operation of multi-ultra-wideband airborne radars requires sub-millisecond sweeps, higher pulse repetition frequencies, and increased data rates. These features became realisable as technology advanced in recent years. Moreover, broadband data from these radars can be used "as is" to yield cm-scale vertical resolution; or can be spectrally segmented to emulate the operating parameters of spaceborne sensors (Rodrigues-Morales et al., 2021 [RD95]).

Currently, the operation of high-performance aerial radar systems for snow studies involves the following main scenarios: (1) separate large- and mid-size systems operating onboard platforms with moderate restrictions on payload size, weight and power (SWaP) [18-21]; (2) separate single-band compact instruments for operation on manned or unmanned vehicles [2], [22-27]; and/or (3) inherently multi-band systems with relatively narrow-band capabilities [28-29].

The CReSIS ultrawide FMCW radars include the snow radar (2-8 GHz), the Ku-band radar (12-18 GHz), and the more recent Snow/Ku Radar that covers the entire bandwidth of those first two systems. Combined, these are simply referred to as snow radars. In addition, a Ka-band (32-38 GHz) millimetre-wave front-end was also deployed during a single spring campaign in 2015. These different systems allow for large-scale measurements of snow thickness over sea ice at centimetre vertical resolution. The Snow and Ku-band radars were operated as separate systems until 2017 (MacGregor et al., 2021 [RD70]).

A compact, nadir-looking multi-UWB radar system was also developed with the remarkable capability of collecting data with up to ~18-GHz cumulative bandwidth, distributed in three separate bands: S/C (2–8 GHz), Ku (12–18 GHz), and Ka (32–38 GHz). The system's small form factor and relatively low power consumption, makes it easy to integrate and operate onboard mid-size aircraft, which are well suited for low-altitude surveys (<1,000 m above ground level, AGL) in cold regions. The sensitivity and vertical resolution of this system across its operating bands is comparable to that of the three separate instruments flown on larger aircraft as a part of NASA Operation IceBridge (OIB) between 2009 and 2016 [30]. Rodrigues-Morales et al. (2021) [RD95]

The Ka/Ku radar was flown as a single unit in CryoVEx/ICESat-2 2019 summer campaign with ~6 GHz of bandwidth, the system provides a theoretical vertical resolution of ~3 cm in snow, assuming a windowing factor of 1.44 and a dielectric constant of 1.53, which corresponds to a density of 0.3 g/cm3. This resolution is sufficient for the assessment of firn layers in ice sheets and thick snow cover on sea ice. However, wider bandwidths are required for measuring thin snow on sea ice, as shown in (Rodrígues-Morales et al. 2020 [RD94]).

Between 2009-2019, OIB repeatedly flew a snow radar during its campaigns, enabling the first contemporary basin-scale estimates of snow thickness on sea ice. Multiple algorithms were developed to infer snow thickness from OIB snow radar (Kwok et al., 2017 [RD60]), where each takes different approaches in determining the range to the air-snow and snow-ice interfaces. The algorithms included:

1. The original reference algorithm developed by the OIB PSO for the 2009-2013 campaigns (Kurtz et al., 2013 [RD55], 2015 [RD53]). It empirically accounted for inter-campaign differences in snow radar SNR, but did not account for the effect of sidelobes, and was therefore replaced in 2015 by a waveform-fitting-algorithm (Kwok et al, 2017 [RD60]).
2. A "quick-look" algorithm generated by the OIB PSO for the 2012-2019 Arctic spring campaigns (Kurtz et al., 2014 [RD54]).
3. A snow radar layer detection algorithm (Koenig et al., 2016 [RD49]).
4. A wavelet-based algorithm (Newman et al., 2014 [RD79]).
5. An algorithm developed by JPL (Kwok and Maksy, 2014 [RD61]).
6. The Support Vector Machine supervised learning algorithm (Holt et al., 2015 [RD39]).

Snow depths have been determined in both the Arctic and Antarctic, showing good agreement within situ observations if using an algorithm accounting for side- and main lobe effects of the impulse response of the snow radar. If not accounted for these side- and main lobe effects can result in a significant difference of >20 cm between OIB and in situ snow surveys (Kwok and Haas, 2015 [RD65]). In the western Arctic, a decrease in overall snow thickness is observed between all snow thickness derivation methods - potentially due to the later sea ice formation in the autumn and the shift from multi-year ice to first-year ice (Webster et al., 2014 [RD115]). Furthermore, a thinning of the snow on first-year ice compared to that on multi-year ice is also observed (Kurtz and Farrell, 2011 [RD56]), when compared to the 1950-1980s climatology of Warren et al. (1999) [RD114]. Snow thickness in the Antarctic is however more challenging,

due to unique conditions including extensive ice deformation, seawater flooding, snow-ice formation, and meltwater freezing, which complicates the retrieval of the air-snow and ice-snow-interfaces, which results in larger uncertainties (Kwok and Maksym, 2014 [RD61]). Nonetheless, it must be mentioned that differences in the various OIB-related snow thickness products persist, especially given the progressive improvements to the snow radar itself over the mission lifetime.

More recently, since 2019 AWI IceBird campaigns have added a snow radar to its instrument package and developed a new algorithm "Peakiness" relevant for low-altitude flights carrying the fully-polarimetric S/C/Ku-band sensor [RD]. The ESA Cryo2IceEx/NERC DEFIANT Antarctic Campaign in December 2022 also carried along a CReSIS snow radar (C/S-band).

CRISTALair: With the upcoming Copernicus Expansion Ka/Ku dual-frequency polar satellite altimetry mission, CRISTAL, expected to launch in 2027/2028, an airborne demonstrator is currently being developed for the validation of the satellite observations. CRISTALair will succeed ASIRAS (originally developed to simulate CryoSat-2, see first paragraph in this Section), with the ability to acquire data simultaneously in Ku- and Ka-band. The radar shall acquire at 1-4 km ground altitude and have interferometry in both Ka- and Ku-band, with a pulse-repetition-frequency of more than 10 kHz and automatic tracking (range and gain) system. The swath is expected at >200 m. Requirements set forward include elevation uncertainty of less than 10 cm, range noise less than 0.8 c, and altitude accuracy of less than 5 cm. Furthermore, the CRISTALair campaigns will integrate an airborne laser scanner, a color-infrared camera, and ancillary equipment for ensuring precise positioning and attitude of the interferometer. Platform requirements for CRISTALair include acquisition of data up to 7000 meters above sea level with a 6-hour flight duration, and certification to fly on either the Basler BT-67 or DHC-6 Twin Otter aircrafts currently. Test flight campaigns are expected in spring/summer 2025.

5.2.1.3   Synergestic airborne passive microwave radiometers

CIMRair: Similarly to CRISTALair, the future Copercnius Expansion CIMR mission is currently also being build an airborne simulator named CIMRair. Currently, there are no public documents available describing the instrument set-up expected on CIMRair, but considering the synergies between CRISTAL and CIMR, we assume similar synergies between CRISTALair and CIMRair. Here, this includes snow depth retrieval, thin ice retrieval, and surface classification.

For considering synergies, there is an expected Arctic Copernicus Synergy Campaign planned for collocated measurements of CRISTALair, CIMRair along with snow radar, radiometer (airborne) and ground measurements, which is aimed at acquiring a unique dataset supporting the cryosphere scientific community research and shall help improve current models and estimates.

5.2.1.4   Synergestic airborne synthetic aperture radars (SAR)

CryoSAR: While the future Copernicus Expansion polar L-band SAR mission, named ROSE-L, does not have a dedicated airborne demonstrator being developed, other airborne systems simulating the observations are available. In particular, the University of Waterloo (Canada) deploys their CryoSAR system carrying an airborne synthetic aperture radar (SAR) operating at polarimetric, interferometric (repeat pass and single pass for L- and Ku-band, respectively) L-band (1.3 GHz) and Ku-band (13.5 GHz) funded through NERSC, CFI, and CSA. Here, potential scientific applications include sea ice concentration, thin thickness, and snow depth on sea ice. The SAR is manufactured by MetaSensing and can be deployed on a Cessna 208B Caravan and a DC-3 Basler (STC pending). Waveform modulation at L-band is pulsed, whereas at Ku-band is a FMWC, and the bandwidth is 200 MHz and 600 MHz, respectively, both with a maximum azimuth resolution of 25 cm. The system can be operated in –20 to +60 degrees C.

5.2.1.5   EM sea ice thickness sounding

Electromagnetic induction sea ice thickness sounding takes advantage of the fact that sea ice has a very low electrical conductivity, whereas sea water is a good conductor (high electrical conductivity). Typical conductivities of sea ice are 0 to 50 mS/m (Haas et al., 1997 [RD31]) and 2400 to 2700 for mS/m for sea water. Due to the electrical conductivity of sea ice, the primary EM field generated by a transmitting coil of the EM system will penetrate the sea ice almost unaffected, while it will generate eddy currents in the sea water below the sea ice. These eddy currents induce a secondary EM field which propagates upwards through the sea ice, and the strength of the secondary EM field is measured at the receiving coil of the EM system. The strength of the secondary EM field is directly related to the distance

h_w between the coils and the conductive sea water surface, which coincides with the ice underside. To obtain the height from the ice surface to the EM system, h_i, one would normally use a laser altimeter to extract the height. Thereafter, the ice thickness (Z_i) is a result of the difference between the electromagnetically determined height above the water surface (h_w) and the height above the ice surface (h_i) measured with the laser (Haas et al., 2006 [RD32], 2009 [RD33]; Pfaffling et al., 2007 [RD84]), $Z_i = h_w - h_i$, where the Z_i is the total ice thickness (that is, the sum of snow plus ice thickness).

Figure 5.5: Principle of EM thickness sounding using the EM Bird, there ice thickness z_i is obtained from the difference of the bird's height above water and the ice surface (h_w and h_i, respectively). h_w is obtained with the assumption of a negligible ice conductivity σ_i, known water conductivity σ_w and horizontal layering (Haas et al., 2009 [RD33]).

More recently the EM sensor has been installed and flown on fixed winged aircrafts, i.e. AWI DC-3 (Polar-5/6), which makes it easier to make coincident flights, i.e during CryoVEx campaigns, as the Twin Otter and DC-3 can fly with similar survey speeds (~100 knots) and with different altitudes 300m for TO and 50m for DC-3. Coordination is crucial as the EM sensor during in-flight calibration needs the aircraft to climb to higher altitudes (~3,000ft) and descend afterwards. The helicopter is more optimal for regional surveys and can be brought along on icebreaker cruises.

The nominal ice thickness uncertainty for a single HEM measurement is 0.1 m over level ice, with significantly larger errors and an underestimation of maximum thickness occurring in heavily ridged areas due to footprint smoothing (Haas et al., 2009 [RD33]; Mahoney et al., 2015 [RD71]). Typical HEM footprint size is on the order of 40–50 m.

As the integrated system EM+laser results in total thickness (snow + ice), the most optimal configuration is to add a snow radar. This setup has been used in AWI IceBird campaigns since 2019.

5.2.1.6 Colour/IR Cameras

In the ESA CryoVEx/Cryo2IceEx several different types of digital cameras have been used, more recent GoPro cameras, for nadir looking images. These cameras are relatively small and have fitted into the limited space, due to a tight installation fitting both radar and laser scanner, in the relatively small hatch in the Twin Otter aircraft used. These images have typically been geolocated by assigning a position and time at the approximate center of each image. Onboard the British Antarctic Survey (BAS) Twin Otter the instrument bay allows installation of a larger DSLR camera of type Canon EOS 7D with high pixel resolution (5184×3456). By mounting the camera with the larger Field of View (FOV) parallel to the flight direction allows for overlapping images depending on the aircraft cruise speed. The NASA Operation IceBridge (OIB) Digital Mapping System (DMS) consists of DSLR cameras (Canon 5D Mark II/III) and the CAMBOT system (Canon Rebel XTi, AVT Procilica GT 4905C) (MacGregor et al., 2021 [RD70]) where the images can directly be used for surface classification in the ATM sea ice freeboard algorithm (Section 5.2.1.1). The typical FOV of the DMS cameras are 46° in the across-track direction and 65° in the along-track direction corresponding to a swath width of 849 m and swath length of 1274 m. These kinds of cameras also have the sufficient dynamic range for observations over sea ice. This corresponds to an along-track overlap of 60% and a nadir pixel resolution of 10 cm at nominal OIB survey AGL (460 m) and ground speed (280 knots or 144 m/s), which will correspond to a pixel resolution of at least 1 m at 1000 m altitude AGL.

For a digital camera to fulfil the requirements as an FRM it shall be possible to generate georeferenced images e.g. geotiff format or similar, where each pixel is assigned a geographic position and time. Such image processing requires referencing each frame to the navigation system (GNSS and INS), Location and pointing knowledge, characterization of

lens distortion, and derivation of mounting angles. Often the internal clocks of cameras are not precise enough, and time-tagging by either GNSS or other methods are needed (MacGregor et al. 2021).

5.2.2 Permanent/semi-permanent instruments, platforms and sensors

Various in situ data of relevance for altimetry-derived sea ice thickness exist and will be described in further detail below. It is crucial to understand, that while the direct observations may not be applicable in a validation, it is the derived observations that are often used to validate by - which, however, also means that assumptions and simplifications may apply, all of which should be considered when comparing with the derived satellite observations.

5.2.2.1 Upward Looking Sonar (ULS)

Moorings can provide a time series of temperature, salinity, currents, sea ice draft, and bottom pressure (sea surface heights). Upward Looking Sonar (ULS) instruments (sometimes called ice profiling sonar, or IPS) measure sea ice draft by transmitting pulses of sound toward the surface and measuring the time elapsed until the echo of a pulse is received back at the instrument. Time is converted to distance using assumptions about the profile of sound speed in the water between the instrument and the surface. As the location of the open water surface is apparent in the echo record, and the depth of the instrument is known, then the depth (or draft) of the under-ice surface can be calculated (Witte and Fahrbarch, 2005 [RD119]).
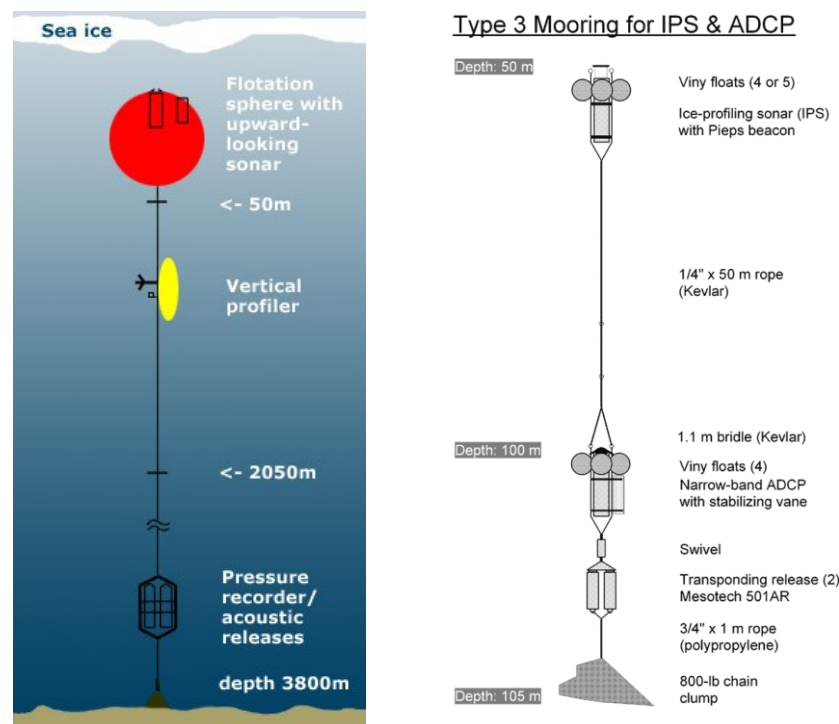

Figure 5.6: Mooring design. (a) BGEP, and (b) IOS.

A variety of programmes have deployed moorings and they are amongst the primary in situ observations used to validate satellite-derived sea ice thickness by (e.g., Sallila et al., 2019 [RD97]; Quartly et al., 2019 [RD90]). Programmes such as BGEP, NPEO, NPI, ADPC, and IOS are only some of the programmes which have deployed (and some still deploying) ULS'. Institutes such as AWI are also deploying their own ULS observations, and as such, many observations from ULS are available over a relatively long period and from different locations. However, while the principle behind ULS is the same for the different profilers used in the various programmes, the actual setup of the moorings and the used profilers are different. Furthermore, the processing methods used to achieve the derived sea ice drafts may also differ, resulting in potential discrepancies among the sea ice draft observations. Figure 5.6 shows a range of different mooring setups.

One specific example of a ULS setup (BGEP): A McLane Moored Profiler (MMP, coloured yellow in mooring diagram) is used to sample currents and hydrographic data from 50 to 2050 m with a 17-hour time interval. In addition, an upward-looking sonar (ULS) provides information about sea ice draft, and a bottom pressure recorder (BPR) measures sea level height variability and near bottom temperature and salinity. Each mooring consists of a surface flotation package at 50 m depth housing an ULS, a mooring cable containing the MMP, dual acoustic releases and tether to BPR attached to the anchor. [RD141]

5.2.2.2 Ice Mass Balance (IMB) buoys

An IMB is a buoy that can measure the mass balance of the sea ice at a particular location, including measuring any ablation or accumulation of snow and any growth or melt of ice - this information makes up the mass balance of the ice. Currently there are various IMBs in use and deployed at different areas, however since they are deployed on sea ice floes, they drift along with the sea ice. Thus, the lifetime of an IMB depends on the condition of the floe, the surrounding sea ice and weather conditions, and the condition of the IMB itself.

5.2.2.3 Traditional IMBs

The very first all-year-round IMBs were deployed by CRRELL and use a thermistor chain to measure the temperature profile through the ice, typically at 5-10 cm intervals. Furthermore, two acoustic sensors (one above-ice, the so-called snow acoustic sounder, and one under-ice, the so-called underwater acoustic sounder), which are used to monitor the mass balance, i.e. the snow accumulation/ablation and ice growth/melt (Richter-Menge et al., 2006 [RD92]). The data is transmitted through the Argos satellite system, or more recently the Iridium system.

For CRREL, the instrumentation of the autonomous mass balance buoys typically consists of a data controller module and Argos transmitter (Figure 5.7), a temperature string, above ice and below ice acoustic sounders measuring the positions of the snow/ice surface and ice bottom within 5 mm. In addition to the mass balance instrumentation the buoys have a barometer, and an air temperature sensor (Jakobsen et al., 2013; Polashenski et al.; 2011 [RD87]; Richter-Menge et al., 2006 [RD92]; [RD127]).
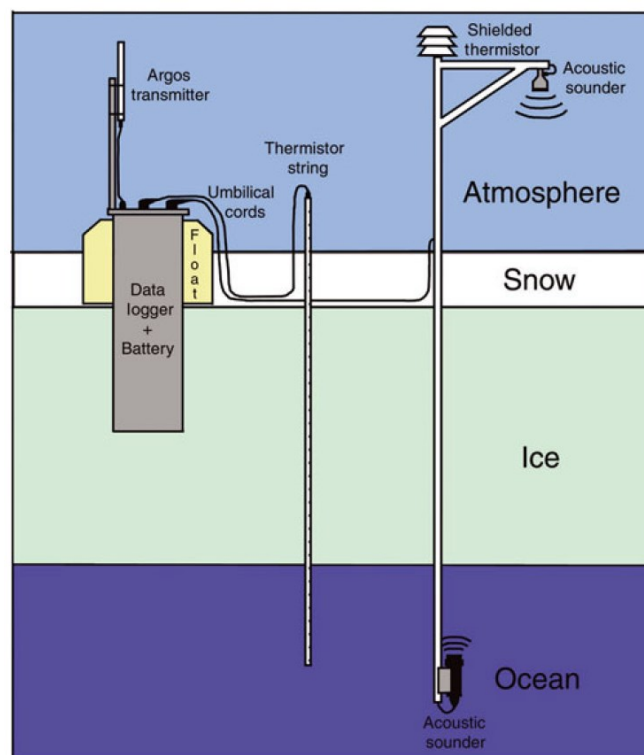

Figure 5.7: Traditional IMB schematic diagram from Polashenski et al. (2011) [RD87]

5.2.2.4   Seasonal IMBs (SIMBs)

A seasonal IMB buoy, designed to survive the summer melt, has also been developed to consider the current change of the ice cover from perennial to seasonal ice cover. Since this change poses new challenges and needs to the instrumentation, and since the traditional IMBs were developed for deployment on multi-year ice/thicker ice, there was a need to adapt the IMBs to the changing ice cover. The hazards expected to occur or be present in a perennial ice cover is expected to be amplified in a seasonal ice cover. One example is the multi-component design setup of the traditional IMBs, all connected by umbilical cords, as it exposes the system to greater risk of being rendered apart by ice dynamics or wildlife. Thus, placing all instruments in a single housing presents an advantage against risks related to ice dynamics and wildlife, but also presents a challenge of ensuring that the housing does not significantly affect ice conditions near it. Reducing the size of the buoy hull and altering the material make-up could alleviate this concern (Figure 5.8). Furthermore, the SIMB must be capable of keeping itself upright without ice support and in addition, water-proofing and ensuring the possibility of floating in a known orientation is necessary as well, to ensure that the end-of-melt season conditions in the seasonal ice zone, which is bound to expose the IMB to open water, is not an issue for the setup (Polashenski et al., 2011 [RD87]).
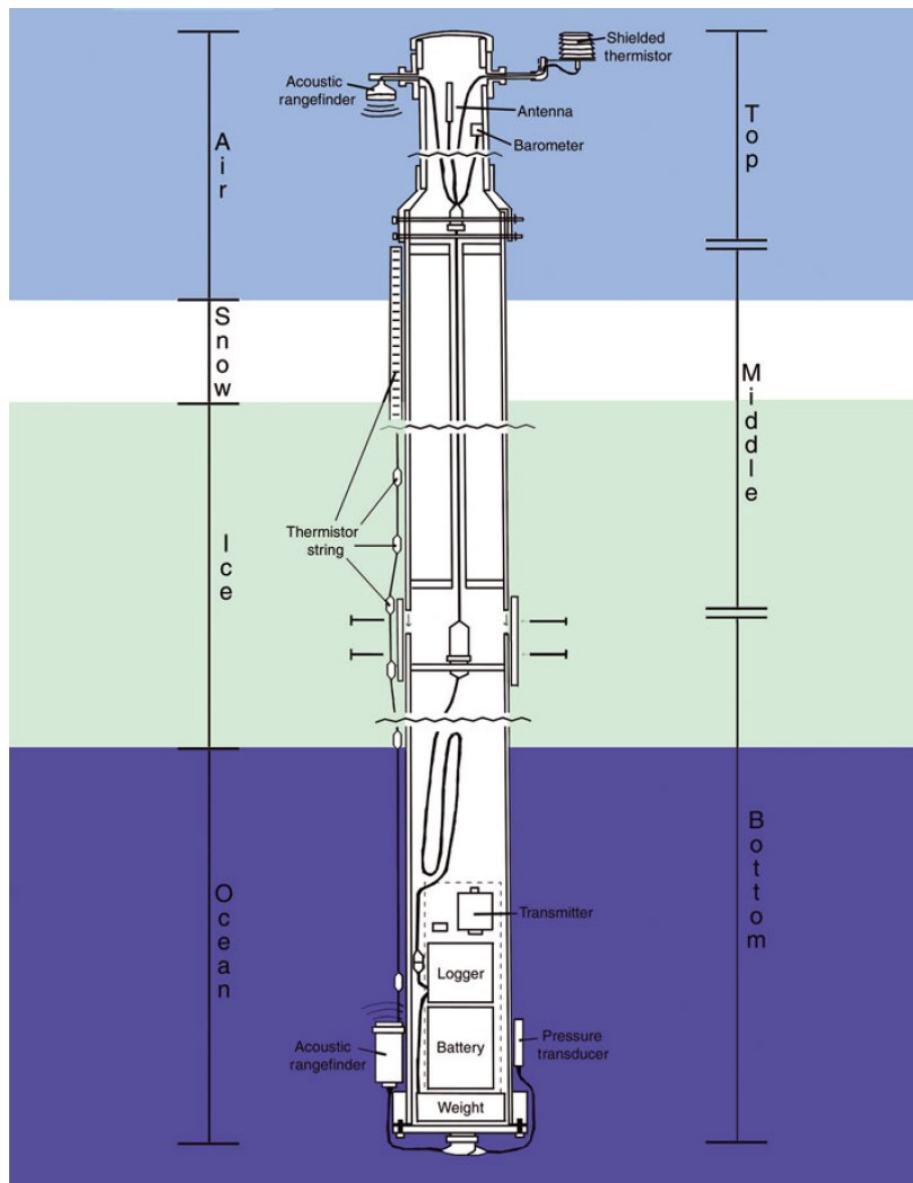

Figure 5.8: Seasonal IMB schematic diagram from Polashenski et al. (2011) [RD87]

The updated setup of the traditional IMBs to a seasonal ice cover is made of a single 15 cm diameter spar-buoy type hull that contains, protects and positions the sensors with minimal external wires. The hull is made entirely of PVC components (reducing cost and matching thermal properties of the ice). The design is modular and ships in three sections, easy to transport and prepare on site. The total height of the SIMB buoy is 5.5 m, with the top 2 m above the ice surface. The instrument package is like that of traditional IMBs: sonic rangefinders above and below ice surface, a thermistor string for measuring profiles of temperatures through the atmosphere-ice-ocean boundary. Coordinates of the buoy are calculated from Doppler shifts in the satellite transmissions to within a few kilometres (however, there is a potential for adding a GPS). New for the SIMB is an underwater pressure sensor, that provides information on changes in the mass balance of the entire floe, and allows for the buoy to be monitored for slippage in relation to the ice during thin ice conditions. Additional meteorological data such as air-temperature and barometric pressure observations are also taken, and provided on an hourly basis, while ice temperatures and mass-balance data are collected and sent only every 4 hours. The position of the buoy is calculated from each transmission set received (Polashenski et al., 2011 [RD87]).

5.2.2.5 SIMBA buoys

While traditional IMBs have been using acoustic sounders (over-water for snow and under-water for ice) to measure the snow and ice thickness, a more recent type of IMB buoys, called the SIMBA (Snow and Ice Mass Balance Array) buoy, makes use entirely of a string of thermistors. SIMBA buoys measure vertical temperature profiles through the air-snow-ice-water column using a thermistor string, and then determine the ice and snow thickness from the temperature profile. While the determination of the snow and ice thickness is currently a manual process, an automated algorithm has been developed to perform this task to aid the processing (Liao et al., 2018 [RD68]).
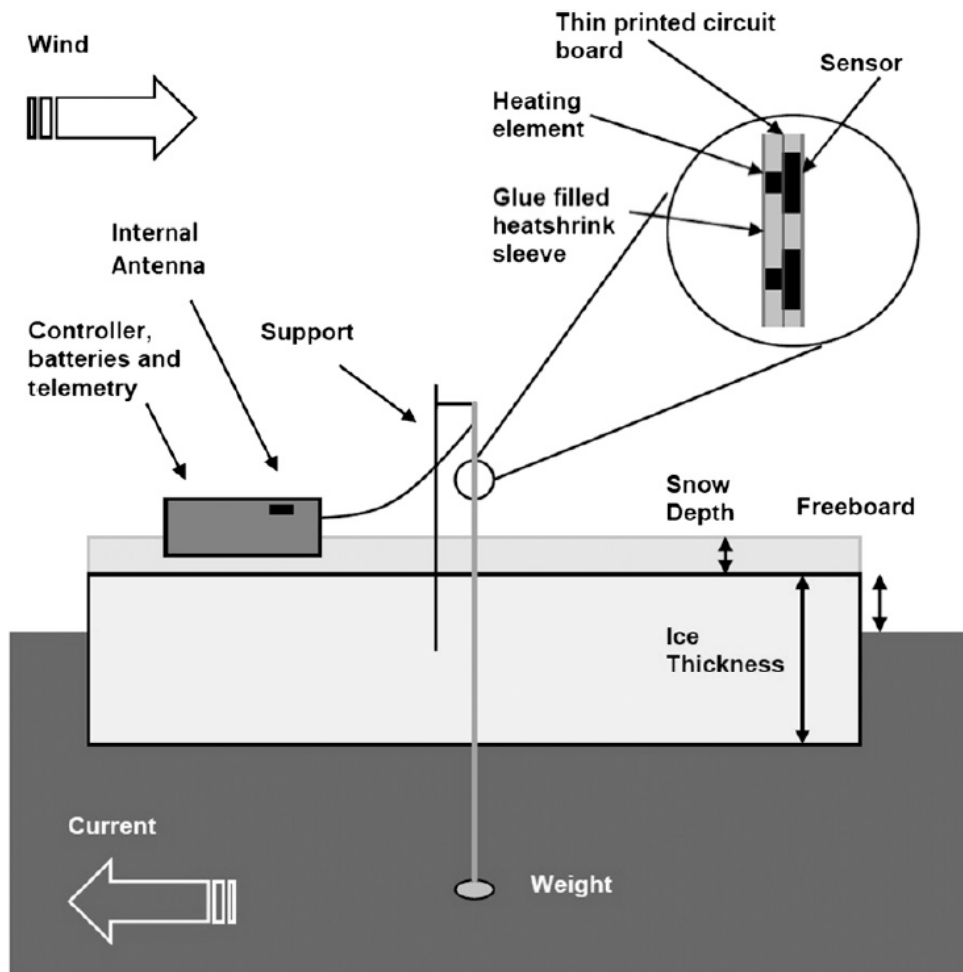

Figure 5.9: Schematic design of the SIMBA IMB setup, from Jackson et al. (2013) [RD45]

The SIMBA buoys were developed by the Scottish Association for Marine Sciences (SAMS) Research Services Ltd (SRSL) based at the Scottish Marine Institute, UK. It is equipped with a 5-m-long thermistor string with sensors spaced every 2 cm (Jackson et al., 2013 [RD45]), a built in-GPS, a magnetometer for tilt and floe rotation, a barometer for surface air pressure, and an external sensor to measure near-surface ambient air temperature, and a weak voltage supply is connected to create gentle heating of each sensor and its surroundings. The heating interval usually lasts between one and two minutes, and the heating occurs once a day, and the Iridium satellite is used for data transmission. In comparison with the traditional CRREL IMB buoys, the SIMBA buoys are considered low cost. The change in temperature recorded by the thermistor string during the day is used to identify air/snow, air/ice and ice/water interfaces. However, the retrieval of the snow and ice thickness is not trivial since many factors can impact the temperature observations. The sensors exposed in the air could be affected by wind vibration, snow drift, frost condensation, and solar heating, which could result in erroneous temperature readings (Liao et al., 2018 [RD68]).

Ref	NOV-FE-1464-NT-043		
Issue	1	Date	26/11/24
Rev	0	Date	26/11/24
Page	53/ 120		

ST3TART-FOLLOW-ON: FIDUCIAL REFERENCE MEASUREMENTS (FRM) - S3 LAND ALTIMETRY
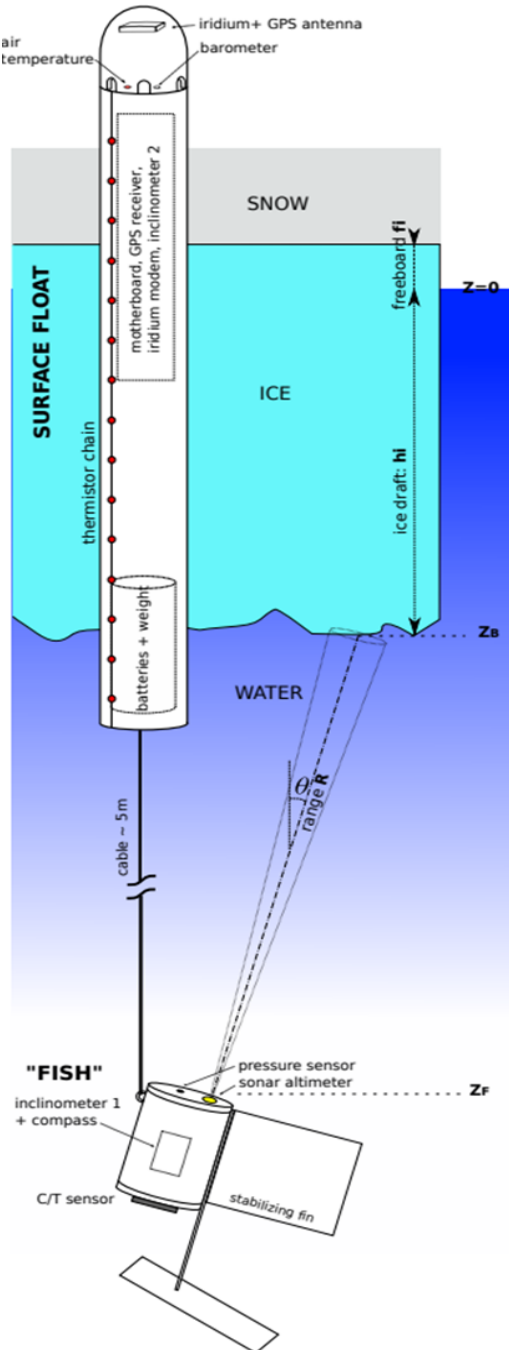
5.2.2.6 Ice-T buoys

Figure 5.10: Schematic of an Ice-T buoy

A different type of mass balance buoy is called the Ice-T (Ice-Thickness) buoy, which records parameters relevant to the local sea mass balance as well. The Ice-T buoy includes a 2 m long floating surface buoy trapped in ice, with an instrumented subsurface module hanging approximately 5-6 m below the ice base, called the 'fish'. The surface buoys host a vertical chain of 32 thermistors that captures the thermal field of the snow/ice/water layers, while also measuring air temperature, atmospheric pressure, GPS position, and the tilt of the instrument. Data is transmitted every 15 minutes through the Iridium communication system, and the buoy is autonomous for one year. Since 2016, an inertial motion unit (IMU) has been operational on the Ice-T buoy. The subsurface module also includes an upward looking sonar, a two-axis inclinometer with a magnetic compass, and a pressure sensor, which are combined to provide a measurement of ice draft. Finally, the subsurface module also includes a conductivity-temperature sensor, recording the temperature and salinity nominally at 6 m below the ice/ocean interface (Vivier et al., 2016 [RD109]).

5.2.2.7 Various other buoys

The ZENO Ice buoys [RD128] yield data on air, snow and ice temperatures, but not directly on mass balance as the other buoys provide based on acoustic sounders or thermistor strings. However, in the study of Zhongxiang et al. (2017) [RD126], where they compared SIMBA buoys with Zeno buoys deployed during the CHINARE route in 2014 and 2003, respectively, they presented a method of analytically deriving snow depth from the temperatures measured by the ZENO buoys.

5.2.3 Long-term monitoring community-based programme sites

Other types of semi-permanent observations are available, but less exploited by the sea ice altimetry community. An example of such sea ice observation networks, based on a community effort, is the Siku-Inui-Hila project (funded by the NSF), that took place during 2006-2010. The aim of the Siku-Inuit-Hila project was to examine sea ice, sea ice use, and sea ice change in the Arctic communities of Qaanaaq, Greenland, Barrow, Alaska, and Clyde River (Huntington et al., 2010 [RD40]), Nuanavut. It presented a possibility of acquiring observations of sea ice throughout the season (compared to campaigns) while still requiring personnel to go out and observe the data (much like one would do in a campaign). They acquired the help of locals to make these observations, as the observations would benefit both the local community, while also providing reference observations. Beside campaign-related activities such as drillings (observations taken when the opportunity allows itself at various locations), semi-permanent observation sites were also deployed during this programme. In the Handbook by Mahnoey and Gearheard (2008) [RD71], they described the instruments, deployment procedures and protocols that locals should perform to acquire the observations by drilling and observation sites. Drillings will be detailed in a later section, but here three types of measurements to be acquired at the observation sites will be described in more detail based on Mahoney and Gearheard (2008) [RD71]. The following three types of instruments can be deployed close to each other and thus consist of a longer-term monitoring site, where locals can go to and observe the change of the sea ice.

Here we can also mention **CanCoast**, which is a collection of datasets that describe the physical characteristics of Canada's marine coasts including weekly sea ice thickness and snow depth measurements in the Canadian Arctic with some stations measured as far back as the 1950'ies to present. The data was collected by Environment Canada's Meteorological Service, St. Lawrence Seaway Authority, Trent University, and Queen's University. The dataset is publicly available and has been used for satellite altimetry validation purposes but is challenged by being obtained close to the coast on landfast ice, where sea ice thickness is difficult to measure by satellites.

5.2.3.1 Hotwire thickness gauges

A hotwire thickness gauge can observe sea ice thickness. As described by Mahoney and Gearheard (2008) [RD71], a hotwire gauge consists of a thickness stake and a cable, where the thickness cable has a metric measurement tape on it. The cable has a wooden handle at one end and a metal bar at the other end, and to install this gauge, two holes must be drilled, approximately 2.5 cm apart. The stake must be placed in one hole, ensuring that the screw at the 0 m mark rests at the ice surface, below the snow. Then snow must be used to pack the hole above the water like to hold the stake vertically while it freezes into its position. Next, hold the wood handle on the end of the hotwire cable and drop the metal bar through the other hole. The wooden handle should be hung up out of the snow on the second screw of the thickness stake (see Figure 5.11 (a)).
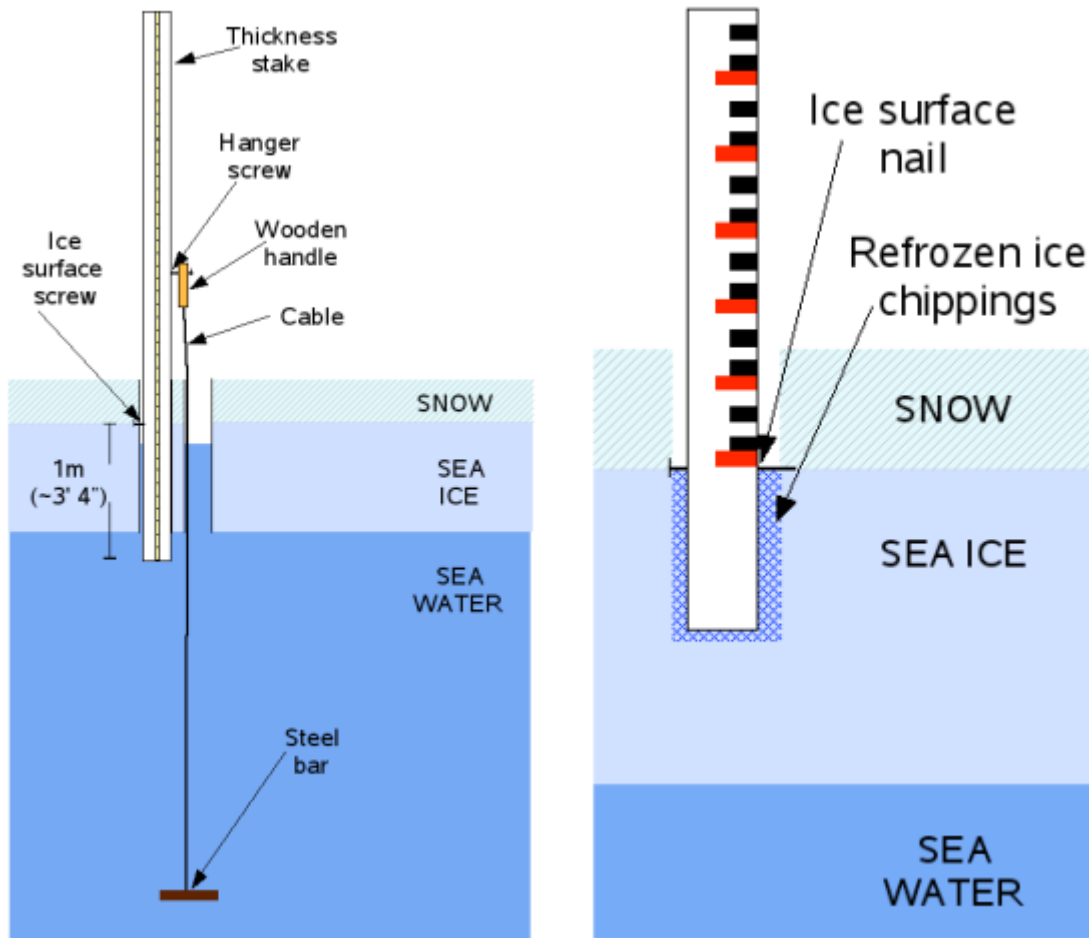
Figure 5.11: (a) A hotwire gauge (stake and cable) placed in two holes through the ice, and (b) a snow take in the ice placed in a shallow hole in the ice (Mahoney and Gearheard, 2008 [RD71]).

A grounding wire is required and needs to be connected with the thickness gauge. It requires a 3 m length of copper wire and a stake, without marking, and must be placed in a hole drilled completely through the ice and the copper wire must be lowered through the ice, learning about 1 m above the ice. The stake should be placed in the hole, and the wire should be wrapped around the stake a couple of times. This setup is not a hotwire thickness gauge (Mahoney and Gearheard, 2008 [RD71]).

To observe sea ice thickness from the hotwire thickness gauge, the hotwire cables must be melted free of the ice by running electric current through them using a generator. Having the steel/metal bar of the thickness gauge melted free, it is now possible to hold the handle tight up against the underside of the ice, and against the measurement tape on the thickness stake and read the distance at the top of the handle as the thickness of the ice. Once the observation has been noted, the metal bar must be hung on the screw of the stake again to prevent the bar from freezing into the underside of the ice (Mahoney and Gearheard, 2008 [RD71]).

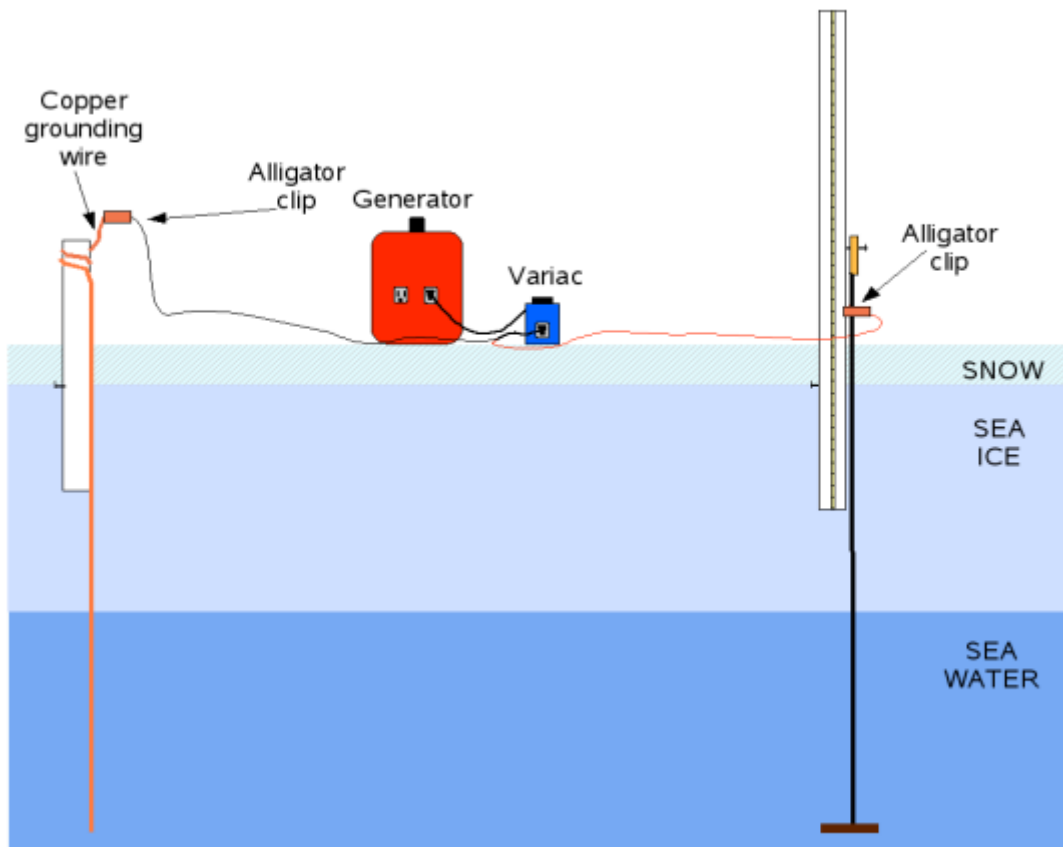**Figure 5.12: Connecting a hotwire cable and the copper grounding wire to the generator, through the Variac. The seawater beneath the ice completes the circuit and the current heats the cable so that it melts free (Mahoney and Gearheard, 2008 [RD71]).**

5.2.3.2   Snow stakes

A snow stake provides information about the snow depth and requires only one hole of at least 15 cm depth. To disturb the snow as little as possible, one should not drill through the sea ice. Once the hole is drilled, the stake should simply be placed inside the hole so that the nail rests on the ice surface (see Figure 5.11 (b)). The stake must be vertical and facing such that the thinner edge is toward the prevailing wind and that all stakes are facing the same direction - this will make them easier to read and cause less snow to drift in behind each stake. Once the stake is properly deployed, the hole must be packed with ice shippings and a little water from a bottle should be added to make it freeze quicker (Mahoney and Gearheard, 2008 [RD71]).

When acquiring the snow depth from snow stakes, one must make sure not to disturb the snow within the measurement area. The length of each stake sticking out of the snow must be recorded (black and red lines can be counted which aids the reading of the stakes). Since the nail is placed so that it rests as the ice surface, measurements on the snow stake are only made from the placement of the nail and upwards. Thus, one can calculate the snow depth by subtracting the visible height from the total height of the snow stake (Mahoney and Gearheard, 2008 [RD71]):

5.2.4   Shipborne

While ships may carry shipborne radars, various instruments to be deployed on the ice or potentially scanners attached to the side of the ship for tracking the surface, the most common and widely used method for detecting observations of relevance to Sentinel-3 LAND Sea Ice observations are the visually estimated sea ice thicknesses. Various methods are applied by the personnel and the observers onboard the ship. Here, we detail two commonly used methods:

As described by Worby and Allison (1999) [RD121], ice thickness (for Antarctic sea ice, used in the ASPeCT programme) are estimated for the three dominant ice types (primary, secondary and tertiary). To help the observer that is located at the bridge of the ship, an inflatable buoy of a known diameter can be suspended over the side of the ship,

approximately 1 m above the ice, to provide a scaled reference against which floe thickness can be estimated. Only the thickness of level floes or the level ice between ridges is estimated. The thickness is observed visually from the floes that turn sideways along the ship's hull by a trained observer (Worby et al., 2008 [RD120]; Worby and Allison, 1999 [RD121]). It is mentioned that very thick floes may be estimated by their freeboard, and that the accuracy of careful observations will be within 10-20% of the actual thickness - thus, a large sample of observations could provide a good statistical description of the sea ice pack. Dedicated voyages could also include regular in situ observations of ice and snow thickness, both on level ice and across ridges (Worby and Allison, 1999 [RD121]).

For the ASSIST programme, a slightly different approach is used or at least described in more detail with additional requirements. Here, the observers are trained to estimate the thickness of blocks that are fully overturned (though much like the ASPeCT programme), and by observing a series of overturning blocks during an observation period, the thickness of level ice for each ice type can be estimated. The precision here is expected to be 20 cm for an experienced observer. Only estimates of level ice are considered valid (ridged ice may not overturn fully and thin ice may not overturn at all, thus only level ice is relevant). The thickness estimate should be the most common thickness of level ice observed for each ice type over a 10 min observation period. They also note that it can be helpful to have an object near the water line of known dimension to train the eye after (for estimating both freeboard, thickness, and snow thickness). Either by tying a fishing buoy of a known diameter on a line over the side of the ship, or by placing a pole with 10 cm painted blocks on it to a lower rating of the ship see Figure 5.12). They note that a standard procedure for an ice watch is to make an observation every hour, on the hour, when the ship is in motion and that observations should not be recorded when the ship has not moved. In their manual, they state that: the ice should be viewed within 1 nautical mile from the ship during a 10-minute observation period that is normally performed on the ship's bridge (Hutchings et al., 2020 [RD41]).

Figure 5.13: Painted pole used to aid eye in estimating ice thickness (credit: Lauren Farmer and Alex Cowen, used in Hutchings et al., 2020 [RD41]).

Additional other parameters are often observed from the ships such as floe size, ice type, concentration, snow thickness, snow type etc. According to Hutchings et al. (2020) [RD41], snow depth is observed in the same way as ice thickness, though the mean depth is estimated. In Worby and Allison (1999) [RD121], the snow thickness is also described to be relatively straightforward to determine from floes turned sideways along the ship's hull. However, they do note that at times the ice-snow interface can be difficult to distinguish, especially if the snow has been flooded and snow-ice has formed.

5.2.5 Ground-based campaign data

Beyond airborne, shipborne and helicopter borne campaign data, many of the sea ice campaigns also include measurements acquired on ground by the ground team. These observations make up the various in situ (and 'ground-

truth') observations which are identified as the most accurate observations to validate by. However, they are sparse due to the nature of campaigns, restrictions of remote areas and harsh conditions/environment. The ground team often carry various instruments along for measuring specific geophysical variables; this includes both light-weight and heavy-weight equipment depending on the campaign and what is aimed to measure. Some measurement techniques and instruments have already been mentioned e.g., GEM and GPR. We will discuss in more detail some additional observations acquired as 'traditional' in situ observations: meterstick observations, magnaprobe observations, drillings and thickness gauge observations.

5.2.5.1 Magnaprobe

A magnaprobe provides automatic snow depth observations. It consists of a ski pole-lid rod housing a magnetostrictive device along which a basket and a magnet assembly slide. The rod is inserted into the base of the snow, the basket floats on top of the snow and when a button is pushed, the distance between the rod tip and the basket is measured while a position is acquired. They are accurate to more than 5 cm depending on the underlying surface (Sturm and Holmgren, 2018 [RD104]).

One magnaprobe available that has been used in various studies (e.g., Haas et al., 2017 [RD35]) is the Snow-Hydro Magnaprobe [RD129]. This snow-depth-probe is similar to an automatic snow depth probe, but also records GPS position. With this probe, an operator can walk across a snow-covered landscape and in several hours produce a detailed transect of snow depths. Of the magnaprobe observations used in Haas et al. (2017) [RD35] which used observations from the CryoVex 2017 campaign, measurements were performed with a constant spacing of two to four steps, corresponding to a distance of 1-3 m, depending on the operator, along the same profiles as the GEM thickness observations used as well.

Figure 5.14: An example of a magnaprobe in use (Sturm and Holmgren, 2018 [RD104]).

5.2.5.2 Drilling
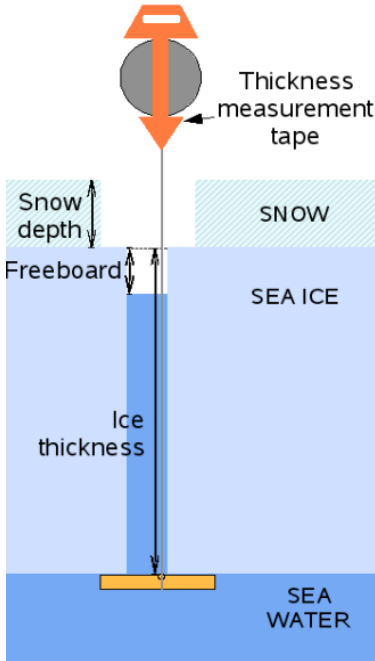
One method of measuring sea ice thickness and ice freeboard is by drilling directly in the ice. To do that, one could use a Kovacs Auger. which is a tool used for drilling through ice. The cutting edge is sharp and care should be taken to not damage it or other objects during transport. The auger comes with additional flights which can be attached to the auger to drill through thick ice, where each flight is 1 m long. To power the auger, one can use either a hand (by using the brace attachment) or an electric drill, however the electric drill needs to be powered by a generator. Once a hole has been drilled, one can measure the snow depth, ice thickness, and freeboard using a thickness tape. The thickness tape is connected with a brass weight, and when measuring the various variables of interest, the tape should be unfolded and the brass weight should be lowered down into the hole until it is below the ice. Then, one should gently pull the tape so that the brass weight is up against the bottom of the ice. From here, the following is observed (Mahoney and Gearheard, 2008 [RD71]):

- <u>Sea ice thickness</u>: where the top of the ice meets the tape.
- <u>Ice freeboard</u>: The distance from the ice surface to the water surface.
- <u>Snow depth</u>: If the snow has been disturbed while drilling, the snow depth must be measured using a ruler somewhere near the hole.

5.2.5.3 Meterstick snow thickness

During various ground-based campaigns, snow thickness observations may be acquired using a pointed meterstick. The pointed meterstick is pushed vertically through the snow until it reaches a firm interface, which is assumed to be the ice surface, and the rule marking that aligns with the snow surface is noted. Generally, meterstick measurements are accurate to 1-2 cm due to the verticality being approximate and the snow surface not always being smooth. An example is the study by Pfaffhuber et al. (2017) [RD83], who investigated snow thickness profiling in Antarctica sea ice using 1468 snow thickness values in combination with GPR data. For a detailed discussion on in situ snow thickness measurement techniques see, for example, Sturm (2009) [RD105].

5.2.5.4 Ground penetrating radar (GPR)

Snow thickness has been determined from ground-penetrating radars (GPRs) which have been both airborne and ground-based. Airborne (helicopter-based) GPRs has been experimented with with since the 1990s and early 2000s to map snow thickness on Arctic sea ice (Lalumiere and Prinsenberg, 2009 [RD67]) and Pfaffling (2007) [RD85] presented additional helicopter-based GPR data, which showed that only thick and undeformed snow could be identified in the radargrams. Pfaffhuber et al. (2017) [RD83] investigated ground-based GPR over Antarctic sea ice, which showed remarkable accuracy when compared with in situ meterstick data.

5.2.5.5 Ground-based electromagnetic (GEM) induction

Geonics EM31SH instrument [RD130] used for GEM observations in the Arctic during CryoVex 2017 (Haas et al., 2017 [RD35]). It has a coil spacing of only 2 m and operates with a signal frequency of 9.8 kHz. For the observations used in the study of Haas et al. (2017) [RD35] the instrument was mounted onto a small toboggan and operated in horizontal dipole mole, and dragged while walking along the profiles. Data was acquired with a sampling frequency of 1 Hz and georeferenced by GPS. At each site, two or three drill hole measurements were carried out at the location of the GEM measurements to confirm the proper calibration of the instrument. The accuracy of the GEM measurements was +/-0.1m over level ice up to 4 m thick (Haas et al., 2017 [RD35]). GEM measurements over rough, deformed ice are less accurate where maximum ridge thicknesses can be underestimated by as much as 50% (Haas and Jochmann, 2003 [RD30]).

5.2.5.6   Snow density and salinity

Snow densities are measured in situ by digging a snow pit and taking a known volume of snow and finding the associated mass. The mass/volume provides the density. Commonly used procedures are to use a tube-, box- or a wedge-like density cutter with known volume. This may be made of plastic or aluminium. It is only possible to measure the density of a snow layer if it is as thick as or thicker than the snow sampling tube, this also yields snow between layers of ice lenses. If the temperature gradient is small and the snow grain size is homogeneous throughout the layer, it is possible to take a representative snow density sample by using the density cutter. The snow sample is typically put into a plastic bag and the content is weighted on a dedicated weight. If the snow layer is wet, it is not possible to make a density measurement. If the snow sample is melted the salinity can be measured by using a salinometer. The procedures for snow density measurements and related biases, precision and vertical resolution can be found in (Proksch et al. 2016 [RD88]). The reference data was obtained in a controlled laboratory environment and in the field. In general, but not over sea ice, however, similar procedures are used over sea ice.

5.2.6   New Cal/Val Technologies

New innovative technologies are constantly being developed to improve our understanding of the sea ice and the current sensors used to derive sea ice information. In this section, we will briefly describe some of the more recent studies that have used new technologies to investigate sea ice or snow parameters of relevance to sea ice altimetry.

5.2.6.1   New sensor for Ice-T buoy to estimate snow depths

Currently, the Ice-T buoy can provide estimates of snow load through appropriate signal processing, either from thermal gradients, or from the under-ice pressure sensor. But these estimates are rather crude for a variety of reasons (e.g. thermistor spacing for the thermal approach, or uncertainty in ice density for pressure measurements).

To meet the accuracy required for satellite validation, an integration of a small frequency modulated continuous-wave (FMCW) 120-GHz frequency radar system to detect the snow surface and a similar 24-GHz frequency radar system that has snow penetrating capabilities, has been performed and tested during the St3TART 2022 spring campaign in Baffin Bay [TD-13-2] by the providers of the Ice-T buoy, LOCEAN. This development is based on the performance of such lightweight radars (at 80 GHz frequency), assessed a few years ago, for the determination of snow height (Ayhan et al., 2016 [RD11]). These tests, which were performed at the Centre d'Etudes de la Neige (CEN) / Meteo France facilities in the French Alps, showed that the 80-GHz FMCW radar system can be used for snow height determination with a precision of a few millimetres. The system can be employed in severe weather conditions and is immune to fog, rain, snowfall, or changing light conditions due to negligible attenuation by precipitation and is thus well suited for autonomous Arctic stations.

Tests further showed that the radar system allows measurements over a wide inclination range, which is important in a snow-on-sea-ice application to avoid measurements too close to the buoy, which can be biased by snowdrift in the wake of the instrument.

5.2.6.2   GNSS reflectometry

The potential of using GNSS-reflectometry (GNSS-R) for sea ice applications has been studied more in recent years (reviewed in Yan and Huang, 2019), however more work is still required in order to properly estimate altimetry-related sea ice information (such as sea ice thickness) from GNSS-R. Airborne tests showed a sensitivity to ice reflectivity which was reflected in the peak power of the GNSS-R waveform changing significantly, showing the potential of using GNSS-R for sea ice retrievals. Furthermore, ground-based observations of the ratio between direct and reflected signals (ρ) were investigated for sea ice thickness retrievals where an empirical relationship between these parameters were obtained through a fitting process. The empirical formula was given as:

$$T = 2.086\rho^{-0.021} - 2.697, \qquad (5.1)$$

and was verified in the study of Gao et al. (2017) [RD28] for sea ice thickness of 10 cm to 20 cm.

The application of GNSS-R for Arctic-wide sea ice thickness estimation was investigated in the study of Yan and Huang (2020) [RD122]. Using GNSS-R, specifically the reflectivity data from the TechDemoSat-1 (TDS-1) satellite, in combination with a proposed reflectivity model, a good estimate of thin sea ice thickness (less than 1 m) was derived. The GNSS-R derived sea ice thickness was compared with reference data from the Soil Moisture Ocean Salinity (SMOS) satellite, and the combined SMOS/Soil Moisture Active Passive (SMAP) measurements. A correlation coefficient (r) of 0.84 was obtained when comparing with SMOS and of 0.67 when comparing with SMOS/SMAP. An example of the derived SIT is shown in Figure 5.15.
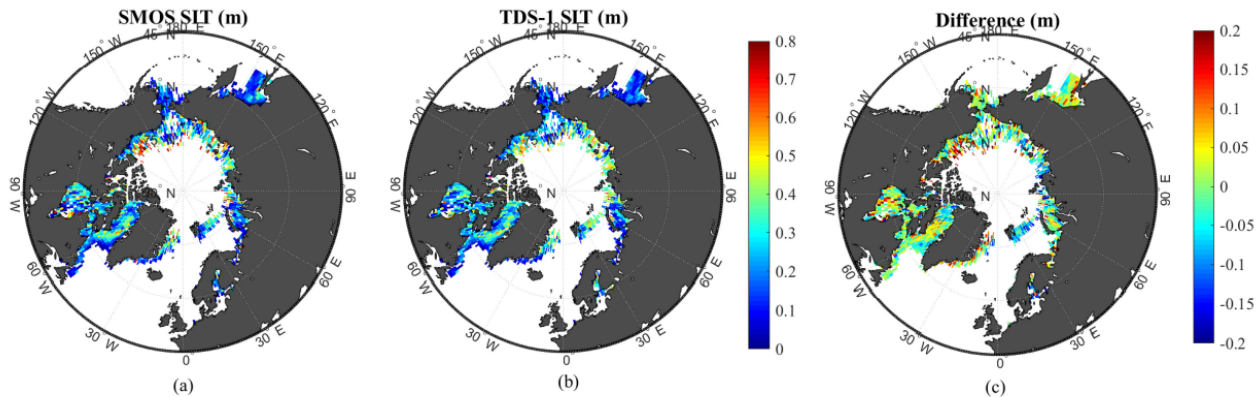

Figure 5.15: Sea ice thickness from SMOS (a), GNSS-Reflectometry (b) and differences between these (c). From Yan and Huang (2020) [RD122]

Noteworthy is the FSSCat mission, launched in September 2020 and winner of the 2017 ESA Sentinel Small Satellite Challenge and the Copernicus Masters competition, which operates a payload that includes an L-band microwave radiometer and GNSS-R. As part of the calibration and validation activities of FSSCat, a GNSS-R instrument was deployed during the MOSAIC expedition. The study of Munoz-Martin et al. (2020) [RD77] presents some of the first results of the PYCARO-2 instrument, focused on the GNSS-R techniques used to measure snow and ice thickness. They show that under general conditions, sea ice and snow thickness can be retrieved using multiangular and multi-frequency data.

While currently methods are still less mature than altimetry-based sea ice thickness, there is potential for additional validation data in the sense of ground-based GNSS-R observations as presented by Munoz-Martin et al. (2020) [RD77], or by comparing Arctic-wide sea ice thickness estimations as has been attempted in the study of Yan and Huang (2020) [RD122], although more work is required to ensure that the thicker sea ice is derived properly.

5.2.6.3   Drones

The use of drones for obtaining reference measurements in the Arctic has been of great interest in the recent years, and while UAVs have been utilised particularly over inland water, open ocean and for glaciology investigations (Gaffey and Bhardwaj, 2020 [RD26]), limited studies have been made on using UAVs over sea ice. A recent review paper by Gaffey and Bhardway (2020) [RD26], describing the latest advances and prospects of applications of UAVs in the cryosphere, showed how 103 peer-reviewed articles, theses etc. related to studies of UAVs in the cryosphere had been published during 2014-2019, and only two of these covered observations of the sea ice. The platforms of the UAVs used in these studies appeared to primarily carry optical images, although it was not clear from the review paper exactly which of the studies looked at sea ice, particularly, and how they investigated them. However, in comparison, 36 of the papers were focused on glaciers. This showcases a need for investigation of the utilisation of drones to validate the sea ice observations, but also highlights the amount of challenges and issues that such an enterprise entails.

5.2.6.4   Autonomous Underwater Vehicle (AUV)

Mapping of ice below the surface using sonars mounted on an AUV has been tested repeatedly since 2002 to measure 3D mapping of sea ice (Wadhams and Krogh, 2019 [RD110]). The AUV has so far relied on a tether to secure recovery of the AUV in ice infested waters, limiting the operational range, and has further been challenged by large heavy AUV's. Bo Krogh ApS has developed an underwater buoy communication and positioning system (USBL) to secure safe navigation of a small AUV without a tether, currently tested to a range of up to 2 km from the deployment site.

Bathymetric sonar mounted on an AUV was deployed underneath the sea ice in Cape Evans in Antarctica in November 2014, and the study of Lucieer et al. (2016) [RD69] shows encouraging results in using this to estimate sea ice thickness. Here, the ice thickness (T) was determined by:

$$T = D_{\text{pressure}} - D_{\text{swath}},$$

(5.2)

where D_{pressure} represent the AUV depth calculated from a pressure sensor mounted on the AUV, and the D_{swath} represent the derived GeoSwath AUV depth presented in the study of Lucieer et al. (2016) [RD69] (see Figure 5.15). They compared the thickness observations/pressure sensor depths with ice core depths acquired at collocated sites and found between 0.94% –15.54% difference of ice thickness, which shows some potential is applying different instrumentation to remotely steered vehicles.

If combined with airborne or drone data measuring the ice freeboard (or total freeboard + snow depth), these measurements can in combination provide information about the sea ice freeboard to draft ratio for different sea ice types and settings (Doble et al. 2011 [RD19]).
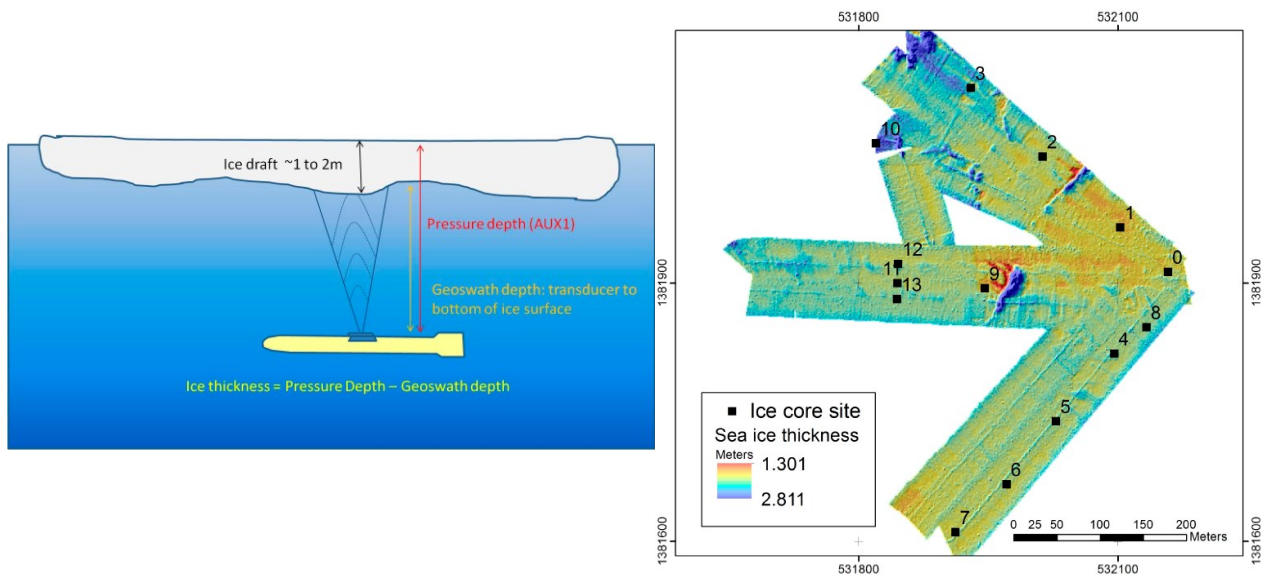

Figure 5.16: Principles of upward looking sonar mounted on AUV (left) and ice draft from survey site (right) from Lucieer et al. (2016) [RD69]

5.2.6.5   Ground-based radar observations: Ku-band and KuKa radar

The sea ice altimetry is currently based on the assumption that, for Ku-band radars, the radar pulse penetrates fully to the snow-ice interface (after removing the impact of slower propagation speed through snow). However, while this assumption holds for dry, cold and non-saline snow, once the snowpack changes characteristics, it may shift the backscattering interface (scattering horizon) upwards in the snowpack.

To investigate when this happens and its impact, a ground-based Ku-band radar was used over Antarctic sea ice [RD118], since the snow on Antarctic sea ice often experiences unfavourable conditions for altimetry. Here, they observed that for snow with no morphological or flooding features, the backscattering interface was at the snow-ice interface for 83% of the data. For snow with morphological or flooding features, the backscattering interface differed: In 42% of the returns, the backscattering interface was the air-snow interface; 30% originated from the snow-ice interface; 23% from a layer within the snowpack, and 3% were ambiguous. These results highlight a topic of high interest for the sea ice community, and the results of Willatt et al. (2010) [RD118] has, together with the opportunity of deriving snow depth from dual-frequency radar altimeters, paved the way for the new KuKa ground radar [RD101]. KuKa is a ground-based Ku- and Ka-band radar that can map in two modes (nadir/staring or scatterometer). KuKa is expected to provide valuable insights regarding the limitations of radars when travelling through snowpacks with morphological or flooding features. Recently published work (Stroeve et al., 2022 [RD102]) presented how, even in the Arctic, the scattering horizon changes

depending on the snow conditions. This is especially important with the changing climate and increasingly wetter precipitation occurring in the high Arctic even during winters. Therefore, exploring the KuKa data and impact of upsampling from ground-based Ku-band radar observations to satellite-based is of great interest to the sea ice community.

5.2.6.6 SnowMicroPen (SMP)

Through a combination of snow pit and SnowMicroPen (SMP) observations, the study of King et al. (2020 [RD48]) derived snow density on sea ice estimates for 14 sites in the Canadian Archipelago and Arctic Ocean. After calibrating with a SMP profile, they were able to provide 58 882 layer-classified estimates of snow density on sea ice equivalent to more than 600 individual snow pits. Here, they observed an average bulk density of 310 kg m^{-3} with clear separation between FYI and MYI environments. Lower densities on MYI (277 kg m^{-3}) corresponded with increased depth hoar composition (49.2 %), in strong contrast to composition of the thin FYI snowpack (19.8 %). Based on their results, they suggest that snow density observations could more easily be sampled using the SnowMicroPen compared to former in situ technologies. This would be of great benefit to future in situ campaigns which could more easily obtain sea ice density observations and would likely be able to sample a larger area.

5.2.6.7 Thermal infra-red cameras for lead classification

A recent study has utilised a thermal infra-red camera to map leads. Here, they utilised the thermal IR camera (VarioCAM HD head 680 GW) from InfraTec GmbH from a helicopter during the MOSAiC Expedition (see more in Section 5.3.6) to obtain thermal images of the sea ice. The detector format was 640 × 480 pixels with spectral range 7.5-14 µm (Thielke et al., 2022 [RD106]). These types of cameras can possibly provide good quality lead surface classification (Figure 5.17).
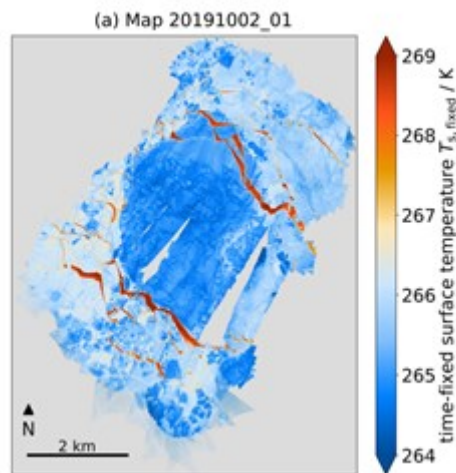
Figure 5.17: Mosaic of thermal IR images taken from helicopter over sea ice at the MOSAiC Expedition 2019. From Thielke et al. (2022) their figure 8.

5.3 Existing networks, surveys and campaigns

Validation data is still sparsely distributed in the Arctic and even sparser in the Antarctic due to the harsh environment and cost-expensive access. In Table 5.1 and Figure 5.18 we have collected and plotted available sea ice freeboard, sea ice thickness and snow depth validation data covering the satellite altimetry era from ERS-1 to present from different data sources ([RD149]).

Table 5.1 - Overview of available validation data covering the satellite altimetry era for the sea ice from ESA CCI Sea Ice project.

There are several techniques and different platforms measuring different geophysical parameters, e.g. sea ice freeboard, sea ice draft, total thickness. Below is provided an overview of existing Cal/Val data from campaign, and permanent (semi-permanent) solutions. We here intend to carefully assess these techniques.
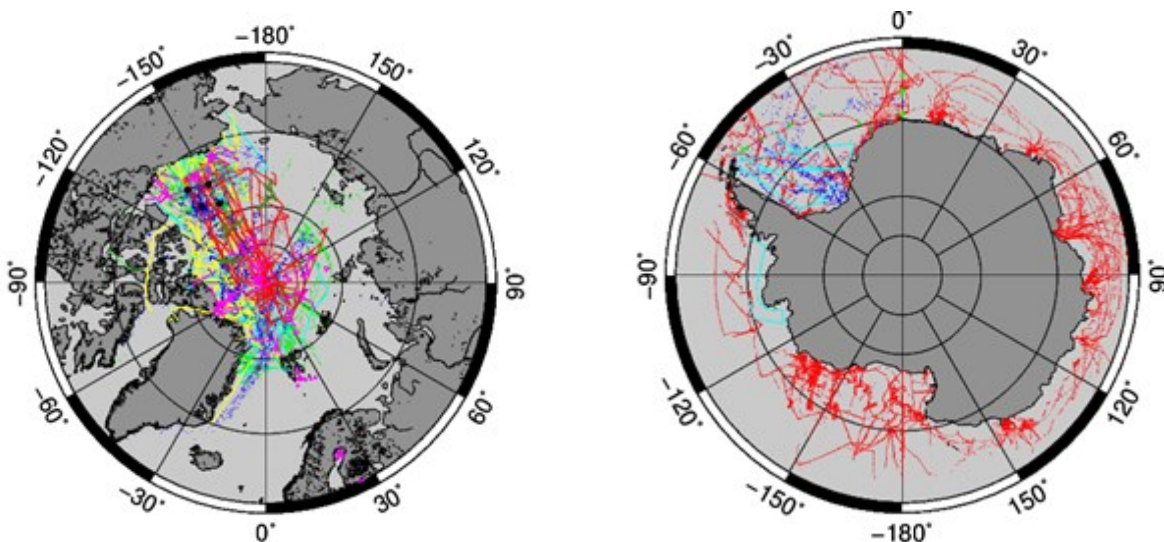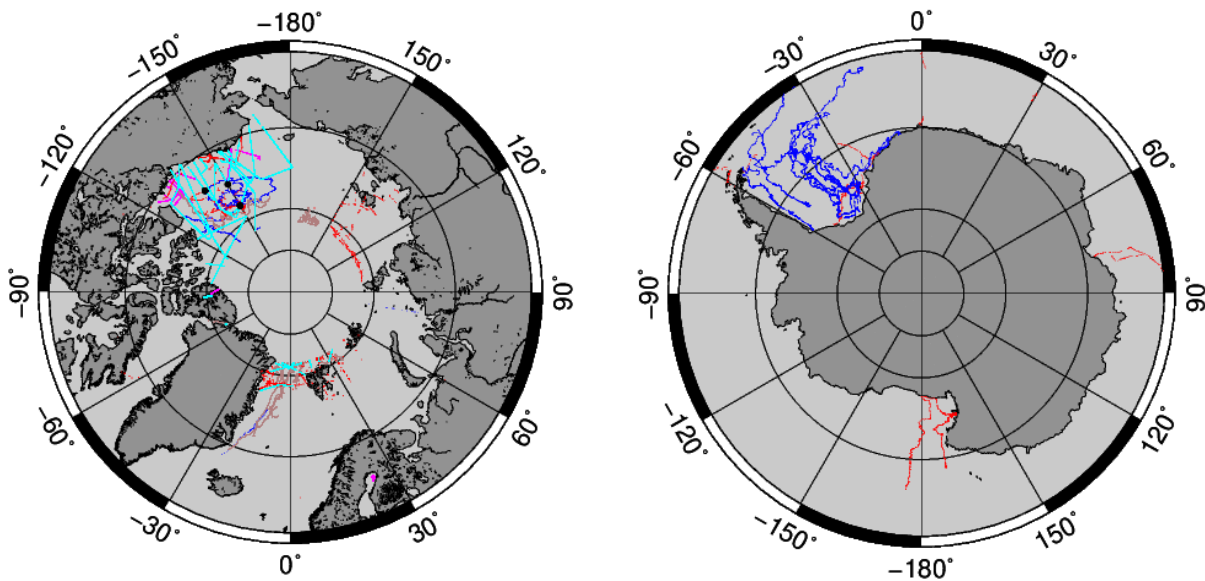
Figure 5.18: Overview of existing publicly available validation data within the Polar satellite era (upper plots) and limited to S3 operational period (lower plots) for the Arctic (left) and the Antarctic (right) corresponding to the overview in Table 5.1. Arctic observations are: CRREL IMB (blue), NASA OIB (yellow/cyan), AWI snow depth buoys (brown), ASSIST (red), AWI IceBird HEM/AEM (pink), BGEP ULS (black). Antarctic observations are: NASA OIB (cyan), ASPECT (red) and AWI snow depth buoys (brown)

5.3.1   Airborne campaigns

CryoVEx (Arctic and Antarctic): ESA CryoSat Validation Campaigns (Arctic March/April 2003-2019, Antarctic December 2017/January 2018) with airborne radars (ASIRAS, KAREN, CReSIS with Ku/ka-band) and high-resolution lidar altimeter (ALS) measurements of sea ice freeboard are currently not processed at a suitable level for direct validation of altimetry measurements. There are direct under-flights of S3A in 2016 and 2017 (see Figure 5.19: Overview of S3A under-fights from ESA CryoVEx 2017 and EU ICE-ARC airborne 2016 campaign.Figure 5.19), but these have only been used in the very preliminary state of the S3 data processing. The overall objective of all CryoSat-2 validation activities is thus to assess and quantify uncertainty in the CryoSat-2 measurements of sea ice thickness and land ice thickness change. The principal means for carrying out this program will be through dedicated, independent, ground-, and airborne campaigns along with detailed investigations of retrieval methods applied to the satellite measurements, as described in Table 5.2.

Cryo2IceEx (Arctic and Antarctic) 2022: The aim of the ESA Cryo2IceEx is to underfly dedicated Cryo2Ice orbits. The instrumentation in the Arctic campaign includes CReSIS Ku/Ka-band radar, ALS and GoPro camera. Due to weather and a mal-function of IS2 none of the Cryo2Ice orbits were underflown. The campaign was coordinated with St3TART and SILICE campaigns. The Antarctic campaign was coordinated with UK NERC funded project Defiant using for the first time a British Antarctic Survey (BAS) owned DASH-7. The larger platform allowed the use of a multiple suite of instruments including CReSIS Ku/Ka and combined C/S-band snow radar, ALS, several GoPro cameras, radiometer and GNSS Reflectometry. One dedicated Cryo2Ice orbit and several CS2 and IS2 orbits were successfully underflown over sea ice in the Weddell Sea.

Table 5.2 - CryoSat-2 validation requirement

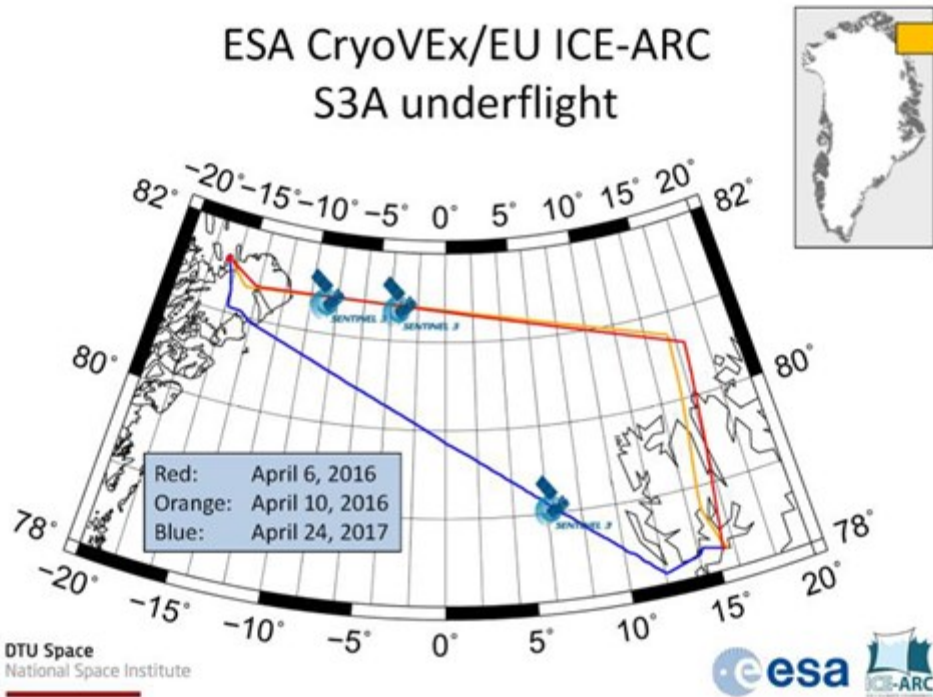| Sea Ice			
5)	Snow loading	4.2	*In situ* measurements
			Reappraisal of existing snow depth records
			Very narrow beam firn radar measurements
6)	Ice Density	4.3	Helicopter electromagnetic thickness and freeboard measurements
			Sea ice coring
7)	Preferential sampling	4.1 4.5	Coincident laser altimetry and imagery
			Coincident CryoSat-2 measurements and imagery
8)	Freeboard error – geometric & penetration errors	4.4.2 4.4.3	Comparison with airborne or ICESat laser measurements
			Detailed investigation of time-variant 13.8Ghz volume scattering using airborne laser/radar systems
9)	Freeboard error – ocean tide error	4.4.1 4.4.2	Direct measurement from CryoSat-2 satellite data
10)	Freeboard error – ocean geoid error	4.4.1 4.4.2	Comparison with CHAMP and GRACE satellite measurements
			Comparison with ground survey
11)	Freeboard error – ocean variability error	4.4.1 4.4.2	Direct measurement from CryoSat-2 satellite data
12)	Freeboard error – atmospheric refraction error	4.4.1 4.4.2	Model investigations of expected contribution

Figure 5.19: Overview of S3A under-fights from ESA CryoVEx 2017 and EU ICE-ARC airborne 2016 campaign.

IceBird (NH): AWI Airborne electromagnetic (AEM) sounding of total sea ice thickness in the Arctic (March (<5%)/April) from 2004-2019 campaigns. AEM tends to underestimate thick and deformed ice. Since 2019 the instrument package includes a snow radar.

Figure 5.20: IceBird ice thickness surveys carried out with the Polar 5 and Polar 6 aircraft between 2009 and 2017 (credit: AWI, [RD131]).

OIB (NH+SH): NASA Operation IceBridge total sea ice freeboard, snow depth, sea ice thickness, and surface roughness data from the Arctic (March/April) and (October/November) Antarctic campaigns 2009-2019. In general, the OIB Arctic campaign data has been processed at a level directly comparable to satellite altimetry measurements including observations of total freeboard from ATM and snow depth from the CReSIS snow radar. On the contrary the officially published Antarctic campaign data is limited to total freeboards from ATM for the 2009 and 2010 campaigns. The Arctic snow depth products are provided as 6 different products based on different processing to account for e.g. side lobe effects. There should be direct under-flights of S3 in most previous data sets. The main instruments were the laser altimeters, where multiple versions of four different laser altimeters were deployed. Since OIB campaigns were surveyed at a relatively low elevation above ground level (AGL) of approximately 460 m, multiple altimeters were suitable. For campaigns at higher altitudes, only the Land, Vegetation and Ice Sensor (LVIS) instrument had sufficient ranging capabilities. Main instruments ATM with two additional types of laser altimeters were also deployed, however according to MacGregor et al. (2021) [RD70], they appear to have been used primarily for land ice purposes. Therefore, they will not be further described. Of snow radars, the following instruments were deployed during the OIB surveys: Beyond these key instruments were also gravimeters, magnetometers and various optical/infrared/hyperspectral imagery systems used to either validate the other airborne observations (such as for identification of leads or ice ridges) or for different sciences or other studies.

OIB was a 13-year (2009-2021) airborne mission hosted by NASA which aimed to survey land and sea ice across the Arctic, Antarctic and Alaska. The primary goal of OIB was to bridge the gap in laser altimetry observations between NASA's ICESat (2003-2009) and its follow-on, ICESat-2 (launched 2018). OIB used 15 different aircrafts and conducted 968 science flights, of which 42% were repeat surveys of land ice, 42% were surveys of previously unmapped terrain across the ice sheets and 16% were surveys of sea ice. Overall, in the Arctic OIB flew 22 campaigns between 2009 and 2019 on nine different aircrafts based from five different locations and using more than 20 instruments - overall 124 of the 464 flights conducted during these 22 campaigns were of sea ice. OIB flew 17 Antarctic campaigns during 2009-2019 on six different aircrafts based from four different locations and using more than 25 different instruments - of these 320 flights, 34 were of sea ice. Furthermore, OIB also flew 26 Alaskan flights and 184 glacier flights (MacGregor et al., 2021) [RD70].

Beside laser altimetry, NASA formulated that the deployed aircrafts in OIB should also be fully exploited to make ancillary measurements relevant to cryospheric sciences. This included deploying multiple radar sounders, gravimeters, magnetometers, and visible, infrared, and hyperspectral cameras - all to measure additional surface and subsurface geophysical properties (MacGregor et al., 2021 [RD70]).

In 2018, the science requirements set forward during the OIB campaigns were revised and approved, which reflected adjustments needed in the light of logistical and budget limitations, compared to the original science requirements set out in 2010 (shortly after OIB took off).

Table 5.3 provides the baseline science requirements for sea ice.

A feasible set of about 30-50 potential flights in each hemisphere each year were planned, where the sets were purposefully larger than the number of available flights, to ensure that the teams would not run out of options while undertaking the campaign. For any given flight day, the list of possible surveys was constrained by regional weather and other logistical constraints, which whittled feasible surveys to a handful from which the highest priority mission was typically selected. Finally, a data management plan was implemented in consistency with NASA standards, which stated that within 6 months of the conclusion of each campaign, the data were intended to be processed and delivered to and released by NSIDC (MacGregor et al., 2021 [RD70]).

5.3.2   Moorings

Provide continuous point measurements of sea ice draft by use of upward looking sonars:

BGEP ULS: Sea ice draft measured by Beaufort Gyre Exploration Project (BGEP) moored upward looking sonars in the Beaufort Sea (2003-2018);

NPI ULS: Norwegian Polar Institute (NPI) moored upward looking sonars in Fram Strait (1990-2018);

AWI ULS: moorings in Fram Strait;

NPEO ULS: Sea ice draft data set from NPEO ULS moorings (2001-2010);

Laptev ULS: Sea ice draft from ULS/ADCP mooring in Laptev Sea (2013-2015);

AWI ULS: sea ice draft from moored ULS, Antarctic, to validate ERS-1/2 (1990-2011).

5.3.3   Submarine Cruises

Provide measurements of draft by upward looking sonars:

SCICEX: Sea ice draft from Submarine data SCICEX cruises 1993, 1996-2000, 2005, 2011, (2012), 2014, (2016) primarily to validate ERS-1/2 products;

HMS Tireless: Submarine data from HMS Tireless data;

Table 5.3 - Baseline Science Requirements for OIB Sea Ice Flights (MacGregor et al., 2021 [RD70]).

SI1	Make surface elevation measurements of the water, ice, or snow with a shot-to-shot independent error of less than 10 cm and correlated errors that contribute less than 1 cm to the mean height error in either sea surface or sea ice elevation. The spot size should be 1 m or less and spaced at 3 m or less
SI2	Make elevation measurements of both the air-snow and the snow-ice interfaces to an uncertainty of 3 cm, which enables the determination of snow thickness to an uncertainty of 5 cm
SI3	Provide annual acquisitions of sea ice surface elevation in the Arctic and Southern Oceans during the late winter along near-exact repeat tracks in regions of the ice pack that are undergoing rapid change; flight lines shall be designed to ensure measurements are acquired across a range of ice types including seasonal (first-year) and perennial (multi-year) sea ice to include, as a minimum: **Arctic** 1. At least two transects to capture the thickness gradient across the perennial and seasonal ice covers between Greenland, the central Arctic, and the Alaskan Coast 2. The perennial sea ice pack from the coasts of Ellesmere Island and Greenland north to the pole and westward across the northern Beaufort Sea 3. Sea ice across the Fram Strait and Nares Strait flux gates 4. The sea ice cover of the Eastern Arctic, north of the Fram Strait **Antarctic** 1. Sea ice in the Weddell Sea between the tip of the Antarctic Peninsula and Cape Norvegia 2. Mixed ice cover in the western Weddell Sea between the tip of Antarctic Peninsula and Ronne Ice Shelf 3. The ice pack of the Bellingshausen and Amundsen Seas
SI4	Include flight lines for sampling the ground tracks of satellite laser altimeters (ICESat and ICESat-2) and radars (CryoSat-2 and Sentinel-3). In the case of CryoSat-2, both OIB and CryoSat-2 ground tracks should be temporally and spatially coincident whenever possible. At least one ground track of each satellite should be sampled per campaign
SI5	Conduct sea ice flights as early as possible in the spring flight sequence of each campaign, prior to melt onset
SI6	Collect coincident natural colour visible imagery of sea ice conditions at a spatial resolution of at least 10 cm per pixel to enable direct interpretation of the altimetry data
SI7	Conduct sea ice flights primarily in cloud-free conditions; however, data shall be retained under all atmospheric conditions with a flag included to indicate degradation or loss of data due to clouds
SI8	Make full gravity vector measurements on non-repeat, low-elevation (<1,000 m) flights over sea ice to enable the determination of short-wavelength (order 10–100 km) geoid fluctuations along the flight track to a precision of 2 cm
SI9	Make available to the community instrument data on sea ice surface elevation and snow thickness within 3 months of acquisition and derived products within 6 months of data acquisition

5.3.4 Drifting buoys

Providing snow depth and/or sea ice thickness and surface temperature:

CRREL/AWI IMBs (NH): ice mass balance buoys (2000-present), however, no snow or ice data is available for 2000, 2001 and 2016;

Snow depth buoys (NH+SH): from Alfred Wegener Institute (AWI) (2013-present).

SHEBA (NH): The Surface Heat Budget of the Arctic Ocean (SHEBA) experiment took place in 1997/1998 and consisted of distributing an array of over 100 mass-balance measurements over a 100 km^2 area and monitoring the sites for a full year (Polahenski et al., 2011 [RD87]).

5.3.5 Ship cruises

Visual inspection of sea ice thickness (snow depth) from ships. Tend to underestimate the general sea ice thickness as the ships tend to follow the most optimal route for sea ice navigation.

ASSIST (NH): Sea ice thickness and snow depth from Northern Hemisphere using the Arctic Shipborne Sea Ice Standardization Tool (ASSIST), (2006-2021);

ASPeCt (SH): Southern Hemisphere ASPeCt sea ice thickness from ship cruises (1981-2019). The Antarctic Sea Ice Processes and Climate (ASPeCT) program was established in 1997 by the Scientific Committee on Antarctic Research (SCAR). Within the project, one of the first objectives was to collate the many sea ice logs kept from cie breakers operating in the Antarctic sea ice zone.

5.3.6 In situ

Temporary ice camps: Russian NP drillings with observation of sea ice thickness, sea ice freeboards, and snow depth, e.g North Pole (NP) 37-39 drifting stations; Russian North Pole drifting stations: in situ and classified data like Warren 1999 [RD115] and SS18 climatology. Other temporary ice camps include US Ocean Naval Research ice camps, the SEDNA ice camp (2007), GreenArc (2009), EU GreenIce (2004), EU Damocles (2007)

Supported by aircraft/helicopter: ESA CryoVEx spring campaigns 2006, 2008, and 2017.

CanCoast: See also Section 5.2.3

Shipbased:

- N-ICE2015
- UNCLOS, Oden, in summer primarily
- CHINARE (Chinese National Arctic Research Expedition)
- US Healy
- Polarstern (several expeditions)

MOSAiC (Arctic); collected a huge amount of validation data during its drift over the Arctic Ocean from September 2019 to October 2020. In particular the dual-frequency ground sensor KuKa is of interest for this assessment.

Figure 5.21: Schematic of the MOSAIC setup [RD132]

MOSAIC (the Multidisciplinary drifting Observatory for the Study of Arctic Climate) was the first every year-long polar expedition that took place during September 2019-2020, where many aspects on sea ice were investigated from at various scales and from various places (under ice, on ice and above the ice). The backbone of MOSAiC was the year-round operation of RV Polarstern, drifting with the sea ice across the central Arctic from September 2019 to October 2020. During the set-up phase, RV Polarstern entered the Siberian sector of the Arctic under late summer's thin sea ice conditions. A distributed regional network of observational sites was set up on the sea ice in an area of up to ~50 km distance from RV Polarstern. The ship and the surrounding network drifted with the natural ice drift across the polar cap towards the Atlantic, while the sea ice thickened during winter [RD43].

The expedition took place during September 2019 to September 2020, which means that data availability and accessibility is still limited. The MOSAiC participation teams are currently processing and studying the data, since they have a beforehand-right to use the data. This also means that labs and scientists not affiliated with the MOSAiC expedition have to wait until January 2023 to get a hand of all the data acquired during MOSAiC, since it will not be fully publicly available before that. However, some labs and teams have already published various datasets and studies, which provides a first-hand-view of the measurements obtained during the expedition, the conditions during the expedition and potential future work related to such expeditions and observations as well.

5.3.6.1 Central observatory and the ICE CITY (ice camp)

The Central Observatory was located at/near Polarstern (see Figure 5.21), and was the primary area of data acquisition. From here observations of snow pits and ice cores would be performed, the spatial distribution of snow depth and ice thickness has been investigated and manual measurements of morphological properties of pressure ridges performed. Beyond that, from the Central Observatory various other observations were made such as: walking surveys, airborne observations using helicopters or UAS to estimate melt ponds.

There were several measurement sites used to measure different ice types and conditions at daily/weekly visits - such as surface conditions, physical properties (snow pits, ice cores), mass balance (snow depth, ice thickness, ice growth, surface melt, and bottom melt), and optical protiers. Complementing the selected site there were a few semi-autonomous stations to measure ice mass balance and spectral incident, reflected and transmitted radiation and those would have web cameras. Surveys were also performed on snow depth, ice thickness, pond depth, and spectral albedo measured along survey lines that were expected to be hundreds of meters in length using instruments installed on sledges or carried (e.g., EM ice thickness devices, spectroradiometer, cameras). Lidar surface topography would also be mapped over areas of hundreds of meters. Underwater remote operated vehicles would be used to measure spectral transmission and under ice topography along transects (IASC, 2016 [RD43]).

5.3.6.2 Distributed networks

For sea ice, the overarching goal was to extend the observations made at the Central Observatory ice floe to to characterize the variability of ice properties over an ensemble of floes and over an annual cycle. Four primary areas were targeted, whereas two were of particular interest to sea ice altimetry: (1) snow and ice morphology, including surface topography, snow depth and ice thickness distributions, ice floe size distribution, lead fraction, ridge characteristics, melt pond distributions, and the spatial relations of these features, and (4) ice motion, deformation, and internal stress (IASC, 2016 [RD43]).

5.3.6.3 Instruments/observations of particular interest

At the Central Observatory

Small installations were monitored on Polarstern to monitor the ice camp and the surrounding ships (visible and infrared cameras). Furthermore, the ship radar was used for continuous monitoring of sea ice movements and deformation scales of 5 km – 10 km around Polarstern. Furthermore, bridge observations were logged daily to describe the sea ice conditions. At the ice camp, most of the measurements and work of the sea ice team are performed within a few kilometres of the ice camp close to Polarstern. Key observations of relevance to sea ice altimetry and sea ice thickness observations, since there were many different observations made, include (IASC, 2018 [RD44]):

- Transects of sea ice thickness, snow depth, freeboard in order to obtain sea ice and snow mass balance
- Snow cover studies, widely spread over the ice camp, to quantity snow accumulation as well as surface topography and redistribution
- ROV based work in the uppermost meters of the ocean with a focus on, but not only, sea ice draft
- Sea ice and snow sampling from ice cores to describe the physical properties of the sea ice and the snow cover
- Investigation of surface properties and their changes with respect to roughness, melt processes and melt pond formation and evolution
- Sea ice deformation (lead opening and ridging) events

At the Distributed Network

A significant part of sea ice observations was expected to be performed through autonomous measurements by ice tethered platforms (buoys). The buoy systems were expected to include some combination of Ice Tethered Profiler (ITP), Ice Tethered Micro-mooring (ITM), Ice mass balance (IMB), autonomous ocean flux buoy (AOFB), O-buoy, Ice-atmosphere-ocean observing system (IAOOS), surface radiative flux buoy, and potentially also others (IASC, 2016 [RD43]). Time series on sea ice thickness, ice growth, surface melt, bottom melt, snow depth, accumulation and ablation, temperature profiles through snow and ice etc., were gathered. Repeated visits at selected nodes of the distributed network allowed for complementary measurements in the form of local transects. Furthermore, the use of autonomous underwater vehicles (AUV) would also contribute to these observations. They were used on a weekly basis to connect the central observatory with different autonomous nodes of the network. In particular, a key instrumentation for the sea ice team was a n upward looking bathymetric multibeam sonar to map sea ice bottom topography. Potential of using a hovercraft for transect measurements within the distributed network was also a possibility (IASC, 2018 [RD44]). Since the data is still being processed, it is not fully disclosed exactly which or how measurements were made.

Airborne observations

Beyond the more local observations, airborne measurements would also be performed. They would allow for connecting the central observatory with scales beyond 20 km in order to upscale the local observations and to enable estimates of regional variability. Key variables in this aspect were: sea ice thickness, snow depth, surface topography, surface morphology, visible and infrared imagery, along with microwave properties of sea ice and snow. The airborne measurements were to be performed with helicopters from Powerstern whenever weather conditions would allow it. One additional airborne campaign during spring was also expected to take place during spring, and would allow for long-range measurement transects between the central observatory and land stations (IASC, 2018). The potential of using UAS was also presented in the Science Plan of MOSAIC (IASC, 2016), where the intention for the MOSAIC UAS programme was to have locally operated aircrafts, which would be locally launched and recovered either from the deck or from adjacent ice, and would likely have a range of about 5 km. The systems were to be used on a periodic basis (weekly at minimum) to provide important measurements of the spatial and vertical variability of key parameters (IASC, 2016 [RD43]). It is still not published which airborne data sets are available or exactly which measurements have been acquired, but will come in the future.

Intensive Observing Periods (IOPs)

Beyond the already mentioned observations, some intensive observing periods (IOPs) were also planned for the sea ice team. Here, sea ice, snow and melt pond studies at a secondary ice camp were planned, and would allow for more intensive observations of spring-summer properties and processes away from Polarstern. The ice camp was expected to be directly connected to one of the main nodes of the distributed network (IASC, 2018 [RD44]).

Below, Table 5.4 summarises the different types of observations expected to be made during MOSAIC including the method to be used and where it is expected to take place.

Table 5.4 - Observations and methods expected to be/used when surveyed during MOSAIC relevant for sea ice altimetry (does not include measurements related to melt ponds, optics, ocean under sea ice or additional other observations stated in IASC, 2018).

	Method	Ice camp and PS	Distr. networks	>20 km
Sea ice				
Thickness	Survey lines	Weekly		
	Drillings	Weekly		
	Buoys	Continuously	Continuously	Continuously
	Survey flights (EM)		Weekly (weather)	Weekly (weather)
	ROV, AUV	Weekly		
Mass balance	Stakes and wires	Weekly	Continuously	Continuously
	LIDAR and ROV	Weekly		
Bottom topography	ROV and EM	Weekly		
Freeboard	Levelling	Monthly		
	High prec. pressure sensors	Continuously		
Density	Coring	Monthly		
Salinity	Coring	Monthly		
	Ice harp	Continuously		
O18	Coring	Monthly		
Texture	Coring	Monthly		
Porosity (ice + ridges)	ROV + EM	Weekly		
Stress	Stress buoy	Continuously	Continuously	
	High prec. pressure sensors	Continuously		
Strength	Borehole jack	Opportunistically		

Floe size (distribution)	Survey flights (cameras)		Weekly	Weekly
Lateral melt/floe size	Survey flights	Days, seasonal	Weekly	Weekly
Core sampling processing	Freezer Lab	Weekly		
Snow				
Thickness	Survey lines	Weekly		
	Buoys	Continuously	Continuously	Continuously
	Survey flights (radar)		Weekly (weather)	Weekly (weather)
dg, rho, strati, hard, liquid w., ssa	Pits	Weekly (melt+)		
Snow water equivalent	Samples	Events		
Redistribution	Stations	Continuously	Continuously	Continuously
	Lidar	Events		
Salinity, O18	Samples	Events		
Temperature	Pits	Weekly (melt+)		
	Thermistor strings	Continuously	Continuously	Continuously
Surface roughness	LIDAR	Events	Events	Events
Surface properties	Cameras	Continuously	Continuously	Continuously
Others				
MW properties (L and Ku-band)	Scatterometer	Weekly	Weekly (weather)	Weekly (Weather)
	Station	Continuously		
Deformation	Ship radar	Continuously		
Ice conditions	Bridge observations	Daily		

5.4 Uncertainty estimates of existing validation data

The table below lists literature values for the uncertainties associated with several of the methodologies discussed in this section and was prepared by the ESA CCI+ Sea ice project. Methods for evaluating uncertainties are discussed in more detail in Sections 0 and 7.5 below.

Table 5.5 - Literature values for the uncertainty associated with different existing validation methods ([RD149]) their Table 4.

Campaign	Averaging methodology	Uncertainty estimates [m]	Uncertainty source
OIB (Altimetry)	EASE-Grid 2.0	Individual uncertainties available	Kurtz et al. (2016); Kurtz et al. (2015)
AEM-AWI (AEM)	EASE-Grid 2.0	±0.10 (SIT), ±0.10 (FRB)	SIT: Haas et al. (2007), FRB: Jutila et al. (2022)
ASSIST (VO)	EASE-Grid 2.0	±0.20	Hutchings et al. (2018)
ASPeCt (VO)	EASE-Grid 2.0	10-20% of actual thickness	Worby et al. (2008a, 1999)
IMB-CRREL (IMB)	EASE-Grid 2.0	±0.01****	Donald K. Perovich, Richter-Menge et al. (2006a)
SB-AWI (SDB)	EASE-Grid 2.0	±0.01	Personal comm.,Nicolaus et al. (2021)
BGEP (ULS)	Temporal	±0.05-0.10	Krishfield and Proshutinsky (2006)
AWI-ULS (ULS)	Temporal	±0.05 (summer), ±0.12 (winter)***	Behrendt et al. (2013a)
TRANSDRIFT (ULS)	Temporal	±0.05 (ULS),±0.96 (ADCP)	Belter et al. (2020), Belter et al. (2021)
NPI-FS (ULS)	Temporal	±2.7E-03 (1990-1991), 1.9E-03 (1991-2003), 1.3E-03 (2003-2006), 0.088E-03 (2007-2018) *	Sumata (2022), supplementary materials table 3
NPEO (ULS)	Temporal	±0.05	Morison et al. (2016)*****
SCICEX (ULS)	EASE-Grid 2.0	Bias: +0.29, Unc:±0.5**	Rothrock and Wensnahan (2007); NSIDC (1998, 2006)

VO: Visual Observation
*: Uncertainty of the monthly means Supplementary materials table 3
**: uncertainty based on 2·std
***:default: line correction for sound speed model:±0.23
****: 0.01 m accuracy in usual conditions 0.02 m if it is very cold the sensors do not work well during the melting season
*****: uncertainty estimate available from metadata

5.5 Calibration measurements for the FRM

5.5.1 Calibration

5.5.1.1 Corner reflectors

Corner reflectors are in principle easy to use and provide a benchmark for the "true" surface. They are easy to identify in airborne radar altimeter data. However, the results rely on exact knowledge of the position of the corner reflector both horizontal and vertical, and more challenging is to "hit" the target from an aircraft due to the rather narrow along-track footprint size (10 m – 15 m) of the airborne sensors.

Reference targets to calibrate the airborne observations are crucial to estimate accuracy, and such reference targets could be corner reflectors. As an example, during CryoVEx 2006 and 2008 Arctic campaigns, trihedral corner reflectors were deployed to provide a reference target above the snow surface for the radar, and the coordinates of these corner reflectors were measured using a hand-held GPS during the campaigns (Willatt et al., 2011 [RD117]).

As stated by Willatt et al. (2011 [RD117]), the knowledge of the corner reflectors' exact location is important for correcting the offset between the corner reflectors and the nadir track of the antenna. In their study, they investigated the locations of the corner reflectors using the ALS data of the 2006 and 2008 CryoVEx campaigns. They found that for all ALS data passes, the corner reflectors were not always visible – they attributed this to the spacing between the samples on the ground, and due to specular reflections of the laser beam away from the aircraft. They also investigated from which surface the highest amplitude radar return originated from (the snow-ice or air-snow interface) by comparing with the ASIRAS radar returns and measured snow depths. Here, they calculated the apparent distance from the corner reflectors apex to the surface as seen in the ASIRAS data. Thereafter, they compared this distance to the distances from the corner reflectors apex to the air-snow and snow-ice interfaces. However, first a correction must be applied to account for the fact that the ASIRAS observations were not directly above the corner reflectors. This correction required a precise location of the corner reflectors, which was achieved by comparing with the ALS data as described before. After calibrating by using these corner reflectors, they investigated the reflection of the radar signal

from ASIRAS - whether it originated near the snow-ice or the air-snow interface in different settings (dry and wet snow, respectively, as well as different sea ice types).

5.5.1.2 Lidar calibration building and crossovers

Calibration of ALS misalignment angles between ALS and INS can be estimated from successive overflights from different directions of the same building, where the position of the corners is known with high precision from GPS measurements. Thus standard procedure is to overfly these buildings for calibration purposes, several times during a campaign. As part of the processing routine, crossover statistics are derived for all repeated overflight within an hour of the first overflight. The quality of these crossover statistics varies depending on surface type, incidence angle and level of processing. In general statistics over sea ice is poor due to the drift of sea ice between intersections. The mean elevation differences in the cross-over points are generally less than 6 cm and typically represent errors in the GPS solutions. The standard deviation of the cross-over differences is typically on the order 5 cm – 10 cm over relatively flat surfaces, i.e. the Greenland Ice Sheet and landfast sea ice.
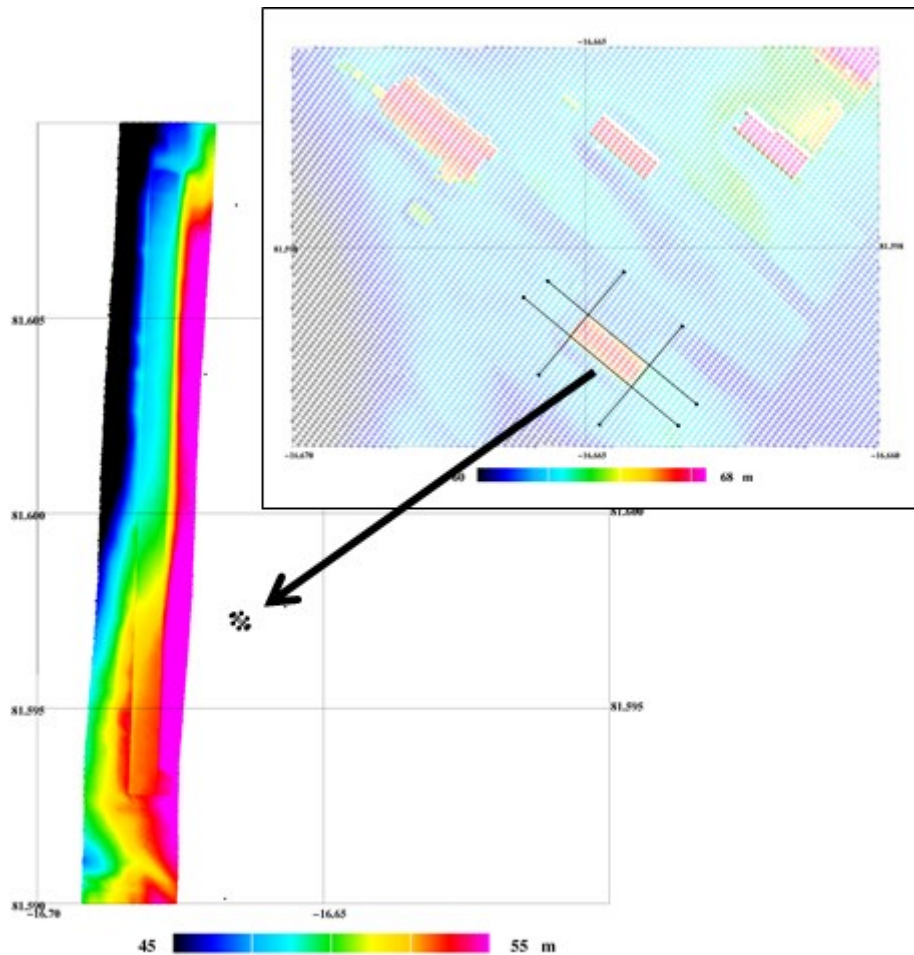

Figure 5.22: Example of ALS calibration over a building. This example is taken from Station Nord, Northern Greenland

5.5.1.3 Radar

Absolute measurements runway calibration or leads Calibration – absolute heights: To obtain absolute surface heights from ASIRAS and KAREN an offset needs to be applied to account for internal delays in cables and electronics. The offset is estimated by comparing ASIRAS and KAREN surface heights to surface heights obtained by ALS over a surface, where both the radar and the laser are known to reflect at the same surface. Such measurements are typically obtained by overflights of runways. Different biases apply for the different aircraft installations and retrackers. Corner reflectors also provide a reference frame for time-tagging but need very accurate measurements of the position of the corner reflector. The OCOG retracker was developed to give a quick and rough estimate of surface elevation and not to be as precise as possible. It may not be the optimal retracker in areas with several layers in the snow/firn, e.g. the percolation zone on ice sheets, see e.g. Helm et al. (2006) [RD38] and Stenseng et al. (2007) [RD100], and it is up to the user of the data to apply different retracker algorithms depending on the application. Roll angles are given as part of the attitude information, as it is common to remove roll angles above/below a certain threshold (±1.5° for ASIRAS) due to waveform blurring.

5.5.1.4 Buoys

In general, absolute observations are preferred for satellite validation, thus initial measurements of snow depth and ice thickness are needed.

5.5.1.5 Airborne Electromagnetic Induction (EM)-Bird

Calibration coils electrically connected for a few seconds and generate well defined In-phase and Quadrature voltage offsets (cf. spikes in Figure 5.23). The measured strength of the calibration voltage offsets is first used to phase the raw complex voltage components and then to convert the voltage measurements into ppm. Typical values of the calibration coefficients derived over the period of our 6 campaigns were (95.27 ± 1.98) µV/ppm, (97.76 ± 1.45) µV/ppm, (27.06 ± 0.64) µV/ppm, and (32.51 ± 0.93) µV/ppm for the Inphase and Quadrature signals of f_1 and f_2, respectively. The values show that the calibration has an uncertainty of less than ± 2% for f_1, and of approximately ± 3% for f_2.

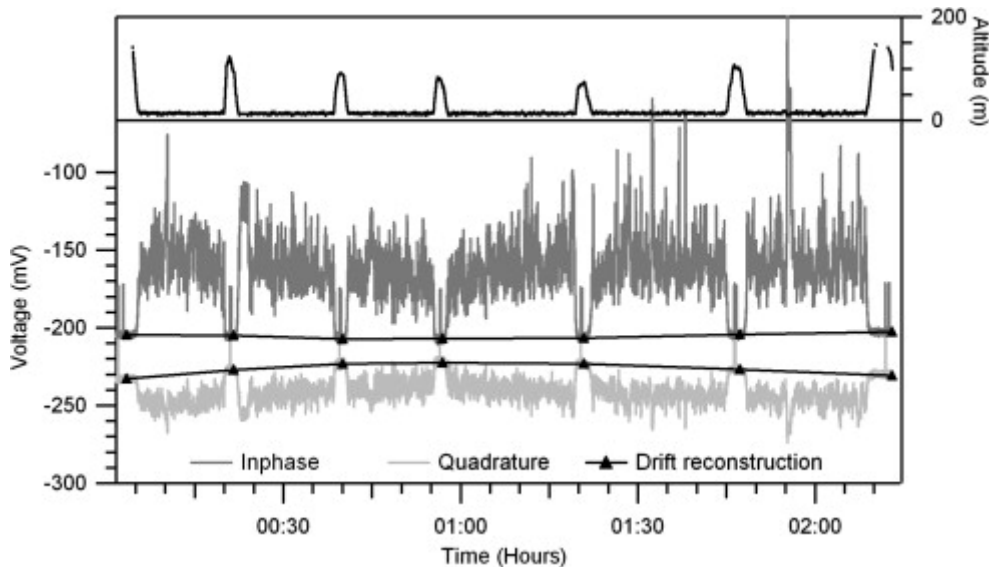**Figure 5.23 Records of Inphase and Quadrature voltages at f1 = 3.68 kHz, and flight altitude. Thick triangles mark the electrical drift determined during ascents to altitudes > 100 m above the sea surface. Note variations of high-altitude measurements due to noise. Singular spikes during high altitude flights are due to calibration signals induced by calibration coils (Haas et al., 2009 [RD33]).**

6 Learnings from alternative satellite missions

6.1 Learnings from other satellite missions' Cal/Val processes

Experience with the Cal/Val processes of other satellite missions can be valuable to understand likely performance of Sentinel 3 missions.

Basically, S3 Ku-band radar operates in SAR-mode, which is similar to the measurement mode of CryoSat-2 over sea ice, except for the coastal regions, where CryoSat-2 operates in its interferometric mode (SARIn), see Figure 6.1 for CryoSat-2 mode-mask. Thus, results obtained with CryoSat-2 over sea ice should in principle apply also for the S3 Ku-band. However, the processing of S3 level-1 data is not similar to CryoSat-2 level-1 processing. Indeed, CryoSat-2 processing turns out to be more suitable for sea ice applications. The differences in the processing of level-1 data also impacts the level-2 products. However, we will review CryoSat-2 validation efforts to support the S3 validation procedures and best practices.

Standard airborne satellite altimetry Cal/Val campaigns aim at under-flying the satellites along the orbit-track preferably timed to match the satellite pass during the flight. These approaches are very good for e.g. penetration studies, but the one-to-one correlation, i.e. by averaging the along-track airborne measurements over the satellite footprint size (Figure 6.2 upper plot), here approximately 300 m × 1600 m, and compare it to the re-tracked point-measurement of CS2, show very low correlation (ESA CryoVal-SI Technical Report, Haas et al. 2016 [RD34]) and the outcome is a "gun-shot" scatter-plot (Figure 6.3). It was concluded that the very narrow airborne observations were not representative for the larger CS2 footprint, but also drift can cause this effect. Different scales were used for averaging the airborne and CS2 satellite measurements and the best correlation was found by averaging both observations over 50 km intervals. This would require long and multiple transects, as the under-flights are usually in the order of 250 km – 500 km, depending on the aircraft endurance. We will look into alternative solutions, which might optimize the airborne validation of S3 (and CS2), i.e. by surveying several parallel lines along the satellite ground track to fully cover the across-track width of the satellite footprint, see example from ESA CryoVEx 2017 campaign (Figure 6.2, lower plot).
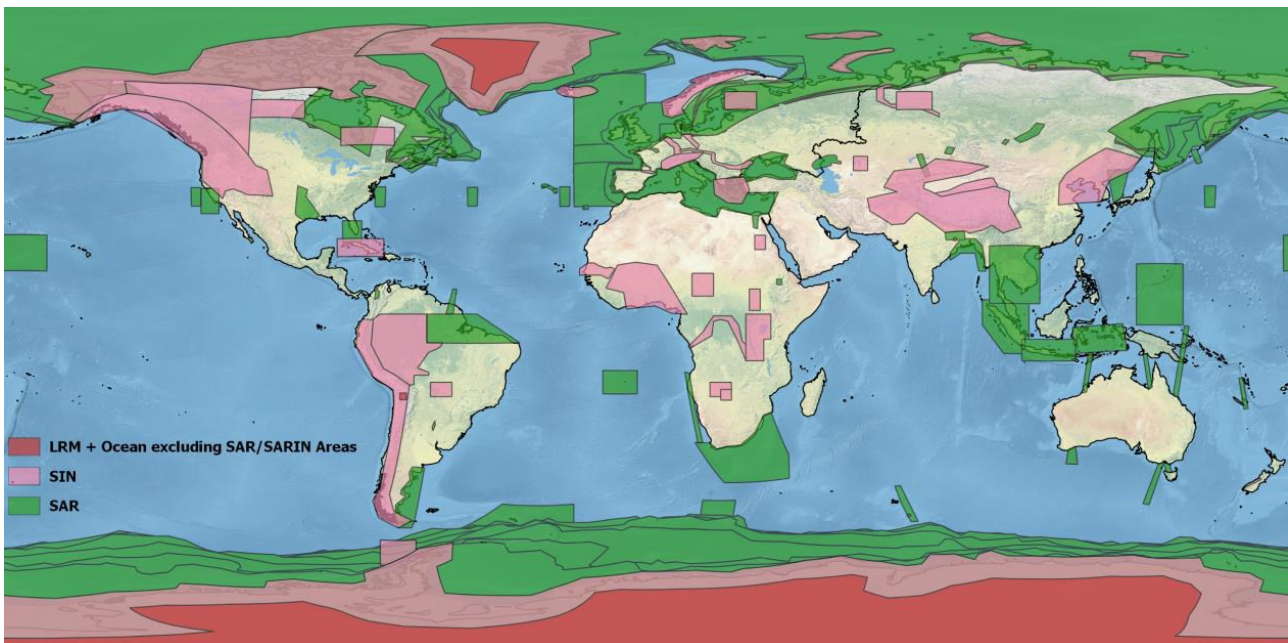

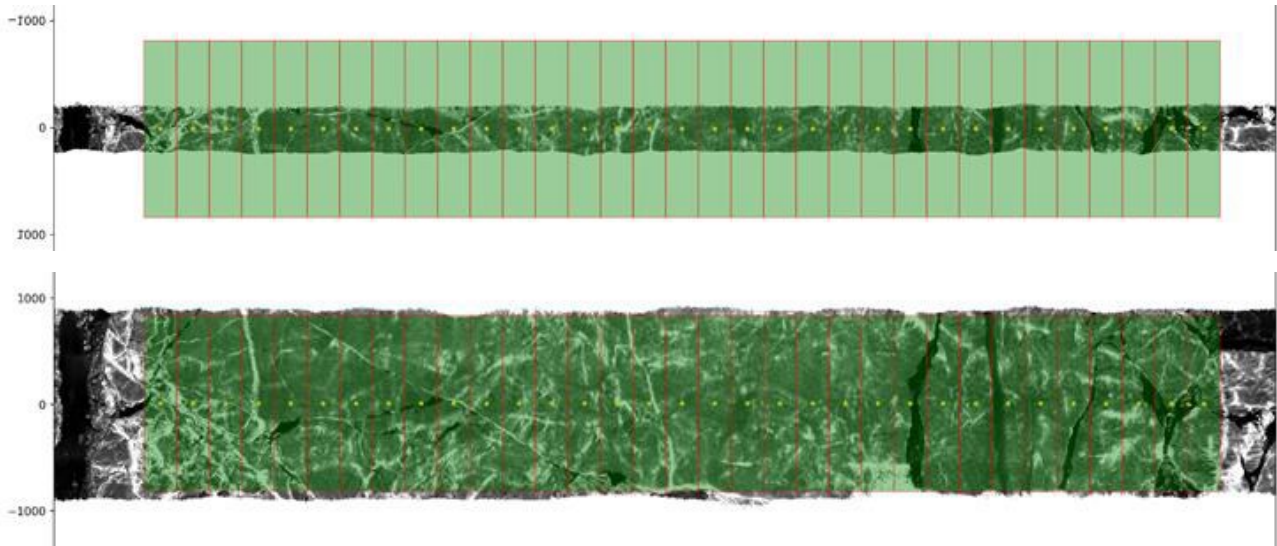**Figure 6.1: CryoSat-2 mode mask version 4.0.**

Figure 6.2: Along-track ALS surface topography with overlapping CS-2 SAR footprints. Upper plot shows ALS swath for 1 track and lower plot shows ALS surface for 5 parallel tracks covering the full width of the across-track CS-2 SAR footprints.
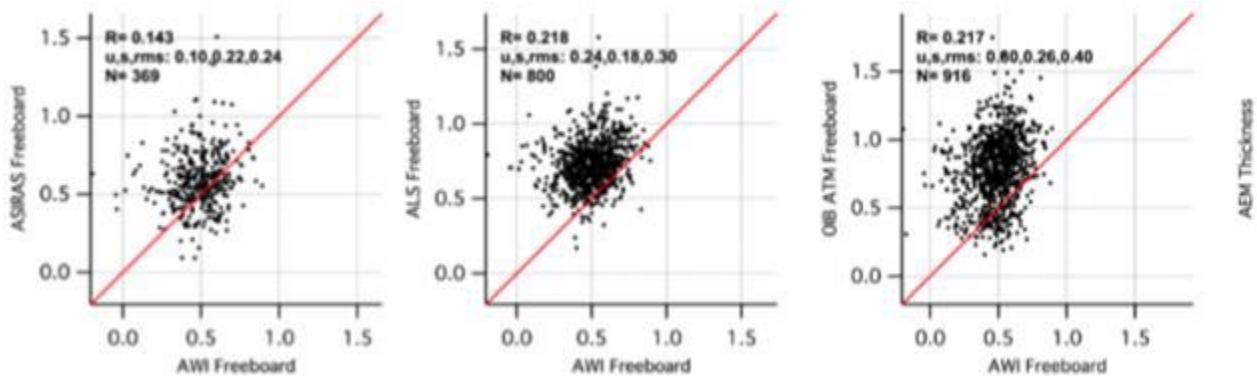
Figure 6.3: "Gun-shot" scatter plots for airborne freeboards form different sensors (left: ASIRAS, middle: ALS, right: OIB ATM) versus CryoSat-2 freeboards using AWI processing. The airborne data has been averaged over 1 CryoSat-2 footprint area as shown in §5.2.

The in-situ validation data that have been identified as the more efficient for CryoSat-2 and that are still available after 2016 are OIB, BGEP and CanCoast (see Figure 6.4 and Figure 6.5). We will make the same comparisons, over the same periods, for CryoSat-2 and Sentinel-3A on one hand and Sentinel-3B on the other hand. The interest of CanCoast is that it provides both the sea ice thickness and the snow depth. An example of comparison of radar freeboard and CanCoast data is shown Figure 6.5.
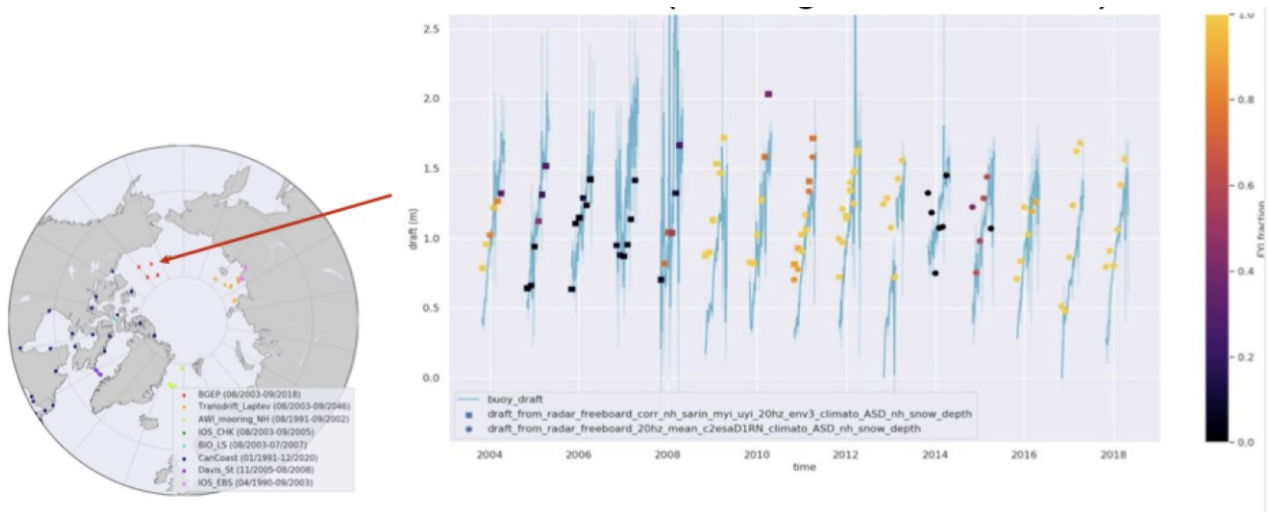
Figure 6.4: Example of validation of CryoSat-2 and Envisat altimetric freeboard against sea ice draft from BGEP mooring A. In order to be able to make this comparison, the radar freeboards have been converted to sea ice draft using a snow depth climatology elaborated from Ka/Ku altimetric measurements [Garnier et al. 2021 [RD27]]. We can observe on the map the 4 BGEP moorings in red and the CanCoast stations in blue in the Canadian Archipelago.
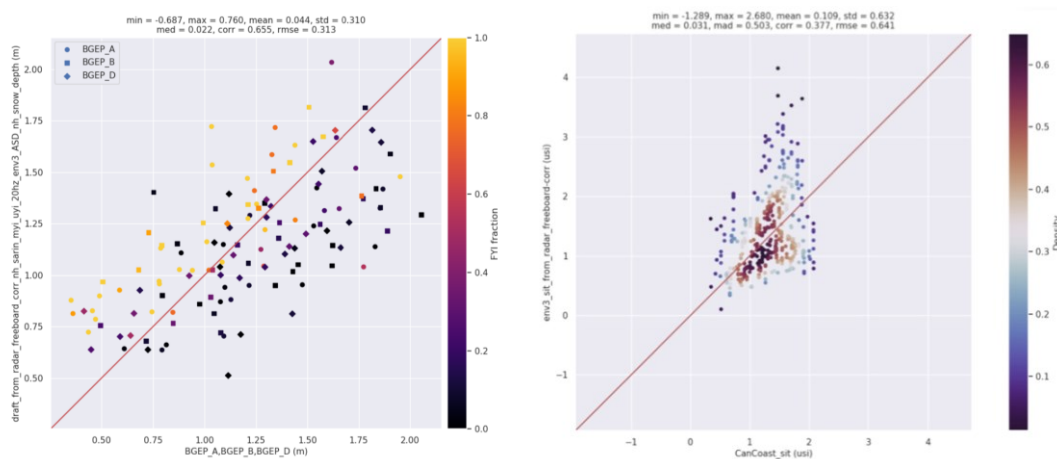
Figure 6.5: Left: Another example of comparison of radar freeboard measurements against BGEP sea ice draft. The colour indicates the type of ice: yellow corresponds to 100% of first year ice. We can observe that the FYI freeboards tend to be overestimated by the altimeter whereas the MYI tend to be underestimated relative to BGEP. This phenomenon probably comes from the snow uncertainties. Right: comparison of altimetry measurements against CanCoast handmade measurements.

6.2 Comparison with other satellites

We can also compare Sentinel3 A&B directly against CryoSat-2 as it has been done previously on older S3 products as illustrated Figure 6.6. S3A and S3B will be also compared with each other to check for their coherency. For all these comparisons the along-track data will be gridded in monthly maps in order to abstract from the different orbits. The grid that we recommend is the EASE-2 grid format suggested by NSIDC, which is a Lambert Azimuthal Equal-Area (LAEA) projection. In contrast to the polar stereo projection, this projection offers square pixels with a constant area, which is particularly suitable for statistical analysis.

However, these comparisons are currently limited by the fact that the SAR processing applied to S3A and S3B data is not adapted to the observation of pack ice. It is indeed necessary to apply a zero-padding and a hamming for the height measurement on the very specular leads (see figure 6.6). In the framework of the S3MPC LAND project, new thematic products are being developed, including a Sea Ice product whose Pilot version shows good coherence with the Ice product of CryoSat-2. It will therefore be necessary to take care in the future to use the most suitable products for the surface considered. This is also the case for CryoSat-2, which is undergoing new thematic developments within the CryoTEMPO ESA project (http://cryosat.mssl.ucl.ac.uk/tempo/), in particular significant changes concerning the ice pack. We can also focus on other projects such as FDR4ALT ESA project (https://www.fdr4alt.org), which seeks to develop thematic series homogeneous between different altimeters, in this case CryoSat-2, Envisat and ERS-1&2. It would be interesting to see to what extent these series can be reinforced by Sentinel-3A&B measurements.
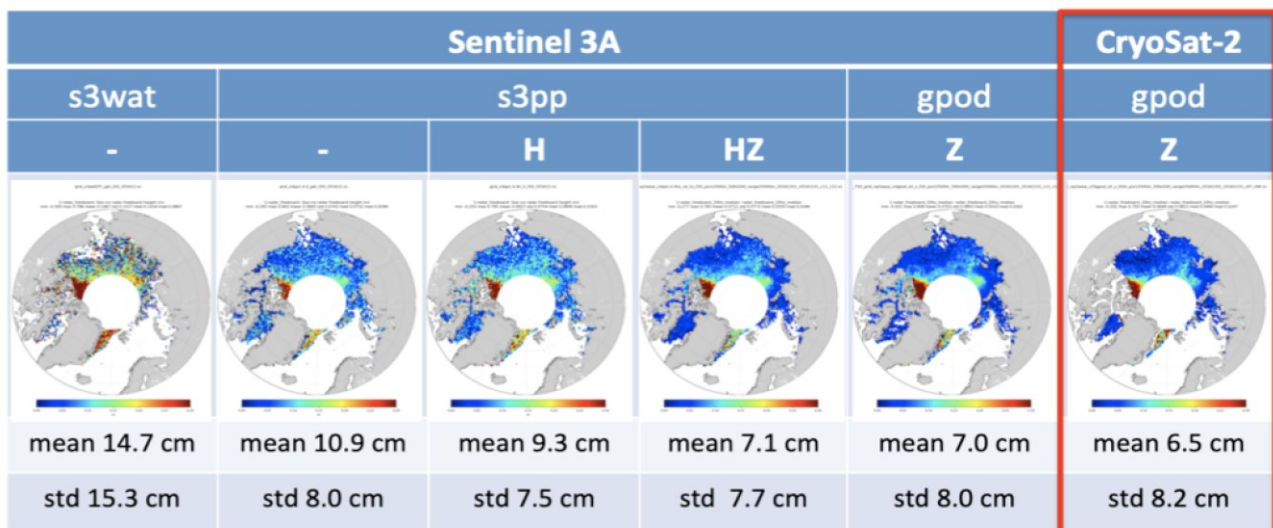
Figure 6.6: Example of comparisons between several sentinel-3A WAT freeboard products and one CryoSat-2 freeboard product (last column in the right). In the context of this project, we will consider the latest S3A LAN products.

A thorough review of penetration depth, reduction of the speed of light in the snow media and other related learnings from CryoSat-2 Cal/Val efforts, as well as new methods available from the highly detailed information from ICESat-2 (e.g. Farrell et al. 2020 [RD21]) to support S3 dependencies on surface roughness and Cal/Val of auxiliary snow depths from a combination of ICESat-2 and CryoSat-2 (Kwok et al. 2020 [RD58]) will be included in later versions of this deliverable. We will also elaborate on sample strategies.

6.3 Using the same validation data for multiple satellites

Finally, comparisons between S3 and validation data, and comparisons with other satellites to the same validation data, whether provided along-track or gridded, can be extremely useful to identify whether observed differences are unique to an individual satellite (which would suggest that they are highlighting potential issues with that satellite's processing), or common to multiple satellites (which would suggest an issue either with the validation data or with the comparison process. This work will be considered in later phases of this project.

7 FRM Protocols and Procedures

As seen from the list of Cal/Val observations in Section 5.3, there are many different sensors and platforms, each observing different sea ice parameters with its own pros and cons and associated uncertainties and errors. Here we look deeper into the different Cal/Val observations, potential test sites, and potential FRM sensors for the validation of the S3 STM sea ice geophysical parameters to define best protocols and procedures for future FRMs. We also consider, in Section 0 and 7.5 how we may approach uncertainty analysis for TDPs and FRMs to meet the QA4EO requirements, as described in Section 1.3.

7.1 Calibration site selection

When selecting a calibration site or sites, several things need to be considered:

- The temporal sampling (e.g., at a specific season, continuously, …)
- What type of measurement and platform to be used?
- The distance to the sea ice
- Specificities of sea ice conditions (e.g., type of ice, type of snow, sea ice drift, density, roughness, etc.)
- Size, Capacity & Restrictions (military station, weather station, temporary site, access to fuel, …)
- Weather and temperatures at the site, e.g., if the measurements are temperature dependent, but also to capture different penetration
- Daylight hours
- Other needs, e.g., navigation and positioning

It is important to select sites of different sea ice conditions and types to evaluate the in-situ performances in various sea ice conditions. It is also important to be covering continuously over time to capture seasonal changes in sea ice and snow conditions.

7.1.1 FRM validation sites and best practices

It is important to consider what is meant by a 'permanent' station when it comes to sea ice. One would consider a permanent station as a station that is always located in the same place, measuring the same type of observations over the same area- or surface-type, and would therefore be a 'reference point' throughout the period of validity of the instrument. However, when measuring sea ice, this assumption of a permanent station is not valid. Due to the dynamic, deformative and drifting nature of sea ice, one could consider two types of deployments as permanent:

- A permanent latitude/longitude position, or
- A permanent ice floe position.

A permanent latitude/longitude position (1) could be a moored upward looking sonar (ULS), such as those deployed by BGEP, NPEO, NPI etc. These observations are anchored to the bottom of the sea floor, and measures at a specific interval the profile of the surface above - either all the way to the water surface in case no ice floes travel across the profiling path, or to the bottom of the ice, i.e., the draft, of the sea ice that travels across the path of the profiler. As such, one could consider this to be a permanent station since it is permanently located in the same spot - however, the draft observations of the ice floes that are recorded are not permanently located in the same spot. The draft observations are instead observations of several types of ice floes - level ice, deformed ice, thin ice, thick ice - drifting across the path of the profiler. Therefore, while the position of the profiler is permanent, it is not the same surface that it measures throughout the validity of the instrument - it is the sea ice draft of various floes. And, if one were to compare monthly draft observations, it would be an average of various floes that have been in the vicinity of the profiler and travelled across its path that is reflected here - but it is not the same floe that is measured throughout the period of measurements.

Campaigns include airborne, shipborne and in situ data collected - either in collaboration with each other (achieving multiple observations from several types of platforms) or entirely shipborne, airborne or in situ. When considering this, procedures are likely quite different because there is a difference between acquiring data from ground, ship, and air.

7.1.2 Long-term

Permanent and semi-permanent solutions often acquire data during several months to years of the area, providing data over a large temporal scope. However, the data are rarely regionally representative, unless a large network of stations are deployed. Thus, the data are limited in their representativeness. Deployment procedures of permanent (e.g. ULS) and semi-permanent (e.g. IMB buoys) instruments may differ depending on the organisation/group that deploys them, area of which they are expected to be deployed in, and of course whether they are permanent or semi-permanent. Furthermore, the most important factors include the condition of the sea ice, the surrounding conditions and potential hazards or dangers (e.g., nearby polar bears, strong winds/currents, etc.).

- **Permanent solutions**
  For sea ice, permanent solutions for long-term monitoring of FRM validation sites are challenging due to the movement of the sea ice and the only options are moorings measuring the draft of the sea ice, and not directly the sea ice freeboard, nor the snow. Data from moorings usually have a long latency time (~1-2 years), i.e. from the time of observation to the processed data is available to the user, as they need to be physically downloaded by recovery of the buoys, which is typically done once a year. These operations are cost-expensive and post-processing is tedious.

- **Semi-permanent solutions**
  Drifting buoys are placed on an ice floe and stay until the ice floe melts or deteriorates or the power supply (batteries in combination with solar panels) dies. Thus, the life-time depends on the location of the buoy and time of deployment, but typically lasts a few months to a few years. Today, the only solutions for data transmission are by Iridium link, but future solutions are currently explored by e.g. nanosatellite constellations. To secure a certain level of life-span of the sensor, these are usually deployed on thicker ice at a certain stage of development. Another hazard for such stations is ice ridging and curious polar bears damaging the buoys. These are potential risks but rare.

7.1.3 Short-term - Campaigns

Campaigns are expensive, and thus often only carried out once or twice a year. Due to this limitation, the temporal scope of the (especially airborne) campaigns are often limited to the same time of year - around spring or end of summer - to investigate a particular season of the sea ice. This is mostly constrained by logistics, expenses, and weather and sea ice conditions. As a consequence, the interannual variability of the sea ice is rarely captured during weekly-to-monthly campaigns, suggesting that the campaigns are only representative for a short period of time. However, compared to the semi-permanent/permanent stations, they often survey a much larger area (several hundred kilometres, compared to a point measurement). This is applicable for both submarine, ship and airborne campaigns. Furthermore, for the case of airborne campaigns, the observations acquired by the airborne instruments are similar to the satellite observations (radar or laser altimetry), which means that they may be more representative of what the satellite observes.

Airborne campaigns (fixed-winged aircraft and helicopters) are cost-expensive and tend to represent the same season, as the airborne campaigns are often based on aviation regulation of visual flight rules (VFR) during survey flights, limiting these outside the Arctic darkness (mid-October-February). As current radar altimeter measurements are related with huge errors outside the winter season (May-September), the window is very narrow.

High Arctic airborne campaigns are restricted in terms of requirements to large payloads, long endurance at low altitudes, and the ability to mount large arrays for securing the radars and ensuring that especially challenging targets could be surveyed as well. Antarctic operations often require very long-range aircrafts based off-continent while also being capable of efficient high-altitude transits across the Southern Ocean, or a Short Takeoff and Landing aircraft based from austere on-continent facilities. Longer aircraft with longer ranges often required a larger number of personnel to meet crew duty rules and to maximize scientific productivity. Thus, all these requirements had to be balanced out according to cost and benefit. Deploying larger aircraft however was particularly important for surveying the most remote science targets at both poles (MacGregor et al., 2021 [RD70]).

Helicopters are in general more expensive per hourly rate and in fuel consumption than smaller ski-equipped aircrafts such as De Havilland Twin Otters. For ground work and testing of systems, which are optimized by being collocated, the

aircraft solutions are preferred, as it has longer endurance and can carry a larger payload. However, with the rapidly changing sea ice conditions, sea ice landings using fixed winged aircrafts are becoming a high-risk business and demand an on-site backup aircraft for safety reasons.

Drones have huge potential, and if proven to work in Arctic conditions, small octo-copter drones as described in WP 2.3.2, are easy to deploy. Because of the slower speed and the need for a certified drone pilot, the costs are not negligible. However, drones would be a nice supplement to airborne campaigns by providing detailed regional studies which can be obtained repeatedly over the season. Thus, drones could potentially fill the gap between the semi-permanent solutions and campaigns.

Submarine and ship cruises are very cost-expensive and especially for ship cruises tend to underestimate the sea ice thickness as the ships usually choose their route in areas with thin ice. Submarine cruises are related with large uncertainties both in the draft, as it is dependent on leads and depth of the submarine, but also the geo-location. Other techniques such as AUV's need further development, as current versions are relatively heavy and so far need tethering not to get lost.

In situ campaigns or as an example: MOSAiC was a massive undertaking that required tremendous work regarding the logistics and implementation of such a network of various on-ice sites, especially since many observations were expected to be acquired during the year-long expedition. The expedition was divided into 6 legs, and during 4 out of 6 legs Polarstern needed to be refueled/deployers needed to be taken home, which required the presence of a second icebreaker. That, along with all the logistics and planning that had to go into the every-day work of each leg to acquire the observations, change personnel, ensure safety and security in such a hostile environment etc., shows how planning and executing such campaigns is a lot of work.

Temporary ice camps These are related to large risks with the shrinking ice cover, and or landings by helicopter or ski-equipped fixed winged aircrafts.

7.1.4 Potential calibration sites

Here we discuss potential validation sites, and associated requirements for FRM sensor deployment.

7.1.4.1 Northern hemisphere

One of the biggest challenges with respect to validation of S3 in the Arctic is the relatively low turnaround latitude (81.5N/S) marked by blue circle in Figure 7.1a, and sites often used for airborne campaigns reaching far into the Arctic Ocean are deemed useless, this yields e.g., Station Nord (NE-Greenland), CFS Alert (NE-Canada) and Eureka (NE-Canada). Other options for reaching far into the Arctic are very cost-expensive and logistically challenging, e.g., site options 1 and 2 in Figure 7.1a.
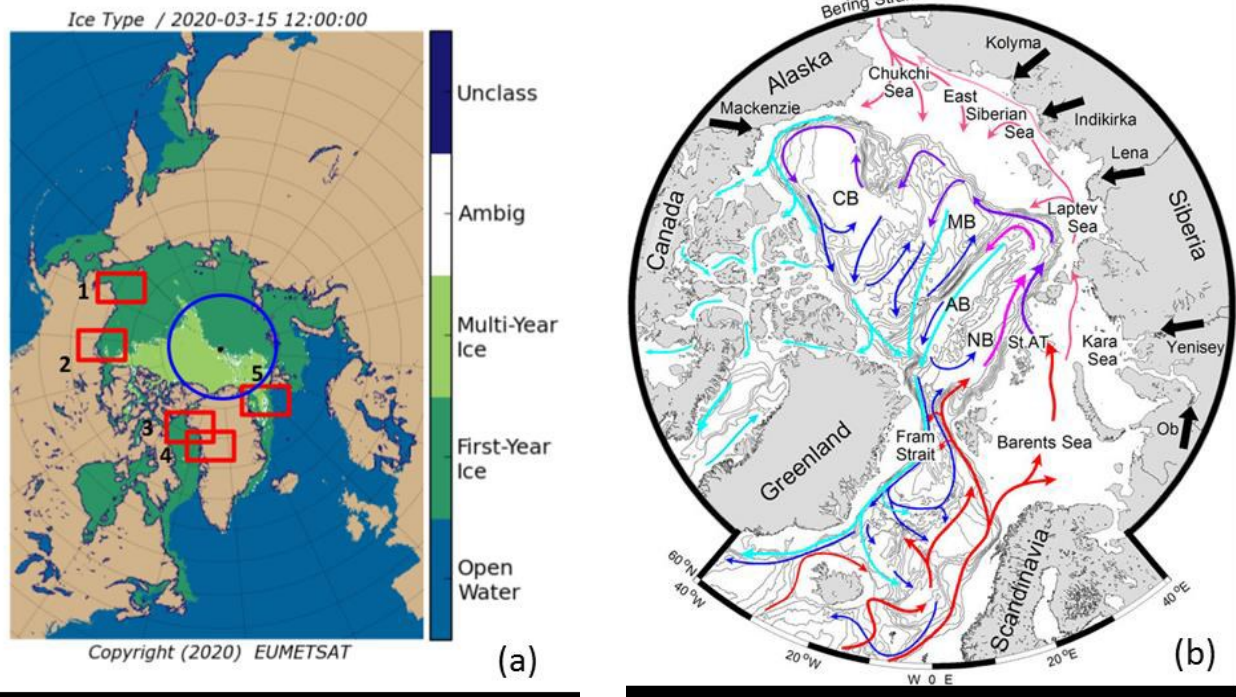
Figure 7.1: (a) Sea ice types from OSI-SAF, overlaid with potential validations sites marked 1-5 (red boxes) and polar gap (blue circle). (b) Main currents in the Arctic from Polar Research 2015, 34, 6891, http://dx.doi.org/10.3402/polar.v34.26891

The most optimal validation site would be the Beaufort Gyre, especially for semi-permanent solutions, as these would tend to stay for a while due to the clockwise circulation of the Beaufort Gyre. For buoy deployment by aircraft or helicopter, such operations could be performed from Inuvik (Canada) or Barrow or Prudhoe Bay (Alaska). Alternative solutions are Baffin Bay based either out of Thule AB (area 3) or Upernavik (area 4). Thule AB is located further from the Baffin Bay, and helicopter operations need refueling in Sassisivik. Also access to Thule AB requires lots of certification and airports are closed during weekends with no option of openings. The Upernavik option provides direct access to the sea ice in Baffin Bay and in Greenland, and it is possible to request openings and/or extension outside of the airport opening hours for a reasonable fee. Other options would be the Fram Strait, but this area is far from optimal as the sea ice is drifting very rapidly through the Fram Strait.

Only options 2 and 5 include areas covered by multi-year ice, as these areas are limited due to the polar gap.

Size, Capacity & Restrictions:

Potential **Community based** drone sites;

- Utqiagvik/Barrow 5000 (Alaska)
- Sachs Harbour 100 (Canada)
- Savissivik 55 (Greenland)
- Kullorsuaq 450 (Greenland)
- Upernavik 1000 (Greenland)

Inuvik is located too far from the sea ice for direct drone operations, and would need helicopters or fixed winged aircraft with the capacity to land on sea ice. Alternatively, these operations could also be ship based, i.e., from cruises in the Arctic ocean.

Central Arctic observation from deployment of buoys and/or ship-based observations:

Deployments of drifting buoys at the north pole might not be the most optimal solution for S3 validation, as this area is within the S3 polar gap. The dominating current in this area is the transpolar drift, which tends to transport the buoys towards the Fram Strait which is one of the more difficult areas, due to high drift speeds resulting in large dynamics, see Figure 7.2 as an example of drifting buoys deployed at the north pole and the tracks. The most optimal solution would be to deploy drifting buoys in the Beaufort Gyre, which tend to keep it for a longer time within S3 coverage. However, this said, an area like the Fram Strait should also somehow be validated as it is the area with the largest transport of sea ice fresh-water out of the Arctic.
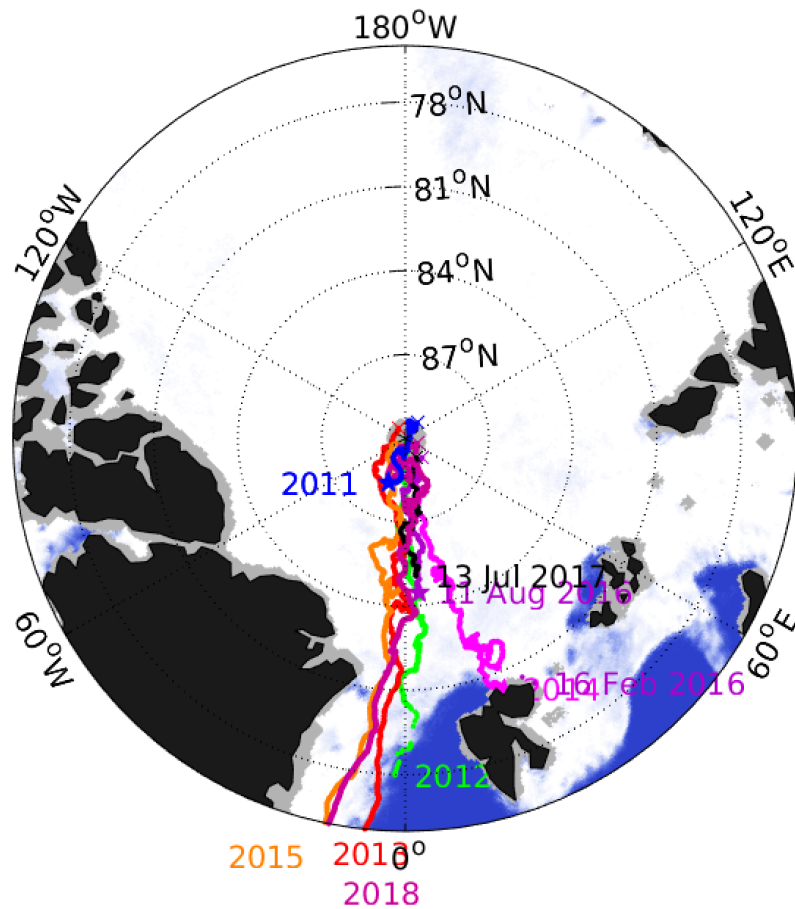

Figure 7.2: Trajectory of Ice-T buoys deployed each April at the North Pole since 2011.

Weather, temperatures and daylight hours:

Weather, temperature and daylight hours might be necessary to take into account when selecting calibration site/sites, depending on the operations and of the instruments, e.g., whether the instruments are temperature dependent, or we need daylight for the operations, e.g., for helicopter operations with landings on sea ice cold conditions with rather thick sea ice (>50 cm) are needed for the safety of operations. Also, enough day-light hours are needed for operations (in the order of minimum 10 hours). For temperatures below -50 °C it is difficult to do any research, as instruments and potential cables are difficult to handle. Battery-driven drones can be impacted by having shorter operation periods in cold conditions, or even have a lower limit for operations. Also radar altimetry is dependent on cold snow for the assumption of penetration to the snow/ice interface to be valid. Thus, temperature records for the calibration site and night/day distributions can be necessary to study and include in the selection of the site/sites, see examples in Figure 7.3. For high Arctic >80°N, operations relying on daylight (including airborne and helicopters) are limited to the time period mid-March to mid-September. For operations in the Beaufort Gyre, (at latitudes <80°N and >69°N) the time period is extended to begin by the end of February to mid-October.
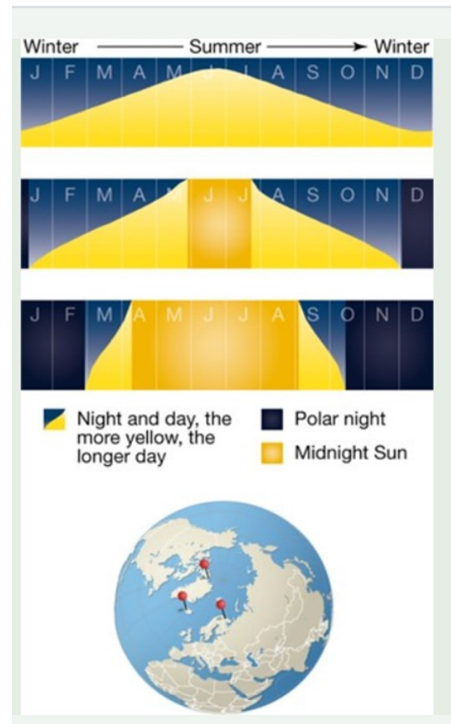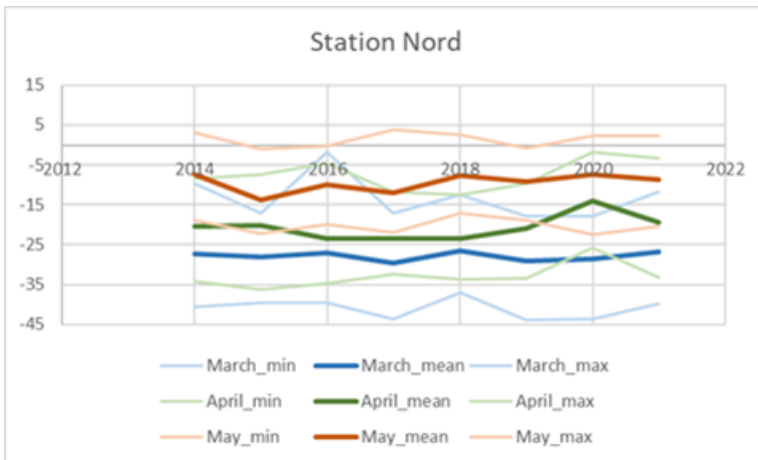
Figure 7.3: Station Nord temperature records from the most recent 10 years (left), source Danish Meteorological Institute https://www.dmi.dk/vejrarkiv. Illustration of daylight variation at 3 different locations in the Arctic, i.e. Akureyri, Iceland (upper right), Murmansk, Siberia (middle right) and CFS Alert, Canada (lower right). Only the northernmost sites have polar night and midnight sun. Credit: Hugo Ahlenius, UNEP/GRID-Arendal, https://www.grida.no/resources/7153

Navigation and positioning:

It is not only the S3 polar gap, which causes challenges in the high Arctic. Lots of drones use GPS to navigate by, which is dependent on communication with satellites. According to Ader and Axelsson (2017) [RD4], the GPS signal should function better in Northern locations since satellites are more frequent there than in other locations. However, as stated by Vesterhauge (2021) [RD108], the orbit of GPS satellites does not cover the Arctic fully - the GPS receiver will only see the satellites in the horizon, which results in insufficient accuracy. To work around this issue, a possibility of utilising a stationary reference point (a ground station) can provide accuracy an order of magnitude better than satellite-based only (Vesterhauge, 2021 [RD108]).

However, not only the GPS positioning proves difficult in Arctic environments. Magnetic compasses are also used to navigate by, however since the magnetic compasses base their directions on their position relative to the magnetic poles, when operating near the poles, the indicated direction becomes less reliable (Ador and Axelsson, 2017 [RD4]). The magnetic interference near the poles can also limit the accuracy of the yaw heading of multi-rotor drones (Vesterhauge, 2021 [RD108]). In particular, the area of the Baffin Bay in the Arctic is near the outermost warning zone (light grey), shown in Figure 7.4, which increases the possibility of navigational issues. However, that area is still not as affected as for example near Station Nord (81°43'N, 17°47'W) where DTU Space once flew a drone that was unable to maintain its position due to unfavourable GNSS and magnetic interference conditions.

Figure 7.4: World Magnetic Model, Main Field Declination. The two ellipses show the most critical areas where potential navigational issues might occur.

7.1.4.2 Southern hemisphere

In the roadmap for sea ice [TD-6-2], we will also look into FRM options for the Southern hemisphere. These might introduce different aspects of procedures and best practices, when compared to the Northern hemisphere, as the sea ice and snow conditions are considerably different from the Arctic. In addition, logistics, access, certifications and costs are different from the Arctic.

7.2   Potential FRM sensors for S3 LAND STM L2 product validation

How do we select a suitable FRM sensor for S3 land STM L2 Sea Ice product validation? First, we cannot fully validate the S3 land STM L2 sea ice product by using a single FRM sensor, as there are several parameters involved with each contributing with their own error budget and representativeness, as described in Chapter 2. We need a suite of sensors to make a full validation, as illustrated in Figure 7.5. We need to consider different aspects to select the most suitable FRMs as listed below:

1. Select FRMs to cover all S3 sea ice geophysical parameters
2. Secure temporal as well as regional coverage, e.g. campaign vs semi-permanent
3. Make strategies of comparing different parameters (Inter-comparability/representativeness)
4. Make strategies for different scales, e.g. footprint/resolution when comparing in situ, airborne, shipborne data to satellite scales
5. Fully describe uncertainty estimates, error propagation and SI-traceability
6. Real-time availability
7. Sea ice drift
8. Costs/deployment procedures

The dependencies of FRM measurand and what type of sensor to select and which platform to be used, can be aided by use of the comparison diagram Figure 3.1, and the Sankey diagram Figure 5.1.
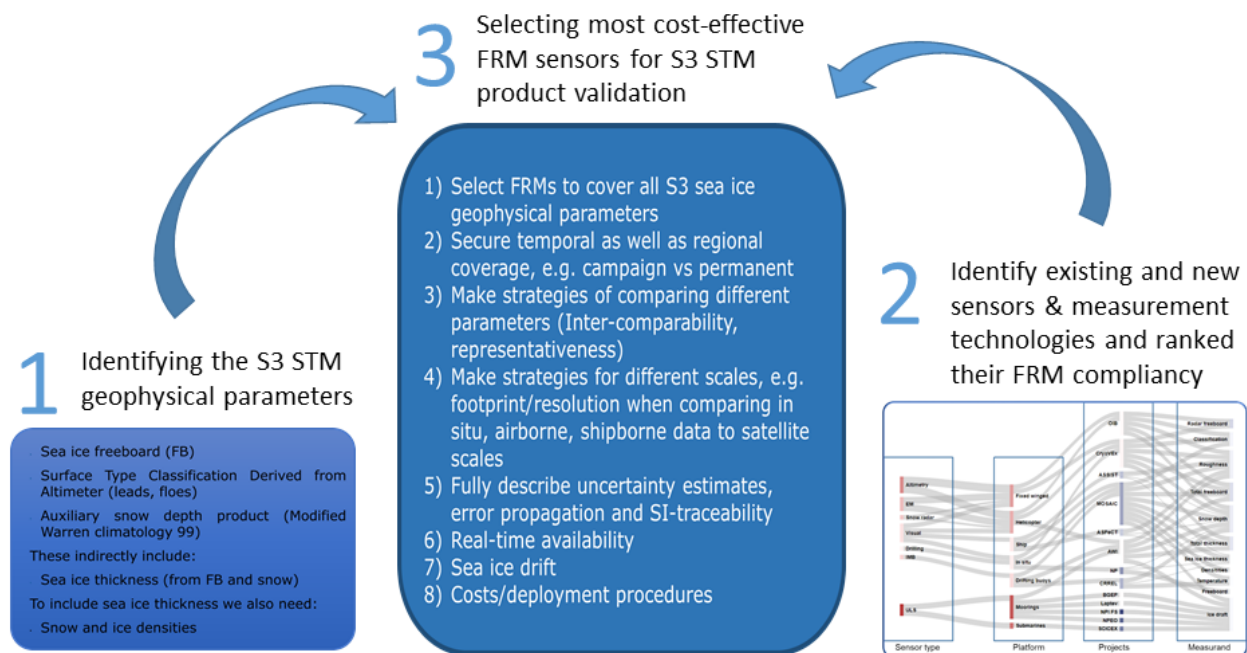
Figure 7.5: Illustration of the procedures for selecting the most cost-effective FRM for the provision of S3 STM L2 product validation. 1) S3 STM Sea ice geophysical parameters, as identified in Chapter 2, and 2) the FRM measurands based on the literature review of existing and new sensors as described in Chapter 5, together with 3) the identified steps needed in order to perform full S3 validation strategy.

A visualisation of the independent platforms (e.g. satellite, airborne, submarine, buoys, drone, in situ) and their dependencies on uncertainty, spatial coverage/representativeness and temporal coverage is shown in Figure 7.6. Here is also provided the type of measurand (i.e. draft, radar freeboard, total freeboard, sea ice thickness, snow depth, roughness) by symbols observed by each platform. Such illustrations can aid the selection of FRMs for S3 validation. Related uncertainties of independent measurands of existing validation data, has been produced within the ESA CCI+ Sea ice project and can be found in Table 5.1.

To test the FRM compliancy for each single sensor (included in the literature review in Chapter 5), we have defined several categories, as listed below, and described each sensor according to the categories in a FRM compliancy matrix. The FRM compliancy matrix is delivered as a separate excel-file [TD-2-FRMCompliancyMatrix]. Each of the categories above is not equally important for testing the sensor for FRM compliancy.

Sensor:

- Sensor type
- Sensor
- Instrument ID
- Manufacturer (not in the ranking)
- Functionality
- Frequency
- Maximum range
- Platform (i.e. buoy, airborne, mooring, …)
- Measurand
- Projects or campaigns
- Range resolution
- Horizontal resolution
- Sampling rate
- Temporal coverage
- Spatial coverage
- Uncertainties of the measurand
- Traceability of the measurand
- Bias of measurand
- Reliability of the measurand
- Lifetime of the sensor
- Stability (e.g. temperature dependencies …)
- Calibration
- Technology Readiness Level (TRL)
- Scientific Readiness Level (SRL)
- Data collection
- Latency time (time of measurement to data availability in FRM)

Costs:

- Sensor purchase
- Yearly maintenance
- Deployment method
- Deployment cost

To test all the sensor types listed in the FRM compliancy matrix [TD-2-FRMCompliancyMatrix] for their ability to act as S3 operational FRM provision, the Appendix A evaluates the sensors based on the following characteristics:

1. Sensor
2. Platform
3. Measurand
4. Accuracy/uncertainty level of Measurand
5. Representativeness of the measurand - how representative is the measurand of the sensor to the S3 TDP
6. Traceability of uncertainty of Measurand
7. Technical Readiness Level (TRL)
8. Scientific Readiness Level (SRL) - this includes algorithm development
9. Latency time: those with high scores have the lowest latency time
10. Costs - based on an overall cost-effect
11. Rank - see definition below.

Where 1-3 are basic descriptions of the sensors, 4 has been quantified, whereas 5-10 have been assigned a scoring (similar to those defined in [TD-1] and listed below in the "Legend of the scoring") according to the sensor type compatibility for S3 operational FRM provision. The overall ranking (11) is described below in the list of "Ranking". 4-6 are the most important categories for the overall ranking, whereas 7-10 are less important. The selected categories (4-

10) are listed in decreasing order w.r.t. importance. As an example, all measurements in the polar regions are relatively cost-expensive, and of lower importance then e.g. the representativeness or traceability.

Legend of the scoring:

- '++' = excellent
- '+' = good
- '-' = not good
- '--' = bad

The overall ranking of sensor FRM compliancy has been adapted from [TD-1], and is defined as follows:

Ranking:

- A = To be preferred for operational FRM provision ('A+' identify the sensor with the best ranking)
- Ax = Similar to A, but with a low TRL or SRL, meaning that they need further R&D
- B = To be used to complement rank "A" sensors ('B+' identify the sensor with the best ranking)
- Bx = Similar to B, but with a low TRL or SRL, meaning that they need further R&D
- C = Not recommended for operational FRM provision

The ranking system shall aid the selection of the individual sensors according to FRM compliancy in benefit of the S3 STM mission. Even though we here define which sensors are FRM compliant, does not mean that other sensors/methods cannot be used as validation data. This is seen in the light of the sparsely distributed validation data in the polar regions. Sometimes observations which are not FRM compliant e.g., with relatively high uncertainty estimates, are better than nothing at all.

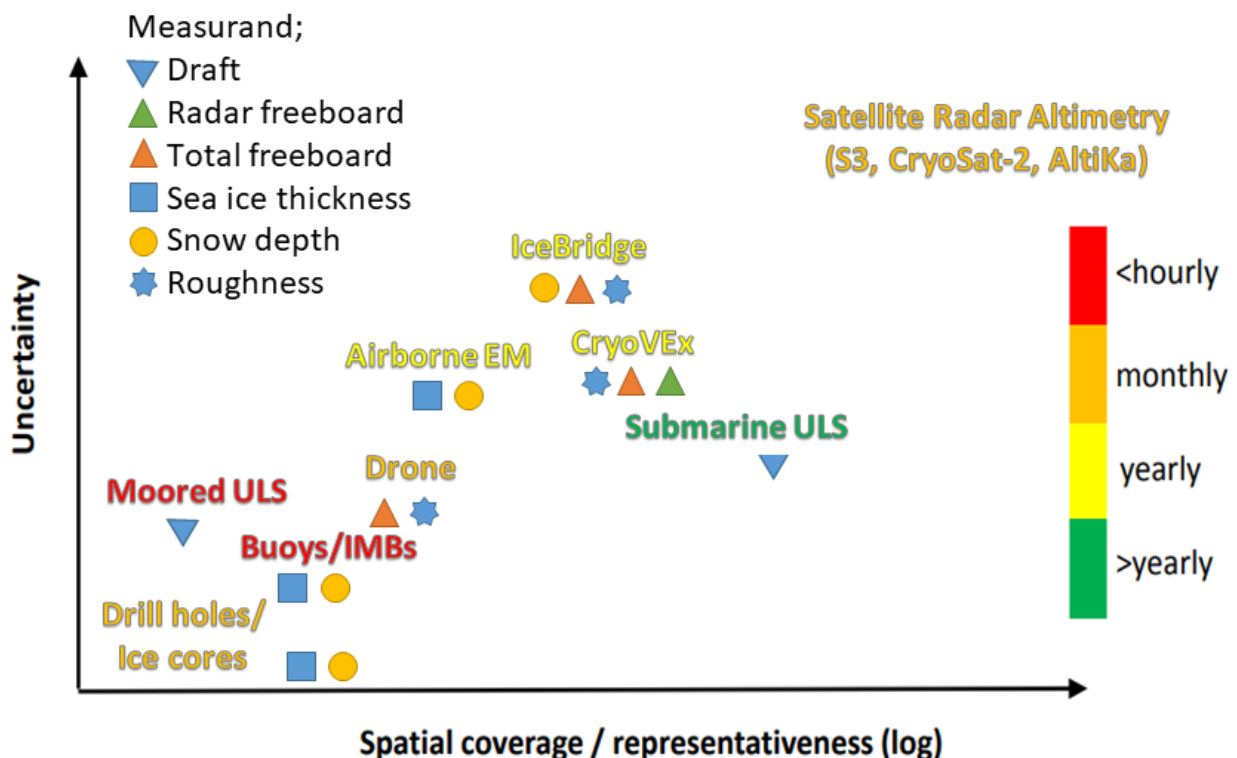**Figure 7.6: Spatial scales and uncertainties adapted from C. Haas.**

Strategies for considering the errors and uncertainty coming from the potential FRM sensor measurements when compared to the satellite measurements within a much larger footprint, but also due to the differences in measurands, e.g., when comparing sea ice thickness from S3 with draft from upward looking sonars from moorings, different

penetration depths and roughness, will be based on learnings from alternative satellite sensors, see Chapter 6. This can be done as there already exists a lot of validation work of both Sentinel-3 and similar satellite missions such as CryoSat-2 measuring with a similar sensor over sea ice as S3. Usually much larger sampling, i.e., averaging, of both measurand of the validation data and satellite observation needs to be performed to get higher correlation, see Chapter 6.

The most optimal solution for S3 LAND STM L2 sea ice product validation would be coincident measurements of sea ice freeboard, snow depth and ice thickness, as well as sea ice and snow densities. It is difficult to find a stand-alone solution for such observations over the full sea ice season, and we will investigate combinations of different sensors and platforms to meet these requirements. A combination of airborne measurements of sea ice freeboards from radars and high-resolution lidar would provide information of penetration depths as well as sea surface classification and surface roughness. However, airborne campaigns are cost-expensive and constrained to either September/October or March/April. An option to get repeat observations of sea ice freeboard on local scales would be the use of drones. We will investigate the option of a light-weighted drone equipped with lidar and camera to obtain sea ice freeboard and surface classification. Both the airborne and drone sensors need further information of snow depth, which we suggest to be done by deployment of Ice-T buoys. We will further discuss ground sampling strategy, sensor stability over time, quality assessment and SI traceability for each sensor type.

Final recommendations for future S3 sea ice FRMs will be based on the ranking of the compliancy matrix, the literature review of existing sensors (Chapter 5), learnings from alternative satellite sensors (Chapter 6) and learnings from the ESA st3TART Arctic sea ice campaign in spring 2022 and is provided in the roadmap [TD-6-2].

7.3 Metrological approach to uncertainties

FRMs, as described in section 1.3, are non-satellite observations that meet the standards of QA4EO and which are helpful to the calibration and validation of satellite observations. For FRMs to meet the standards of QA4EO, they need to have traceability to a community-agreed reference (preferably SI) and have an associated quality metric (preferably a robust uncertainty budget). Several different projects have applied these principles to a wide range of satellite and non-satellite observations, and from those projects, guidelines have been established that are documented on the QA4EO website (www.qa4eo.org).

These guidelines set out 5 steps to an uncertainty budget, which are discussed in the subsections below. In this project we have begun applying these steps to some example FRMs, and one example is given in Section 7.5.1.

7.3.1 Step 1: Define the measurand and the measurement model

Defining exactly what is being measured and provided in a data set is often more difficult than it first appears. Even for an in-situ observation, the reading on the instrument (e.g., a temperature) may be different depending on how the measurement is made, i.e., on its input quantities (e.g., through a radiance measurement, or the expansion of mercury or the resistance of a thermocouple). And beyond that, the measurand of interest may be in how that reading relates to the estimate of the underlying physical phenomenon (e.g., air temperature near surface), or some representative phenomena (e.g., average air temperature in a grid cell of a model). Similarly, for a satellite observation, the measured signal, often in 'counts' needs to be converted to a physical quantity (e.g., top-of-atmosphere radiance within a spectral band). Processes such as orthorectification alter the perception of the measurand. Is an observation representing an average value within a pixel, or a peak value within a footprint? When satellite and in situ data are compared, they are likely to measure different things. For example, satellite-based measurements may relate to sea surface temperature as the top micron of the water, measured over a satellite footprint, whereas in-situ measurements may relate to sea surface temperature at a single point at a depth of a few tens of centimetres.

Furthermore, there may be questions of reference – is a range measured relative to the Earth's ellipsoid or to its geoid, for example. At higher levels of processing, where measured values are combined with models, the measurand may be even more difficult to define. However, defining the measurand is important both to describe the dataset to users and to enable clear thinking in the uncertainty budget. Sometimes, it is necessary to do separate uncertainty analysis for different linked measurands and propagate uncertainty between these steps (e.g., the uncertainty associated with the point temperature, the uncertainty associated with the average spatial cell temperature assumed from that point, and the uncertainty associated with comparing the in-situ temperature to the satellite temperature all require separate analysis).

The measurement model itself may be able to be written as an equation with an analytical function. Or it may only be defined through code, particularly if iterative processes, non-linear fitting, or machine learning techniques are part of the processing. Whether or not it can be written as an equation, the processes by which input quantities are combined to determine the measurand, is known as the measurement model. It is important to realise that there will be uncertainties associated with the form of the measurement model (whether the process it describes accurately describes reality) as well as with the input quantities that are used within it.

7.3.2 Step 2: Establish traceability with a diagram

A visual representation of how a measurement and its traceability is achieved, along with visually representing the different sources of uncertainty, are highly valuable in assessing performance. Diagrams are extremely useful mind mapping tools to help understand and communicate how a measurand is derived and to consider and share what the sources of uncertainty are. Diagrams show where terms come from and thus highlight sources of uncertainty in input quantities and in the approximations and assumptions inherent in the model.

There are different types of diagrams that can be helpful for different purposes. In this project we use a combination of uncertainty tree diagrams and more traditional processing diagrams, as well as a new concept of a comparison diagram.

7.3.3   Step 3: Evaluate each source of uncertainty and document in an effects table

After the work in step 1 to specify the measurand, and in step 2 to identify where the input quantities of the measurement model all come from, it should be possible to get a list of sources of uncertainty (also known as effects). There are several things that need to be known about each effect and FIDUCEO and GAIA-CLIM used the concept of an 'effects table' to document, systematically, the information that needs to be known about each effect.

The exact rows of an effects table will depend on the application, but there are several common requirements. This is for each source of uncertainty to identify:

- Which quantity in the measurement model it affects?
- The magnitude of the uncertainty
- The shape of the probability distribution function for the uncertainty
- How the uncertainty associated with this effect is propagated to the measurand (the sensitivity coefficient)

The error correlation shape and scale for all 'dimensions' that are relevant both for determining the measurand and for subsequent 'higher level' processing or applications that perform averages and/or comparisons

Additionally, it is valuable to document whether the analysis in the table is mature (based on sound analysis with evidence and validated through independent comparison) or very immature (based on expert judgement) or somewhere in between.

The 'effects table' provides a common method for recording what is known about each source of uncertainty. This is valuable to think through the uncertainty analysis and for recording for long term data preservation purposes. Using effects tables that follow the documentary templates and examples given in the guidelines will lead to consistency within the community.

A core part of this methodology (central to step 3) is to consider error-correlation shape and scale in all dimensions. This requires a careful distinction between the concepts of 'uncertainty' and 'error' and an understanding of the nature of environmental observations (affected by both instrument uncertainties and natural variability) and the nature of satellite observation data processing (with different 'levels' that are often processed by different scientific communities). A full discussion of these aspects is given in the documents on the www.qa4eo.org website.

7.3.4   Step 4: Calculate the FRM and its associated uncertainty

The next step involves processing the FRM, FDR or TDP through the measurement model and determining the associated uncertainties. These uncertainties need to be propagated all the way through the entire processing chain to the measurand.

There are two ways of processing uncertainties that are described in the GUM. Uncertainties may be processed using Monte Carlo methods (as in an ensemble analysis), or through the Law of Propagation of Uncertainties (a linearized Taylor expansion often recognized as 'the square root of the sum of the squares', although when there is error correlation a full covariance matrix is needed). Monte Carlo can provide better results for non-linear models and is the often the only option where the processing cannot be written analytically (e.g., in neural networks or iterative processes), however, it is computationally expensive and does not provide easy access to the importance of different sources of uncertainty. A hybrid approach can use Monte Carlo analysis to evaluate sensitivity coefficients that are propagated through the law of propagation of uncertainties or used in look up tables.

7.3.5   Step 5: Document for different purposes

Record the information for both today's users (simplified summary information that can be readily used by others) and for the purposes of long-term data preservation (recording and documenting all the information needed for the scientific analysis to be reproducible in the future).

7.4 Metrological uncertainty analysis for sea ice TDP

To ensure a full metrological uncertainty analysis, the uncertainty traceability must be performed for both the satellite observations and for the FRMs when a comparison is done. Here, we present an example of a metrological uncertainty analysis for sea ice TDP (satellite observations).

7.4.1 Draft example

Here, we present a draft example (draft used here to represent that this is unfinished) to demonstrate how the metrological approach can be implemented for the TDP. The processing chain from initial satellite observations to post-processed data products of geophysical variables (the measurands to be compared) are discussed in more detail.

7.4.1.1 Defining the measurand and measurement model

Figure 7.8 shows an uncertainty tree diagram for the sea ice thickness TDP from the satellite. It shows all the processes from deriving the original ellipsoidal heights by re-tracking a waveform to producing sea ice thickness estimates at the resolution of the altimeter's footprint. The ellipsoidal heights of the satellite are derived by utilising the altitude of the satellite h_{sat} with reference to some reference frame (e.g., WGS84) at the geodetic coordinates of the altimeter observations denoted by (ϕ, λ, t).

From the ellipsoidal heights, we remove the re-tracked range (ρ) observed by the altimeter. Furthermore, geophysical corrections – for the ocean loading tide (OLT), solid Earth tide (SET), ocean tide (OT), geocentric pole tide (GPT) and long-period equilibrium tide (LPET) – and atmospheric corrections – ionosphere (I), dry troposphere (DT), wet troposphere (WT), dynamic atmospheric/inverse barometric (DAC/IB) – must be applied as well to remove their impact. Here, we include the associated uncertainty of interpolating the corrections into the geodetic coordinates of the satellite observations in the +0 term. The measurement function now reads

$$h_{\mathrm{e}}(\phi, \lambda, t)_{20\mathrm{Hz}} = h_{\mathrm{sat}}(\phi, \lambda, t)_{20\mathrm{Hz}} - \rho(\phi, \lambda, t)_{20\mathrm{Hz}} - C_{\mathrm{OLT}} - C_{\mathrm{SET}} - C_{\mathrm{OT}} - C_{\mathrm{GPT}} - C_{\mathrm{LPET}} - C_{\mathrm{I}} - C_{\mathrm{DT}} - C_{\mathrm{WT}} - C_{\mathrm{DAC/IB}} + 0.$$

(7.1)

Note, that later in the processing, when the height over sea (leads) is subtracted from the height over ice (floes), several of these corrections will, at least partially, cancel out, so an uncertainty analysis, must consider that full processing.

From the ellipsoidal heights, we retrieve the surface height anomaly, h_{SHA} – also referred to as sea surface height or sea surface anomaly – by removing the mean sea surface (MSS). This ensures that the surface height anomalies are with reference to the mean sea surface. The mean sea surface is also resampled (interpolated) into the geodetic coordinates of the satellite observations but are not with reference to the same time since the mean sea surface is averaged over a defined period (which changes depending on the version of the mean sea surface). This is denoted by $(\phi, \lambda, t_{\mathrm{avg}})$. Uncertainties associated with interpolation and spatial mismatch is included in the +0 term. The measurement function now reads

$$h_{\mathrm{SHA}}(\phi, \lambda, t)_{20\mathrm{Hz}} = h_{\mathrm{e}}(\phi, \lambda, t)_{20\mathrm{Hz}} - MSS(\phi, \lambda, t_{\mathrm{avg}})_{20\mathrm{Hz}} + 0.$$

(7.2)

From the surface height anomalies, one can now determine the ice level anomaly (h_{ILA}) and sea level anomaly (h_{SLA}). This is derived by applying a surface classification, that separates the satellite-measured surface height anomalies into anomalies originating from floes at geodetic locations (ϕ_0, λ_0, t_0) and leads at geodetic locations $(\phi_{0-\tau}, \lambda_{0-\tau}, t_{0-\tau})$. Both measurement models (equations) include a +0 term associated with the surface classification procedure. The ice level anomaly directly takes the surface height anomalies at the floe locations as input. However, the sea level anomaly at those locations is not measured by the satellite. Additional processing is required to derive sea level anomalies at the sampling location of floes. Here, the surface height anomalies at the lead locations $(\phi_{0-\tau}, \lambda_{0-\tau}, t_{0-\tau})$ are interpolated into the geodetic coordinates of the floes (ϕ_0, λ_0, t_0) using some type of defined interpolation scheme. This introduces additional +0 contributions associated with the interpolation itself and with speckle/noise in the radar observations.

The interpolation scheme is also impacted by the lead density which is defined by the surface classification procedure (as well as the actual presence of leads in the data). The measurement function now reads either

$$h_{\text{ILA}}(\phi_0, \lambda_0, t_0) = h_{\text{SHA}}(\phi_0, \lambda_0, t_0)_{20\text{Hz}} + 0,$$

(7.3)

for ice level anomaly, or

$$h_{\text{SLA}}(\phi_0, \lambda_0, t_0) = f_{\text{interp}}(\boldsymbol{h}_{\text{SHA}}(\phi_{0-\tau}, \lambda_{0-\tau}, t_{0-\tau})_{20\text{Hz}}) + 0$$

(7.4)

for sea level anomaly. From the ice and sea level anomaly at the geodetic coordinates of the floes, the first measurand of interest to sea ice altimetry can be derived, the Ku-band radar freeboard denoted as $FB_{\text{Ku}}(\phi_0, \lambda_0, t_0)$. This is derived by subtracting the sea level anomaly from the ice level anomaly according to the following measurement function

$$FB_{\text{Ku}}(\phi_0, \lambda_0, t_0) = h_{\text{ILA}}(\phi_0, \lambda_0, t_0) - h_{\text{SLA}}(\phi_0, \lambda_0, t_0) + 0.$$

(7.5)

Here, the +0 term includes the uncertainty associated with the interpolation process.

Finally, the processing that takes the radar freeboard to the sea ice thickness estimates (SIT) can be performed. In this measurement function, we also include the conversion of radar freeboard to sea ice freeboard (not explicitly defined) by considering the slower propagation speed when travelling through snow ($P(1 + S \cdot \rho_s)^{1.5}$). Here, P relates to how far the radar signal has penetrated (which is currently not well known, so could potentially be introduced in the +0 term). S is defined by laboratory experiments and currently given as a constant value (see more in Section 2.2.1). Here, the densities of sea water, ice and snow must be known (denoted as ρ_w, ρ_i, and ρ_s, respectively). Furthermore, the depth of the snow layer on top of the ice floes (SD) must be known. Snow depth estimates must be interpolated into the location of the floes (ϕ_0, λ_0, t_0) using some defined interpolation scheme. The densities are commonly constant, however recent studies have suggested using a time-varying snow density estimate. For simplicity, we keep all densities as constants in the diagram, but introduce any temporal and spatial mismatch in the +0 term. The +0 term must also hold the uncertainty related to interpolation of snow depth along the satellite trajectory. The measurement function to derive sea ice thickness now reads

$$T(\phi_0, \lambda_0, t_0)_{20\text{Hz}} = \frac{\rho_w}{\rho_w - \rho_i} FB_{\text{Ku}}(\phi_0, \lambda_0, t_0)_{20\text{Hz}}$$
$$+ \frac{\rho_w \cdot P(1 + S \cdot \rho_s)^{1.5} - \rho_w + \rho_s}{\rho_w - \rho_i} SD(\phi_0, \lambda_0, t_0) + 0$$

(7.6)

The quantification and propagation of these uncertainties requires a dedicated analysis of the FDR/TDP itself and is beyond the scope of the St3TART project. However, a simplified quantification is proposed in the following sub-section.

We have added the uncertainties from the TDP traceability uncertainty diagram Figure 7.8 to an effects table in Appendix B describing (and quantifying where possible) the various uncertainties according to literature.

7.4.1.2 Simplified quantification of Sea Ice Thickness uncertainties

Altimeters such as Sentinel-3A and B allow to measure the height of the floes relatively to the local sea level: the radar-freeboard. The Sea Ice Thickness can then be retrieved using Equation (2.5)which is a simplified version of the previous equation (7.6):

$$SIT = \frac{\rho_w}{\rho_w - \rho_i} FB_{Ku} + \frac{\rho_s - \rho_w\left(1 - \frac{c}{c_s}\right)}{\rho_w - \rho_i} SD$$

(7.7)

In this equation, c/c_s depends on the snow density ρ_s. For instance, Ulaby et al. (1986) [RD-108] suggest the following relationship: $c/c_s = (1 + 0.00057\,\rho_s)^{1.5}$. With these hypotheses, the SIT depends on 5 independent variables, the radar-freeboard, the snow depth and the 3 densities, and its square uncertainty can be expressed as the sum of the squares of the 5 partial derivatives multiplied by each uncertainty u_x:

$$u^2_{SIT} = u^2_{FBku}\left[\frac{\rho_w}{\rho_w - \rho_i}\right]^2 +$$
$$u^2_{SD}\left[\frac{\rho_w(1 + 0.00051\,\rho_s)^{1.5} - \rho_w + \rho_s}{\rho_w - \rho_i}\right]^2 +$$
$$u^2_{\rho s}\left[\frac{1 + 0.000765\,\rho_w(1 + 0.00051\,\rho_s)^{0.5}}{\rho_w - \rho_i}\,SD\right]^2 +$$
$$u^2_{\rho w}\left[-\frac{\rho_i\,FB_{Ku} + SD(\rho_s - \rho_i + \rho_i(1 + 0.00051\,\rho_s)^{1.5})}{(\rho_w - \rho_i)^2}\right]^2 +$$
$$u^2_{\rho i}\left[\frac{\rho_w\,FB_{Ku} + SD(\rho_s - \rho_w + \rho_w(1 + 0.00051\,\rho_s)^{1.5})}{(\rho_w - \rho_i)^2}\right]^2$$

This equation can be written using the following form, where c_x are coefficients that depend on the 5 parameters that characterise the floe and its measurement (ie, the radar-freeboard, the snow depth and the 3 densities) and u_x is the uncertainty associated to each of these parameters:

$$u^2_{SIT} = c^2_{FBku}\,u^2_{FBku} + c^2_{SD}\,u^2_{SD} + c^2_{\rho s}\,u^2_{\rho s} + c^2_{\rho i}\,u^2_{\rho i} + c^2_{\rho w}\,u^2_{\rho w}$$

Using the uncertainty values provided in the Effects Table in Appendix B we can apply this equation on typical cases. In the table below we consider a 1.40m thick FYI floe covered with 15cm of snow and a 2.14m thick MYI covered with 35cm of snow.

	FYI (FBi=**10cm**)				MYI (FBi=**20cm**)			
	mean	u	c^2	c^2u^2	mean	u	c^2	c^2u^2
FBku(m)	0.06	**0.10**	90.07	**0.90**	0.12	**0.10**	52.0	**0.51**
SD (m)	**0.15**	0.10	29.67	**0.30**	**0.35**	0.10	13.5	**0.14**
ρi (kg/m³)	**917**	**36.0**	$16.8\ 10^{-5}$	**0.22**	**882**	**23.0**	$23.1\ 10^{-5}$	**0.12**
ρs (kg/m³)	**324**	**3.2**	$65.8\ 10^{-7}$	**0.00**	**290**	**3.2**	$20.5\ 10^{-6}$	**0.00**
ρw(kg/m³)	**1025**	**0.5**	$14.5\ 10^{-5}$	**0.00**	**1025**	**0.5**	$19.0\ 10^{-5}$	**0.00**
SIT (m)	1.40	1.19			2.14	0.88		

This table shows that the main uncertainties are coming from the uncertainties of the radar-freeboard, the snow depth and the ice density. The uncertainties of the densities of the snow and the water are negligible. The following figure shows the SIT uncertainty according to the measured radar-freeboard uncertainty for MYI (in bold) and FYI (light line).

Hyp FYI: FBi 0.10 SD 0.15±0.10 Rho 917±36 PR_KU 1.00±0.23 PR_KA 0.00±0.07 => SIT 1.40
Hyp MYI: FBi 0.20 SD 0.35±0.10 Rho 882±23 PR_KU 1.00±0.10 PR_KA 0.00±0.03 => SIT 2.14
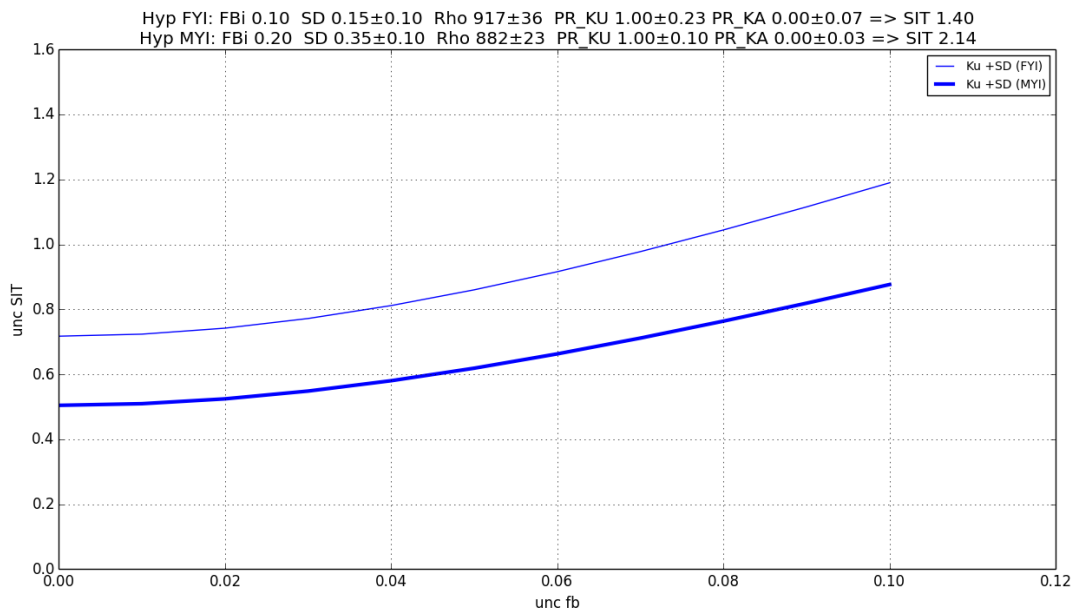
Figure 7.7: SIT uncertainty according to the measured radar-freeboard uncertainty for a typical MYI case of 2.14m with a snow cover of 0.35m (in bold) and a typical FYI case of 1.40m with a snow cover of 0.15m (light line).
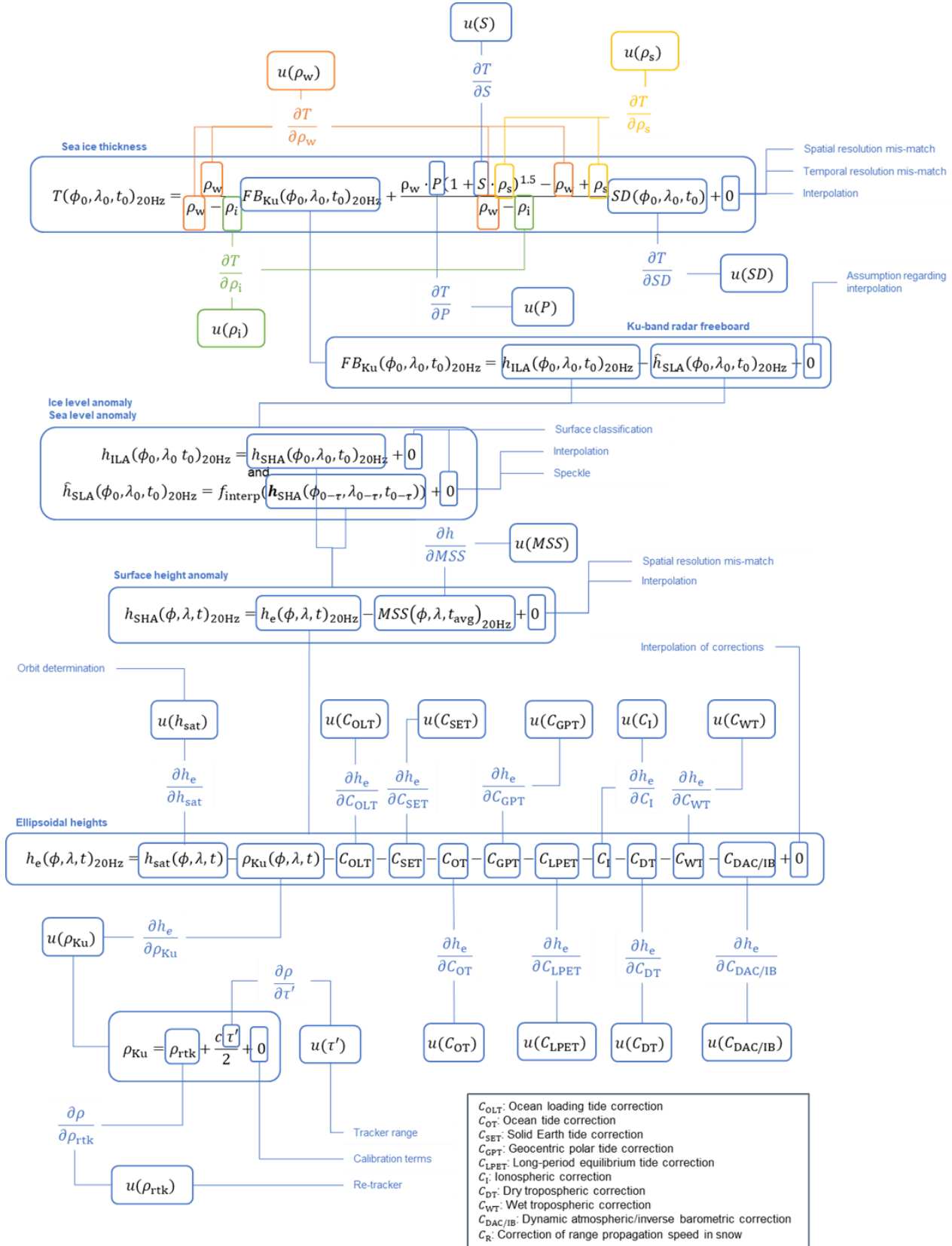
7.4.1.3 Traceability uncertainty diagram

Figure 7.8: Illustration of an uncertainty diagram for sea ice altimetry and relevant measurands.

7.5 Implementing metrological uncertainty analysis for sea ice FRMs

Figure 3.1 shows various validation scenarios for sea ice altimetry. For each scenario, the FRM processing and procedures are different. The full uncertainty evaluation of all possible FRMs is beyond the scope of this project. In this section, however, we provide a draft example of uncertainty analysis for a simple FRM.

In this scenario, an airborne Ku-band radar, such as ASIRAS or CReSIS, collects the same measurand as the satellite altimeter. This is therefore the most straightforward comparison to the satellite altimetry processing in which radar freeboard is derived. Here we describe the setup for collecting the FRM, followed by the metrological procedures to estimate the uncertainty of the FRM.

Figure 7.9 shows a representative FRM setup for validating Sentinel-3 over sea ice. The aircraft underflies the satellite using the same kind of altimeter (Ku band radar) as the satellite, which is expected to have similar penetration depths in the snow layer. In this way it is the FRM that is most similar to the satellite, however, differences in the vertical resolution can introduce different re-tracking points in the associated waveforms.

The aircraft radar altimeter observation measures the distance from the aircraft to the surface, which is subtracted from the altitude of the aircraft (relative to the Earth's ellipsoid measured by a GNSS receiver on board the aircraft) to derive surface heights. The derived surface height differs from the satellite methods as no atmospheric corrections need to be applied (this is not needed as the aircraft nominal survey altitude is about 300 m above ground level (AGL)), and the observation footprint is much smaller (~10 m, rather than ~1.5 km across track, and ~3 m rather than ~300 m along track).

For this kind of campaign, the aircraft follows a track matching the predicted satellite ground track. However, the flight takes a few hours, so the satellite overpass is only perfectly matched in time at one point along the track if the flight is a direct underflight. The spatial matching may also not be perfect as described in Section 3.3.2. There are different approaches of comparing the airborne observations to the satellite:

- The along-track match. In this, individual points can be compared between the satellite track and the aircraft track. To get the best matches, the aircraft observations must be averaged up to match the satellite footprint, and, ideally, also be spatially corrected to account for both sea ice drift (i.e., the specific section of sea ice observed by a satellite may be in a different position when the aircraft measured it an hour or so earlier or later), and the actual satellite ground track.
- The gridded product match. In this, the aircraft and satellite data are averaged over a much longer time period and much larger spatial grid. The gridded products are then compared with one another.

The initial FRM processing steps for the above-mentioned scenarios are similar. Therefore, we include them both in the following discussion. When necessary, we distinguish between the two scenarios by adding sections in the text or using color-codes in the diagrams.

Our analysis shows that even in a simple FRM, set up chosen to be as identical to the satellite observation as possible, considerable care is required to understand how the comparison is done and what the comparison products are. Of course, for FRMs using different technologies, more processing is required (as shown in the comparison diagram in Section 3.3.1).
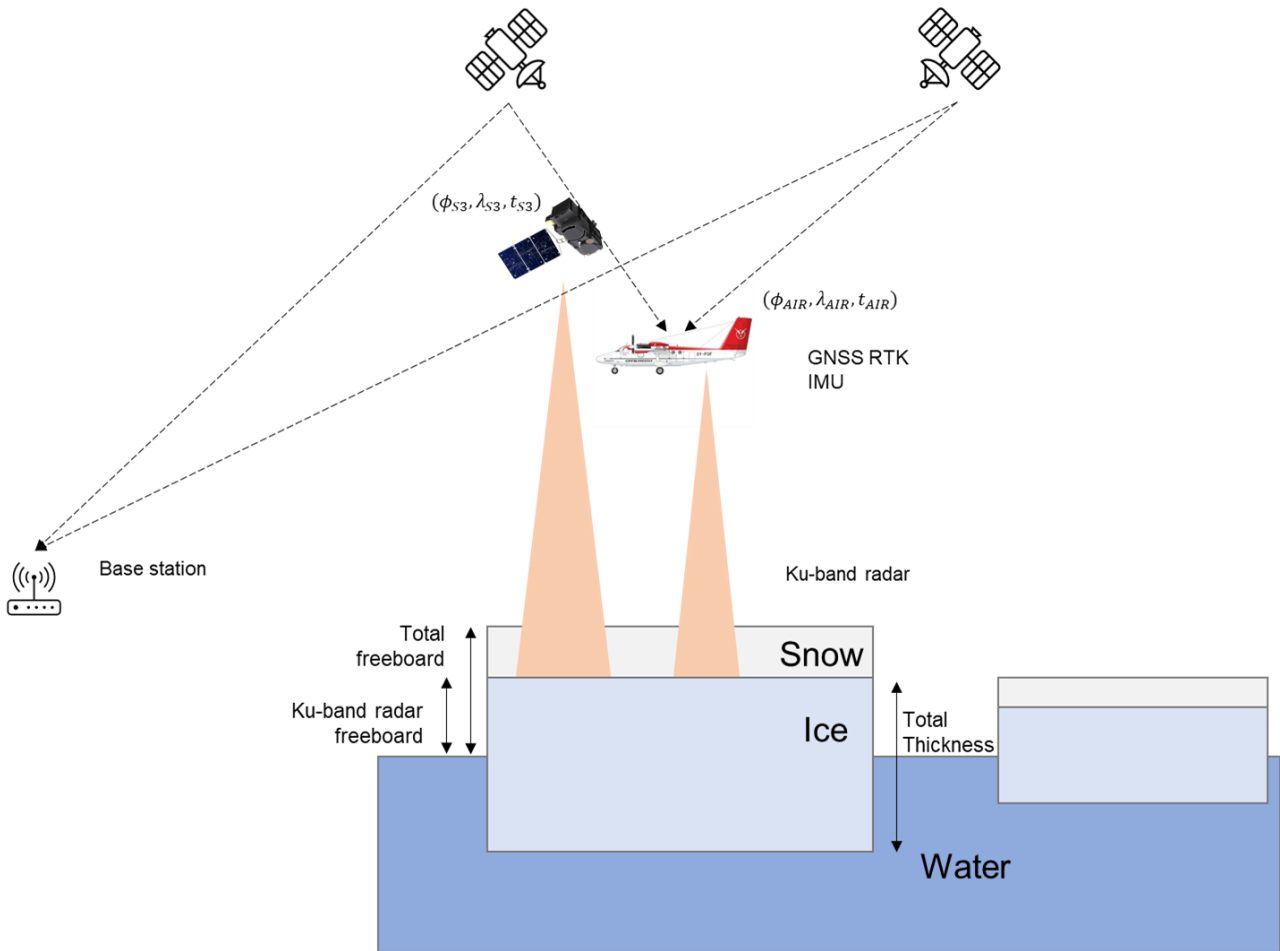
Figure 7.9: Diagram of airborne Ku-band radar FRM set up over sea ice and related measurements such as GNSS and IMU measurements with Sentinel-3 overpassing the set up.

7.5.1 FRM uncertainties

7.5.1.1 Defining the measurand and measurement model

As implied in the discussion above, identifying a measurand is often more complicated than expected, and with Earth observation data, chances are that often more than one measurand can be identified. It could be that the products of different processing steps and levels make up a set of possible measurands, but not all the identified measurands can be validated with reference measurements. Each processing level (measurand) of the FRM observations required to make it comparable to the satellite observations is described in further detail below.

7.5.1.1.1 Height acquired by airborne Ku-band radar

To compute the ellipsoidal heights from the airborne Ku-band radar $h_{\text{AIR,Ku}}$, the re-tracked range ρ_{Ku} is subtracted from the altitude of the aircraft $h_{\text{GNSS}}^{\text{RTK}}$. In this example the altitude of the aircraft is determined via a real-time-kinematic solution referenced to a specific ellipsoid (preferably the same reference ellipsoid that is used by the satellite). It is important to notice that the RTK GNSS height represents the height of the on-board GNSS antenna reference point. Therefore, we need to apply a correction to account for the distance between the GNSS antenna and the onboard altimeter. This correction can be notified as Δh_{offset}. A correction, Δh_{corr}, is also made to account for the delay time of the onboard electronics. To estimate the Δh_{offset} and Δh_{corr} typically, procedures are to make a calibration between the airborne Ku-band radar and ALS over a flat surface, where both the Ku-band radar and ALS is known to reflect on the same surface. Commonly used approach is to make flights over runway and compare the elevations from both sensors to calculate the offset ($\Delta h_{\text{offset}} + \Delta h_{\text{corr}}$). The measurement function therefore reads

$$h_{\text{AIR,Ku}}(\phi, \lambda, t) = \left[h_{\text{GNSS}}^{\text{RTK}}(\phi_\eta, \lambda_\eta, t_\eta) - \rho_{\text{Ku}}(\phi, \lambda, t) \right] - \Delta h_{\text{offset}} - \Delta h_{\text{corr}} + 0. \tag{7.8}$$

$h_{\text{AIR,Ku}}(\phi, \lambda, t)$ is the measured height of the surface, at position (ϕ, λ) and time t relative to the Earth's ellipsoid. We also note that the airborne radar and the GNSS receiver do not share the same sampling point which is clearly represented in the FRM uncertainty diagram with different geodetic coordinates: (ϕ, λ, t) and $(\phi_\eta, \lambda_\eta, t_\eta)$, respectively. Here, the GNSS observations are resampled to the geodetic coordinates of the airborne radar.

It is important to note, that the +0 term includes uncertainties associated with the resampling, as well as an outlier removal procedure including the removal of observations associated with high roll-angles (typically values used for ASIRAS is ±1.5°) which results in waveform blurring. We also note that the uncertainty of ρ_{Ku} depends on the re-tracker used to retrieve the range, where this uncertainty traceability diagram is similar to the TDP uncertainty diagram for the satellite's range, ρ_{Ku}. This traceability is highlighted in the FRM uncertainty diagram by a thick arrow extending from the effects of ρ_{Ku} (which is denoted $u(\rho_{Ku})$ in the traceability diagram) but has not progressed further.

7.5.1.1.2   Sea and ice level anomalies from airborne Ku-band radar observations

To derive freeboard estimates from the surface heights, we must first properly correct the signal for any geophysical effects (e.g., tides and inversed barometer effect), defined as C_{geo}, and reference the observations to a mean sea surface (MSS). However, the geophysical corrections and the MSS are rarely given with a similar sampling rate as the airborne observations and must therefore be resampled/interpolated into the locations of the airborne observations geodetic coordinates (ϕ, λ, t). It is important to note that only the geophysical corrections are dependent on the time (t), whereas an MSS is based on an average of measurements defined over a specific period (which can vary depending on the MSS used). We denote this averaged period of the MSS as t_{avg}. Hence, the surface height anomaly acquired by the Ku-band radar observations can be described as

$$h_{\text{SHA}}(\phi, \lambda, t) = h_{\text{AIR,Ku}}(\phi, \lambda, t) - C_{\text{geo}}(\phi, \lambda, t) - MSS(\phi, \lambda, t_{\text{avg}}) + 0 \tag{7.9}$$

$h_{\text{SHA}}(\phi, \lambda, t)$ is the instantaneous surface height anomaly measured by the airborne radar after removing the impact of geophysical corrections $C_{\text{geo}}(\phi, \lambda, t)$ from the ellipsoidal heights $(h_{\text{AIR,Ku}}(\phi, \lambda, t))$ and referenced to the mean sea surface ($MSS(\phi, \lambda, t_{\text{avg}})$). The +0 term includes the projection (ensuring a common map projection for all observations) and interpolation of the geophysical corrections and MSS into the geodetic coordinates of the radar observations.

Note that the term h_{SHA} is an intermediate quantity in the processing to obtain "sea level anomaly" or "ice level anomaly". It has sometimes been called Sea Surface Height Anomaly (SSHA)

h_{SHA} is interpreted based on a classification of whether the surface is ice (floes) or water (leads). This classification is performed on the waveform shape. Over floes, the ice level anomaly (ILA) is the identical to the surface height anomaly (SHA) because the instantaneous height is used directly. Mathematically,

$$h_{\text{ILA}}(\phi_0, \lambda_0, t_0) = h_{\text{SHA}}(\phi_0, \lambda_0, t_0) + 0. \tag{7.10}$$

Here, the plus zero term includes uncertainties associated with the classification of a particular observation as ice and aspects of mixed observations due to the radar footprint possibly covering both ice and water.

To calculate the radar freeboard, we need to obtain a sea level anomaly at the location and time of the ice measurement (ϕ_0, λ_0, t_0). We do not have a measurement at that location. Instead, we use observations from nearby leads, and interpolate these to the desired location. As a simple example, the sea level anomaly at (ϕ_0, λ_0, t_0) can be calculated from a linear interpolation of sea level anomalies of the nearest leads before and after (ϕ_0, λ_0, t_0). These h_{SHA} measurements are represented as being at locations and times with the index $(0 - \tau)$ and $(0 + \tau')$. In that case we would obtain a sea level anomaly at the point of the ice measurement as:

$$\hat{h}_{\text{SLA}}(\phi_0, \lambda_0, t_0) = f_{\text{interp}}\left(h_{\text{SHA}}(\phi_{0-\tau}, \lambda_{0-\tau}, t_{0-\tau}), h_{\text{SHA}}(\phi_{0-\tau'}, \lambda_{0-\tau'}, t_{0-\tau'}) \right) + 0. \tag{7.11}$$

More generally, the interpolation routine could use multiple observations and could take other forms. The generalised version of this equation is:

$$\hat{h}_{\mathrm{SLA}}(\phi_0, \lambda_0, t_0) = f_{\mathrm{interp}}\big(\boldsymbol{h}_{\mathrm{SHA}}(\phi_{0-\tau}, \lambda_{0-\tau}, t_{0-\tau})\big) + 0. \tag{7.12}$$

Note that the hat in $\hat{h}_{\mathrm{SLA}}$ represents that this is an interpolated, rather than measured quantity. Here the +0 term includes uncertainties associated with the choice of interpolation function, as well as uncertainties associated with the classification.

7.5.1.1.3 Ku-band freeboard estimates for FRM

The freeboard from the FRM (in this case the airborne Ku-band radar) is easily determined at the location of the ice floes by subtracting the sea level anomalies ($h_{\mathrm{SLA}}(\phi_0, \lambda_0, t_0)$) from the ice level anomalies, h_{ILA}, at the location of the floes (ϕ_0, λ_0, t_0). Here, we include in the +0 term the assumption that this interpolation suffices to provide a measure of the local sea surface height anomaly, which is purely dependent on the interpolation methodology (or other type of sea surface height anomaly retrieval). The measurement function for the FRM Ku-band radar freeboard now reads

$$FB_{\mathrm{Ku}}^{\mathrm{FRM}}(\phi_0, \lambda_0, t_0) = h_{\mathrm{ILA}}(\phi_0, \lambda_0, t_0) - \hat{h}_{\mathrm{SLA}}(\phi_0, \lambda_0, t_0) + 0. \tag{7.13}$$

At this stage, the FRM freeboard estimates are not directly comparable to what the satellite is observing. When comparing with satellites, two common approached are often taken: (a) comparing along-track freeboards of direct under-flights with freeboards from that exact satellite pass, or (b) comparing gridded FRM freeboards with gridded satellite freeboards where several tracks over the course of a specific time interval is selected. We shall consider both scenarios below.

7.5.1.1.4 FRM along-track comparable airborne Ku-band observations

When comparing along-track observations of satellites and FRMs, it is important to make the observations comparable. For the case of sea ice, this includes considering the sea ice drift (C_{DRIFT}). Such a drift correction is applied by deriving the drift (shift) between the satellite pass and the airborne observations, this is done by either using local measurements such as crossovers from the airborne campaign or nearby drifting buoys or ship logs if these are drifting with the ice, drifting buoys or by auxiliary data products). It is however not always straightforward to compute such a drift correction; it can be done both automatically and manually, however there are limitations with both aspects. A manual correction may be able to account for non-uniform drift (the entire ice pack not moving as one), but it is time consuming to correct each point if they were to be applied to individual drift corrections. Furthermore, the resolution of potential auxiliary data products used to derive the drift will also impact the accuracy of the drift correction. The drift must be derived between the FRM observation's locations (ϕ_0, λ_0, t) and the location of which the FRM and satellite tracks are comparable (ϕ'', λ'', t''). Hence, the drift correction is denoted $C_{\mathrm{DRIFT}}(\phi_0 - \phi'', \lambda_0 - \lambda'', t_0 - t'')$. The sea ice drift only impacts the location of the freeboard estimate, not the actual height of the freeboard estimates. Actually, the sea ice drift can change the sea ice freeboard height, in case of diverging or converging motion of the sea ice. As this is usually assumed not to be the case, if the airborne campaign is flown during or close to satellite passage time, we will not include this here.

Now to make the FRM freeboards comparable to the satellite observations, the data must be resampled to the location where the FRM freeboards and satellite freeboards are comparable. This location could be the satellite observations or could be the FRM locations – or something completely different. Different approaches have been used across studies. To generalise, we will denote this as location of comparability, denoted by (ϕ'', λ'', t''). To sample to this location, often some re-sampling must be done including area transfer/averaging. This is included in the +0 term. Furthermore, there can be cases where the trajectories do not match well, which is also included in the +0 term along with the question of representation. The measurement function for an individual along-track FRM observations now reads

$$FB_{\mathrm{AT}}^{\mathrm{FRM}}(\phi'', \lambda'', t'') = FB_{\mathrm{Ku}}^{\mathrm{FRM}}(\phi_0, \lambda_0, t_0) - C_{\mathrm{DRIFT}}(\phi_0 - \phi'', \lambda_0 - \lambda'', t_0 - t'') + 0 \tag{7.14}$$

showing the correction for drift. More generally, the along-track freeboard may be obtained by combining multiple measurements calculated with equation (7.14), through a combination function. This could, for example, be a local mean, median or minimum to account for the fact that the satellite footprint is much larger than the aircraft footprint and several aircraft observations need to be combined (before, or after, drift correction). A general form of the equation would be:

$$FB_{\text{AT}}^{\text{FRM}}(\phi'', \lambda'', t'') = f_{\text{comb}}\left(\boldsymbol{FB}_{\text{Ku}}^{\text{FRM}}(\phi_0, \lambda_0, t_0) - \boldsymbol{C}_{\text{DRIFT}}(\phi_0 - \phi'', \lambda_0 - \lambda'', t_0 - t'')\right) + 0,$$

(7.15)

where f_{comb} represents the combination function, and bold is used to represent a vector of individual observations.

7.5.1.1.5 FRM gridded comparable airborne Ku-band observations

Another comparison scenario is comparing gridded satellite observations with gridded reference observations. This is often applied to remove the impact of temporal and spatial differences. Here, both the satellite and FRM observations are gridded to the same grid with the same conditions (spatially and temporally). The change in location (spatially and temporally) is denoted by (ϕ', λ', t'), see Figure 7.10 .
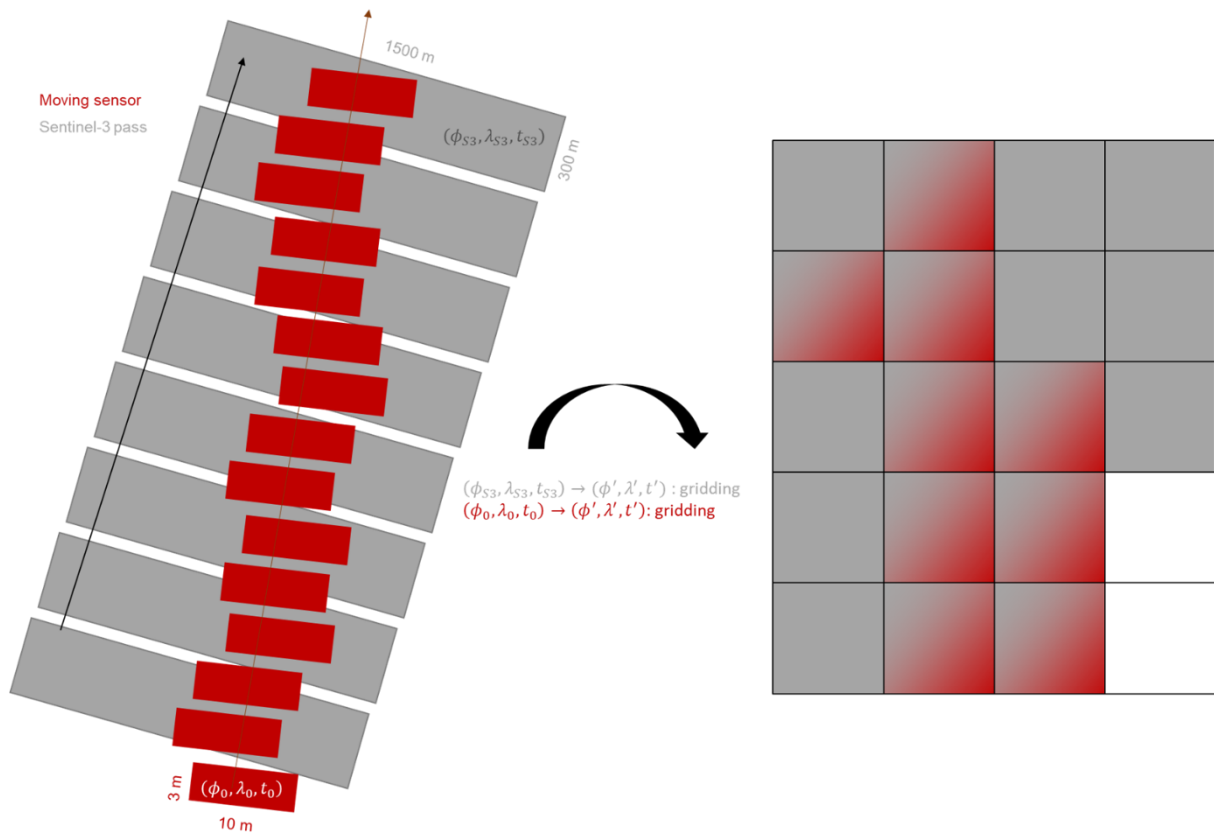

Figure 7.10 Gridding of FRM and satellite observations to a comparable grid.

The gridding methodology can differ depending on the user and is therefore only denoted as a function of gridding. The gridding methodology may be a simple spatial averaging or could include weights based on difference in space, time etc.

To generalise this, we denote the gridding methodology as $f_{\text{grid}}\left(\boldsymbol{FB}_{\text{Ku}}^{\text{FRM}}(\phi_0, \lambda_0, t_0)\right)$. The +0 term will now include the resampling of the observations to the locations of the grid, the aspect of representation when gridding as well as the assumption that one assumes the gridding ensures comparability. The measurement function for a gridded FRM Ku-band freeboard estimate now reads

Ref	NOV-FE-1464-NT-043		
Issue	1	Date	26/11/24
Rev	0	Date	26/11/24
Page	105/120		

Sᴛ3TART-FOLLOW-ON: FIDUCIAL REFERENCE MEASUREMENTS (FRM) - S3 LAND ALTIMETRY

$$FB_{\mathrm{GRID}}^{\mathrm{FRM}}(\phi', \lambda', t') = f_{\mathrm{grid}}\left(\boldsymbol{FB}_{\mathrm{Ku}}^{\mathrm{FRM}}(\phi_0, \lambda_0, t_0)\right) + 0.$$

(7.16)

For example, for an averaged grid, this could be written:

$$FB_{\mathrm{GRID}}^{\mathrm{FRM}}(\phi', \lambda', t') = \sum_i w_i FB_{\mathrm{Ku}}^{\mathrm{FRM}}(\phi_i, \lambda_i, t_i) + 0$$

(7.17)

where w_i are weights for each gridded observation (denoted by index i). The weights may be those for a simple mean, perhaps with some weights set at zero to perform quality control, or may be more complex. However, other approaches are also used (e.g., median values), so we consider the general gridded case.

7.5.1.2 Example of an uncertainty traceability diagram for an airborne Ku-band radar as an FRM

Figure 7.11 gives a first-draft uncertainty tree diagram for an airborne Ku-band radar FRM. The main equation is the central equation in a blue box (the double line represents that there will be multiple observations that fulfil this equation). This is the equation for the freeboard, which is calculated from the sea level anomaly and ice level anomaly, which are in turn calculated from the measured heights. The lower part of the diagram describes the derivation of the FRM freeboard values.

In the upper part of the diagram, we see two separate comparison quantities that can be calculated from the FRM freeboards: either the along-track FRM or the gridded FRM. These quantities are those which can be compared with the satellite observations.
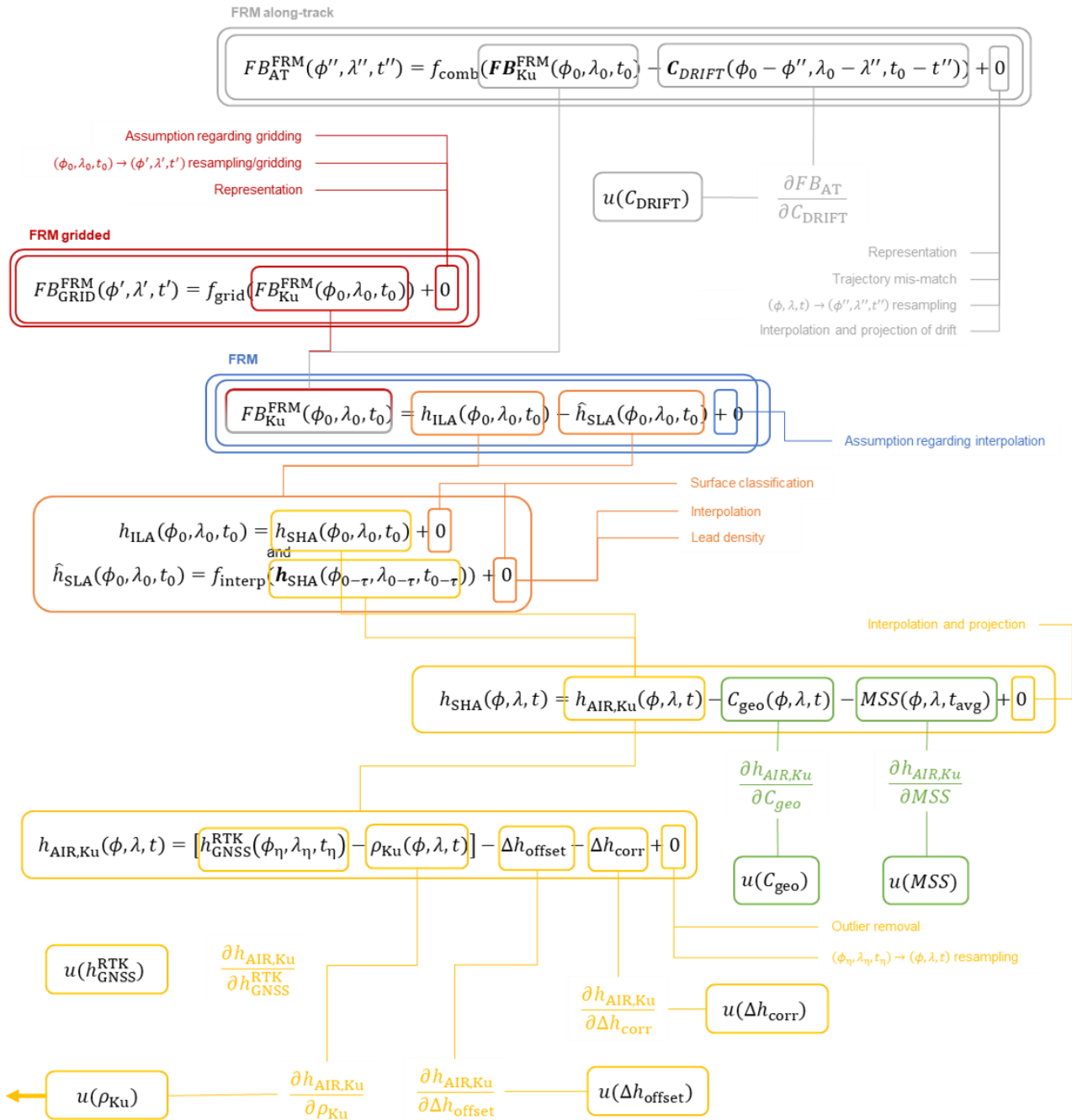
Figure 7.11 Draft example of an uncertainty traceability diagram using an airborne Ku-band radar.

7.5.1.3 Establishing the effects table of the airborne Ku-band FRM and calculating the uncertainties

Here we combine considerations of steps 3 and 4 in the metrological approach. In this draft uncertainty budget we have not yet done sufficient analysis to establish effects tables. An effects table lists all sources of uncertainty and considers their error correlation structures in all relevant dimensions. In a later project we will consider that in detail for the sources of uncertainty identified here.

As discussed in this report, there are different possible observation quantities, from the SLA/ILA to the freeboard to the ice thickness. When we propagate uncertainties through this processing chain, we need to consider the error correlations. For example, (from Figure 7.11), both SLA and ILA are calculated from data that has been corrected for several quantities, including Δh_{offset} and Δh_{corr} in the measured height $h_{\text{Air,Ku}}$ and the C_{geo} in the surface height anomaly. These corrections will be the same, or at least extremely similar, for the SLA observation and the ILA observation at

almost the same time and location, and therefore need to be treated as fully (or mostly) correlated, when propagating uncertainties.

However, such correlations go further, because measurements on the same ice floe, and on nearby ice floes at nearly the same time will also use the same corrections. Because the FRM data will be combined in some way in later processing (e.g., averaging over an area), we need to document error correlation structures. The 'relevant dimensions' are the dimensions over which data are combined in later processing (which can include later processing by other communities). Here, we expect individual FRM observations to be spatially combined (either through averaging, or through more sophisticated processes) to match the footprint of the satellite and/or to create gridded (spatially and temporarily) products.

The effects table will therefore describe error correlation structures over temporal and spatial scales, with the most relevant scales being those that are combined for along-track comparisons and those combined for gridded products. An example of such an effects table (using the TDP uncertainty diagram as an example) is presented in Appendix B. Here, we adapt the effects table presented in [RD145] and include information regarding correlation structures to the effects along with their uncertainty quantities.

The actual calculation of the uncertainties can be performed using either the Law of Propagation of Uncertainty (the full form that considers covariance), or by using Monte Carlo methods. Both methods are described in the Guide to the Expression of Uncertainties in Measurement (the GUM [RD142]). Monte Carlo methods are flexible and can handle complex processing including classification steps, highly non-linear and reverse algorithms, and iterative processes much more straightforwardly than the Law of Propagation of Uncertainty. On the other hand, Monte Carlo methods are computationally expensive and cannot usually be applied to large data sets. A mixed approach is also possible, where Monte Carlo methods are used to identify the sensitivity coefficients then used in the Law of Propagation of Uncertainties. In a later phase of this activity, we will perform the data analysis.

7.5.1.4   Providing uncertainty information with the FRM

It is too early to define how uncertainty information will be provided with an FRM. However, it is likely that uncertainties need to be provided for both along-track and gridded products on a product-by-product basis. Most users are unlikely to be able to use the full covariance information that is determined in a rigorous metrological analysis, so summary information should be provided, perhaps by giving along-track and gridded product uncertainties. All information should be stored and made available to the small number of scientists who can use it for the purposes of long-term data preservation and open/reproducible science.

Appendix A – Compliancy matrix

Comparison of the strengths and drawbacks of all sensors for an operational FRM provision with categories, legends, and rankings defined in Section 7.2.

Sensor	Platform	Measurand	Accuracy of the measurand	Representativeness Measurand	Traceability of uncertainties	TRL	SRL	Latency timeNRL provision	Costs	Rank
Ku-band radar	Aircraft	FBKu	±10 cm	++	+	++	+	-	+	A+
ULS	Mooring	D	5-10 cm	+	++	++	++	--	-	A+
Laser scanner	Aircraft	FBtotal	±10 cm	+	++	++	++	-	+	A
EM	Aircraft Helicopter	SITtotal	±10 cm level ice Unavailable for thick and rough ice	+ -	++	++	+	-	+	A
Lidar	Drone	FBtotal	±10 cm	+	++	++	++	-	++	Ax
IMB	Drifting buoy	SIT	1-2 cm depending on temperature	+	+	++	- needs to lower uncertainty on SD	++	++	Ax
Snow radar	Aircraft	SD	< 10 cm	++	++	++	++	-	+	B+
Drilling/ snow depth	Manual	SIT FBice SD	cm-level	+	+	++	++	+	++	B+
Camera (Geo-located images)	Aircraft Drone	Surface Classification	Not available	+	-	--	+	-	++	B
Acoustic sounder	Drifting buoy	SD	1-2 cm	+	+	++	-	++	++	B
GNSS	Drifting buoy	Drift	< 50 cm in the	Not available	++	++	++	++	+	B

				horisontal							
Snow Radar	Drone	SD	< 10 cm	++	++	++	++	-	+	Bx	
	Snow radar	Ice-T buoy	SD	cm-level	+	+	--	+	++	++	Bx
ULS	AUV	D	decimeter level	+	+	-	+	-	--	Bx	
	SIMS	Ship	SITtotal	±10 cm level ice	+	++	++	--	+	-	Bx
				Unavailable for thick and rough ice	-						
Ka-band radar	Aircraft	FBKa	±10 cm	--	-	++	-	-	+	C	
	Camera (not geo-located)	Aircraft Drone	Surface Classification	Not available	--	-	-	--	-	++	C
ULS	Submarine	D	50 cm + bias	- positioning very poor	-	++	+	− Often military OPS; classified	--	C	
	Visual	Ship	SIT	±10 cm	++	−	++	--	+	+	C
			SD	Not available	++	--					

Appendix B – Effects table

Here we denote some of the recorded uncertainty estimates of the effects noted on the uncertainty diagram for the TDP Figure 7.7. Most of the estimates are based on studies using CryoSat-2 as a reference, but these should be similar for S3 when using similar baseline processing i.e., the new updated sea ice processing for S3 [RD148]. We also discuss some correlation aspects (time, spatial or other effects), but it is important to note that when using Law of Propagation (which is often done for sea ice altimetry), one assumes that the uncertainties are uncorrelated.

The impact of the geophysical corrections on sea freeboard estimation was examined in Ricker et al. 2016 [RD145].They included in their study the Ocean Tide (OT), Geocentric Polar Tide (GPT), Solid Earth Tide (SET), Long-Equilibrium Tide (LPET), Ocean Loading Tide (OLT), Dry and Wet Tropospheric Correction (DTC/WTC), Ionospheric Correction (IC), Inverse Barometric (IB) and the Dynamic Atmosphere Correction (DAC), and found that the major sea-ice covered area in the Arctic is not significantly affected by geophysical corrections, which implies that less than 1% of the area fraction (A) are affected by the specific geophysical correction greater than 1 cm, where the A is calculated as the percentage of all valid CS2 freeboard grid cells of a month of observations. In addition, MEAN($|\Delta Fb|A$) is provided as the mean of the impact on the freeboard for the grid cells contained in A. Regions with significant impact correlate with low lead fractions or lead-free areas and can be found in the multiyear ice north of Greenland and Canada, as well as over landfast ice, i.e. in the Laptev Sea. During the freeze-up in autumn, the ice cover is characterized by many leads and openings, while they are reduced in spring. Hence, the impact of geophysical corrections is higher in spring when the ice is thickest and generally low in autumn. Among the different corrections, only the ocean tides and the inverse barometric correction show substantial contributions to the impact. The study by Ricker et al. (2016) [RD145] uses the impact to the freeboard magnitude, defined by the relative impact ρ, according to the relative error:

$$\rho = |\Delta Fb| \, FbCORR0 = |FbCORRi - FbCORR0| \, FbCORR0$$

where i is the index for the considered correction, while 0 represents the reference retrieval, where no correction has been applied. The study was limited to March/November 2015, but is a good guideline for the impacts.

Effect	Name of effect	Measurement equation	Contribution subject to effect	Correlation in time and space	Correlation between effected partners	Uncertainty quantity with units	Validation of uncertainty	Reference
$u(\rho_{Ku})$	Range	Commonly, for sea ice altimetry, the uncertainty of the freeboard estimates ($\sigma_{RFB_{Ku}}$) is computed not from these effects, but rather from how well the SSHA is determined and by considering speckle noise. Here, $\sigma_{RFB_{Ku}}^2 = \sigma_{l1b}^2 + \sigma_{SSHA}^2$. The speckle noise uncertainty is described in Wingham et al. (2006) [RD146] and originates from the instrument system errors, and the SSHA is commonly derived from taking the standard deviation of the interpolated SSHA from the mean freeboard elevations. It is therefore commonly assumed that this uncertainty estimate is of a lower range. However, it is fair to assume that there is a correlation between adjacent points in time and space when considering changes in the ocean. Furthermore, these measurements will likely originate from random fluctuations, and are therefore considered random – and can usually be minimized by increasing the number of measurements. It is important to note however, that impact of re-tracker threshold, surface roughness and signal penetration has a combined uncertainty denoted in some studies (Ricker et al., 2014) [RD93].				Cryosat-2 example: $\sigma_{l1b,SAR} = 0.10\ m$ $\sigma_{l1b,InSAR} = 0.14\ m$ $\sigma_{SSHA} = 5 - 50\ cm$ $\sigma_{FB_{Ku,SAR}} = 11 - 51\ cm$ $\sigma_{FB_{Ku,InSAR}} = 14 - 52\ cm$ Combined uncertainty of re-tracker, roughness and signal penetration: 6 cm (FYI), 12 cm (MYI)	Not provided.	Ricker at al. (2014) [RD94] Wingham et al. (2006) [RD146]
$u(\rho_{rtk})$	Re-tracker							
$u(\tau')$	Tracker range							
$u(h_{sat})$	Orbit determination	Average order of standard deviation				Negligible impact if a sensor is +/- 1 km to		OSTS 2020, POE-F orbit performance

					the actual ground track		
$u(C_{OLT})$	Ocean loading tide	The impact to the freeboard magnitude, defined by the relative impact ρ			Negligible for freeboard estimates; <1cm	Not provided	Ricker et al. 2016 [RD34]
$u(C_{SET})$	Solid Earth tide	The impact to the freeboard magnitude, defined by the relative impact ρ			Negligible for freeboard estimates < 1 cm		Ricker et al. 2016 [RD34]
$u(C_{OT})$	Ocean tide	The impact to the freeboard magnitude, defined by the relative impact ρ The area fraction (A) is calculated as the percentage of all valid CS2 freeboard grid cells of	According to Ricker et al. (2016), the OT has a significant impact >1 cm in certain regions (when compared to other geophysical corrections except also the IB/DAC. The regions with significant impact correlate with low lead fractions or lead-free areas and can be found in the multiyear ice north of Greenland and Canada, as well as over landfast ice, i.e. in the Laptev Sea. During the freeze-up in autumn, the ice cover is characterized by many leads and openings, while they are reduced in spring. Hence, the impact of OT is higher in spring when the ice is thickest and generally low in autumn.		March 2015: A=7.17%, MEAN(|ΔFb|A) =4.85cm November 2015: A=2.33% MEAN(|ΔFb|A) =3.19cm		Ricker et al. 2016 [RD34]

		a month that are affected by the specific geophysical correction greater than 1 cm. MEAN(|D Fb|A) is the mean of the impact on the freeboard for the grid cells contained in A.						
$u(C_{GPT})$	Geocentric polar tide	The impact to the freeboard magnitude, defined by the relative impact ρ				Negligible for freeboard estimates < 1 cm		Ricker et al. 2016 [RD34]
$u(C_{LPET})$	Long-period equilibrium tide	The impact to the freeboard magnitude, defined by the relative impact ρ				Negligible for freeboard estimates < 1 cm		Ricker et al. 2016 [RD34]
$u(C_I)$	Ionosphere	The impact to the freeboard				Negligible for freeboard estimates		Ricker et al. 2016 [RD34]

		magnitude, defined by the relative impact ρ			< 1 cm	
$u(C_{DT})$	Dry troposphere	The impact to the freeboard magnitude, defined by the relative impact ρ			Negligible for freeboard estimates < 1 cm	Ricker et al. 2016 [RD34]
$u(C_{WT})$	Wet troposhere	The impact to the freeboard magnitude, defined by the relative impact ρ			Negligible for freeboard estimates < 1 cm	Ricker et al. 2016 [RD34]
$u(C_{DAC/IB})$	Dynamic atmosphere or inverse barometric	The impact to the freeboard magnitude, defined by the relative impact ρ The area fraction (A) is calculated as the percentage of all valid CS2	According to Ricker et al. (2016), the IB and DAC have a significant impact >1 cm in certain regions (when compared to other geophysical corrections except also the Ocean Tides (OT)). The regions with significant impact correlate with low lead fractions or lead-free areas and can be found in the multiyear ice north of Greenland and Canada, as well as over landfast ice, i.e. in the Laptev Sea. During the freeze-up in autumn, the ice cover is characterized by many leads and openings, while they are reduced in spring. Hence, the		March 2015: A=2.69%, MEAN(|ΔFb|A) =2.22cm November 2015: A=0.69% MEAN(|ΔFb|A) =2.37cm	Ricker et al. 2016 [RD34]

		freeboard grid cells of a month that are affected by the specific geophysical correction greater than 1 cm. MEAN(|D Fb|A) is the mean of the impact on the freeboard for the grid cells contained in A.	impact of DAC/IB is higher in spring when the ice is thickest and generally low in autumn.			
$u(MSS)$	Mean sea surface	$MSS = MDT + N$, where N is the geoid and MDT is mean dynamic topography.	Depends on which MSS used. In Skourup et al. (2017) they included DTU10, DTU13, DTU15, UCL04, and UCL13 MSS is often determined through years of altimetry observations, and there will therefore be a time correlation (depending on what time period used for MSS) and a spatial correlation. The MSS may even use the same satellite observations of which we are trying to obtain sea ice information if they are from the period of which the MSS has been determined from.	Depending on which MSS/GGM is used, the standard deviation of freeboard differences ranges 0.03–0.06 m, corresponding to an ice thickness uncertainty of 0.24–0.54 m.		Skourup et al. (2017) [RD147]

			When freeboard errors are compared with other sources of uncertainty (e.g., due to remaining uncertainties in geophysical range corrections), the area impacted by MSS uncertainties is more significant. Depending on the choice of MSS/GGM, approximately 60–80% of the CryoSat-2 grid cells have freeboard differences greater than ±1 cm. This compares to an area impact of only 3–7% for errors due to uncertainties in the ocean tide or inverse barometer corrections (Ricker et al., 2016). The impact depends heavily on the lead fraction, as is the case for OT and IB/DAC, and is thus regional and seasonal dependent.				
$u(P)$	Penetration depth	Currently there is no standard method for deriving the penetration depth and applying it to the observations. It is merely stated in the uncertainty diagram to reflect the optimal scenario in case such information was available. The hope is that future studies will be able to answer this.					
$u(S)$	Propagation speed through snow	Not available.		Not available.	Not available.	Not available.	Not available.	Ulaby et al. (1986) [RD108]
$u(SD)$	Snow depth	Not available.		One may assume that snow depth observations have a temporal and spatial	Snow depth appears to have a correlation with the type of ice (thicker/deformed ice often has thicker snow): The topography of the ice also has an impact on how the snow depth cover is, since the wind	$4.0 - 6.2\ cm$ (Interannual variability) -10 to 10 cm (based on ice type classification)	Not available.	Depends on snow depth estimates used. The values are based on

				correlation, since it depends on weather and wind patterns.	redistribution will depend on the topography.			the study of Ricker et al (2014) [RD93] that used W99 (Warren et al., 1999) [RD114] observations.
$u(\rho_i)$	Density of ice	Inverse problem using hydrostatic equilibrium for first-year ice: $\rho_i = \rho_w - \frac{\rho_w F_i + \rho_s H_s}{H_i}$, where ρ_i is density of ice, ρ_w is density of water, ρ_s is the density of snow, F_i is the sea ice freeboard, H_i is the sea ice thickness, and H_s is the snow		Observations acquired before the 2000s, so this needs to be taken into account. Observations have been acquired throughout the Siberian Arctic ocean (689	Density of ice can have a correlation with both snow density and water density, especially in the context of flooding events, where the flooded ice/snow will refreeze, and the density be altered.	$FYI: 35.7\ kg/m^3$ $MYI: 23.0\ kg/m^3$	Compared the bulk density estimates with recorded values of other studies, but the uncertainty was not further examined.	Alexandrov et al. (2010) [RD6]

		depth. Average ice density is determined for all FYI sites using $\rho_s = 324\ kgm^{-3}$, and $\rho_w = 1025\ kgm^{-3}$. We assume that FYI uncertainty is determined using standard deviation. MYI bulk ice density was determined using $\rho_{myi} = \rho_l(1 - F_i/H_i) + \rho_u F_i/H_i$, where typical freeboard (0.3m) and thickness (2.9m) values where inserted and densities of an		landing sites), but if measurements are acquired within a short time or spatial scale, they will have some correlation.			

		upper layer (ρ_u) was set af 550 kgm^{-3} and lower layer at 920 kgm^{-3}. The uncertainty was then calculated as a weighted average of ice density uncertainties for its upper and lower layers.						
$u(\rho_s)$	Density of snow	For Alexandrov et al. (2010) [RD-7], standard deviation of Sever expedition observations (689 landing sites).		Due to precipitation and wind patterns, one may assume a spatial and temporal correlation.	Density of snow is mostly related to temperature, and thereafter compaction and wind. Alexandrov et al. (2010) concluded the snow density between MYI and FYI was the same (only snow depth was different).	$50 - 150 \, kg/m^3$ $50 \, kg/m^3$	Alexandrov et al. (2010) [RD6] compared their snow densities with the recorded values of other studies, but not the uncertainty.	Ricker et al. (2014) [RD93] Alexandrov et al. (2010) [RD6]

$u(\rho_w)$	Density of seawater	Not mentioned.		Very little variation across the Arctic Ocean, although one may assume due to mixing that there will be a time and spatial correlation at short distances.	--	0.5 kg/m^3, although it is assumed to be negligible.	Not noted, but mentioned how other studies in the Arctic varies from 1024-1027 kgm^{-3}.	Alexandrov et al. (2010) [RD6]